# Methods[1]

Expedition 323 Scientists[2]

## Chapter contents

Background and objectives . . . . . 1
Lithostratigraphy . . . . . 2
Biostratigraphy . . . . . 8
Paleomagnetism . . . . . 13
Geochemistry . . . . . 14
Physical properties . . . . . 16
Stratigraphic correlation . . . . . 19
Downhole measurements . . . . . 24
Microbiology . . . . . 27
References . . . . . 28
Figures . . . . . 34
Tables . . . . . 45
Appendix . . . . . 49
Appendix figures . . . . . 51
Appendix table . . . . . 53

[1] Expedition 323 Scientists, 2011. Methods. *In* Takahashi, K., Ravelo, A.C., Alvarez Zarikian, C.A., and the Expedition 323 Scientists, *Proc. IODP,* 323: Tokyo (Integrated Ocean Drilling Program Management International, Inc.). doi:10.2204/iodp.proc.323.102.2011
[2] **Expedition 323 Scientists' addresses.**

## Background and objectives

This chapter documents the procedures and methods employed in the shipboard work described in the Expedition Reports section of the Expedition 323 *Proceedings of the Integrated Ocean Drilling Program* volume. Methods for shore-based analysis of Expedition 323 samples and data will be described in individual scientific contributions to be published elsewhere. All shipboard scientists contributed to the completion of this volume.

### Numbering of sites, holes, cores, and samples

Drilling sites are numbered consecutively beginning with the first site drilled by the *Glomar Challenger* in 1968. Integrated Ocean Drilling Program (IODP) Expedition 301 began using the prefix "U" to designate sites occupied by a U.S. Implementing Organization (USIO) vessel. For all IODP drill sites, a letter suffix distinguishes each hole drilled at the same site. The first hole drilled is assigned the site number modified by the suffix "A," the second hole takes the site number and the suffix "B," and so forth.

The cored interval is measured in meters below seafloor according to the core depth below seafloor, appended (CSF-A), depth scale (see "IODP depth scales terminology" at **www.iodp.org/program-policies/**). This depth scale is equivalent to the Ocean Drilling Program (ODP) depth scale meters below seafloor (mbsf) (see **"Core depth below seafloor (CSF-A)"** in "Stratigraphic correlation"). In general, depth below seafloor is determined by subtracting the water depth estimated from the initial drill pipe measurement to the seafloor from the total drill pipe measurement. The depth interval assigned to an individual core begins with the depth below seafloor at which coring began and extends to the depth to which coring advanced. Each coring interval is generally ≤9.5 m, which is the length of a core barrel; however, coring intervals may be shorter.

Cores taken from a hole are numbered sequentially from the top of the hole downward. Core numbers and their associated cored intervals are unique in a given hole. Generally, maximum recovery for a single core is 9.5 m of sediment in a plastic liner (6.6 cm internal diameter) plus ~0.2 m (without a plastic liner) of sediment in the core catcher, a device at the bottom of the core barrel that prevents the core from sliding out while the barrel is retrieved from the hole. In certain situations, recovery may exceed


doi:10.2204/iodp.proc.323.102.2011

the 9.5 m maximum. In soft sediments, this is normally caused by core expansion resulting from depressurization.

Recovered cores are divided into 1.5 m sections that are numbered serially from the top. When full recovery is obtained, these sections are numbered from 1 to 7, with the last section usually being shorter than 1.5 m. Rarely, an unusually long core may require more than seven sections. When a recovered core is shorter than the cored interval, the top of the core is equated with the top of the cored interval by convention to achieve consistency in handling analytic data derived from the cores. All pieces recovered are placed immediately adjacent to each other in the core tray. Samples and descriptions of cores are designated by distance, measured in centimeters from the top of the section to the top and bottom of each sample or interval. By convention, when a core is described, material recovered from the core catcher is placed below the last section and labeled with the suffix "CC." In sedimentary cores, core catcher sections are treated as separate sections. The core catcher is placed at the top of the cored interval when material is recovered only in the core catcher. However, information supplied by the drillers or logging may allow more precise interpretation of the correct position of core catcher material within an incomplete recovered core interval.

Complete sample identification numbers include the following information: expedition, site, hole, core number, core type, and section number, with the interval in centimeters measured from the top of the section. For example, the sample identification "323-U1339A-26H-8, 4–7 cm" indicates a 3 cm sample removed from the interval between 4 and 7 cm below the top of Section 8 of Core 26 ("H" designates that this core was taken with the advanced piston corer [APC]) in Hole A at Site U1339 during Expedition 323.

### Core handling

Cores recovered during Expedition 323 were extracted from the core barrel in plastic liners. These liners were carried from the rig floor to the core processing area on the catwalk outside the core laboratory, where they were split into ~1.5 m sections. Liner caps (blue = top; colorless = bottom) were glued with acetone onto liner sections on the catwalk by the curator. The length was entered into the database as "created length" using the Sample Master application. This number was used to calculate recovery.

Each section was allowed to equilibrate to ambient room temperature (4 h for sediment) and scanned with the shipboard Whole-Round Multisensor Logger (WRMSL) (see **"Physical properties"**). Whole-round core sections were then measured with the Natural Gamma Radiation Logger (NGRL) (see **"Physical properties"**) and transferred to the core splitting room, where the plastic liners were split lengthwise into archive and working halves.

The archive halves were described for lithology and structural features, and observations were recorded using the descriptive data capture application, DESClogik. Specialized templates and spreadsheets were developed for this application by the individual descriptive laboratory groups (for details, see individual disciplinary sections in this chapter). Digital images of the cut faces of the archive halves were captured with the Section Half Imaging Logger (SHIL). Measurements of point magnetic susceptibility and color reflectance were performed with the Section Half Multisensor Logger (SHMSL) on the archive halves. This instrument also includes a laser calibration system. Data from the laser (e.g., the location of core gaps and rubble intervals) were used to aid data filtering of multisensor measurements (see **"Physical properties"**).

Finally, digital color close-up photographs were taken of particular features, as requested by individual scientists. The working halves were sampled for both shipboard core characterization and shore-based studies.

Samples were taken from the working halves for shipboard physical properties, paleomagnetism, thin section, X-ray diffraction (XRD), and geochemical analyses, as described below. Each extracted sample was logged in the Sample Master database program by location, sample type, and intended shipboard study (e.g., thin section, XRD, etc.). Records of all removed samples are kept by the IODP Curatorial Specialist. At the end of Expedition 323, all cores were transferred from the ship for permanent storage at the Kochi Core Center at Kochi University, Japan. A postexpedition sampling party was organized and carried out at the Kochi Core Center to take the bulk of personal samples requested by members of the science party.

## Lithostratigraphy

In the description of marine sediments collected by IODP and its predecessors, lithologic, textural, and genetic sediment classifications have often been used interchangeably. Moreover, criteria that range from purely descriptive to purely interpretational have been used to identify sedimentary structures. This has been a significant obstacle to the objective representation of sediment characteristics and has complicated the exchange of information between

marine sedimentologists and other marine scientists and, more importantly, the interpretation of sediment data. Consequently, we sought to document the sediments collected during Expedition 323 with objective, reproducible, and unbiased descriptions. Interpretation was only employed for primary (e.g., cross-lamination and turbidites) and nonprimary (e.g., drilling disturbances) sedimentary and diagenetic structures that unequivocally meet the criteria explained in this section.

## Preparation for core description

After the core sections were split, the archive halves were put on the description table. Before further processing occurred, the split surfaces of the archive halves were scraped lightly with a glass slide or spatula to create an even surface.

## Smear slides

One or more smear slide samples of the main lithology were collected from the archive half of each core section. Additional samples were collected from areas of interest (e.g., laminations, ash layers, mottles, etc.). A small amount of sediment was taken with a wooden toothpick and put on a 2.5 cm × 7.5 cm glass slide. The sediment sample was homogenized with a drop of deionized water and evenly spread across the slide to create a very thin (about <50 µm) uniform layer of sediment grains for quantification. The dispersed sample was dried on a hot plate. A drop of Norland optical adhesive was added as a mounting medium to a coverslip, which was carefully placed on the dried sample to prevent air bubbles from being trapped in the adhesive. The smear slide was then fixed in an ultraviolet light box.

Smear slides were examined with a transmitted-light petrographic microscope equipped with a standard eyepiece micrometer. The texture of siliciclastic grains (relative abundance of sand-, silt-, and clay-sized grains) and the proportions and presence of biogenic and mineral components were recorded on a smear slide sample sheet (Fig. F1). Biogenic and mineral components were identified, and their percentage abundances were visually estimated using Rothwell (1989). The mineralogy of clay-sized grains could not be determined from smear slides. Note that smear slide analyses tend to underestimate the amount of sand-sized and larger grains because these grains are difficult to incorporate onto the slide. Postcruise quantitative analysis of grain sizes from Site U1339 demonstrated that clay-sized grains were underdescribed in the smear slides (I. Aiello, pers. comm., 2010), and this is probably the case for slides from other sites as well.

## Thin sections

To better characterize the composition and texture of clasts, very sandy lithologies, relatively large (>2 cm) authigenic nodules, and other similar lithified and partially lithified structures, petrographic thin sections (~30 µm thick) were prepared and then analyzed with a petrographic microscope. The observations were recorded on a thin section sample sheet (Fig. F2).

## Digital color imaging

The flat faces of the archive halves were scanned with the SHIL as soon as possible after splitting and scraping to avoid color changes caused by sediment oxidation and drying. The SHIL uses three pairs of advanced illumination high-current-focused light-emitting diode (LED) line lights to illuminate large cracks and blocks in the core surface and sidewalls. Each LED pair has a color temperature of 6500 K and emits 90,000 lx at 3 inches. A line-scan camera imaged 10 lines per millimeter to create a high-resolution TIFF file. The camera height was adjusted so that each pixel imaged a 0.1 $mm^2$ section of the core. However, actual core width per pixel varied some because of differences in section-half surface height. High- and low-resolution JPEG files were subsequently created from the high-resolution TIFF file. All image files include a grayscale and ruler. Section-half depths were recorded so that these images could be used for core description and analysis.

## Spectrophotometry (color reflectance)

Color reflectance was measured on the surfaces of the split cores every 5 cm using the SHMSL. The surfaces of the archive halves were covered with plastic wrap to prevent contamination of the spectrophotometer lens. The Ocean Optics USB4000 spectrophotometer recorded counts every ~0.2 nm in the range of 177 to 925 nm, which includes the visible and near-infrared spectra. Spectral data were related to color in a cylindrical coordinate system using the tristimulus values L*, a*, and b* (Commission Internationale d'Eclairage, 1986), where the axis of the cylinder, L*, is total light reflected, or luminosity, a* is redness, and b* is yellowness. Before each core was measured, the spectrophotometer was calibrated with a Labsphere-certified white reflectance standard and a black light trap with the light source shuttered. For Sites U1342–U1345, the standards were covered with the same plastic wrap used to cover the core sections. For Sites U1339–U1341, the instrument was calibrated every ~12 h with the same piece of plastic wrap covering the standards and different plastic wrap covering the core. The reflectance data contain

artifacts from the leakage of room lights to the sensor as a function of the flatness and the induration of the sediment surface. Secular drift in the data occurred with infrequent calibration, possibly precluding the use of these data for quantitative reconstruction of sediment composition.

## X-ray diffraction analysis

Intervals of interest (e.g., marked lithologic or color contrasts, diagenetic layers or nodules, and microscopically unidentified minerals) identified during visual core description and in smear slides were sampled for mineralogical analyses from the working halves of the cores. Minimum sample volumes of ~5 $cm^3$ were frozen, freeze-dried, and ground by hand or in an agate ball mill. Prepared samples were mounted onto a sample holder and analyzed by XRD. XRD samples were analyzed using a Bruker D-4 Endeavor diffractometer mounted with a Vantec-1 detector using nickel-filtered CuKα radiation. The standard locked coupled scan was as follows:

Voltage = 40 kV.
Current = 40 mA.
Goniometer scan = 5° to 90°2θ.
Step size = 0.015°2θ.
Scan speed = 0.1 s/step.
Divergence slit = 0.3 mm.

Diffractograms of single samples were evaluated with the Bruker DiffracPlus software package. Reliable results obtained by this analysis are limited to minerals composing at least 1% of the total sediment. Notably, quantification of mineral content was not possible because the samples were not spiked with a defined amount of mineral standard for calibration. Therefore, shipboard results yield only qualitative results on the relative occurrences and abundances of the most abundant mineralogical components. XRD spectra and interpretations are available as supplementary materials (see XRD in **"Supplementary material"**).

## Sediment description worksheets, standard graphical reports, and summary figures

Sediment lithology, color (using Munsell soil color charts [Munsell Color Company, 1994]), structures, accessories, disturbances, and other observations were recorded on visual core description worksheets (Figs. **F3, F4**). The handwritten core description worksheets are available as supplementary material (see LITH in **"Supplementary material"**). In addition, core descriptions were entered into the Laboratory Information Management System (LIMS) database using DESClogik. There are some differences between the core description worksheets and the data in LIMS, so in case of disagreement, the core description worksheets should be considered the primary record of core description. The LIMS database was used to make two types of core description summaries.

First, annotated standard graphical reports, or visual core descriptions (VCDs), were created for each core to summarize data collected during Expedition 323 (Fig. **F5**). The Strater software package was used to compile lithology, biostratigraphy, and physical properties data entered into DESClogik. Each VCD includes site, hole, and core number, followed by a narrative description of major and minor lithologies, the types of boundaries observed between lithologies, and color. On the far left of the VCD are depth below seafloor (mbsf), core length, and section breaks, which provide vertical reference points. The scanned core image is followed by a graphical representation of lithologies and contacts using the colors, patterns, and symbols illustrated in Figure **F6.** Single or multiple interbedded lithologies can be represented in one interval. In general, only lithologies composing >25% of the core are shown graphically; however, an exception is made for some distinct minor lithologies such as ash or authigenic carbonate layers. The right-hand columns show bioturbation intensity, coring disturbances, sedimentary structures, lithologic accessories, samples taken during Expedition 323 for shipboard analyses (e.g., XRD, interstitial water, etc.), and stratigraphic ages (datums). Further to the right are plots of physical properties data, including magnetic susceptibility ($10^{-5}$ SI units), gamma ray attenuation (GRA) bulk density ($g/cm^3$), and color reflectance parameter b* (blue to yellow color space). The far right column contains comments such as notes about laminations, authigenic carbonates, or unusual structures and accessories.

Second, lithologic summary figures were produced for each hole. These figures show 250 m per page (in contrast to the single core [~10 m] per page shown in the VCDs), except for Site U1342 summary figures, which show only 65 m per page (Fig. **F7**). These figures include depth below seafloor (mbsf), core recovery, a lithologic column (which uses the same colors as the VCDs but does not include symbols or contacts), and unit boundaries. Also plotted are the occurrences of soft-sediment deformation, coring disturbances, ash layers, lithologies with >25% sand, sandy layers and mottles, clasts, shells, authigenic carbonates (including yellowish foraminifers recorded by biostratigraphers; see **"Biostratigraphy"** and **"Lithostratigraphy"** in the "Site U1343" chapter), and the abundances of diatoms, foraminifers, calcareous nannofossils, and sponge spicules (Fig.

F7). To the right of these are plots of color reflectance parameter b*, natural gamma radiation (NGR), GRA bulk density, and magnetic susceptibility (plotted with lines showing the data averaged in 0.25 m nonoverlapping bins), followed by selected biostratigraphic and paleomagnetic datums. The Lisiecki and Raymo (2005) oxygen isotope stack is plotted in the panel on the far right, with datum ages and paleomagnetic ages provided for comparison.

## Sediment and hard rock classification

Different lithologic classifications have been proposed for ODP and IODP cruises during the last decade, and these classifications have been adapted according to cruise objectives and/or specific goals of shipboard participants. In some cases, these classifications are inconsistent with other mineralogical and geochemical determinations of the same data set. Because the goal of classifying sediments during Expedition 323 was mainly compositional, the use of genetic terms such as "pelagic" was avoided and the term "hemipelagic" was replaced with "mixed" to describe sediments with mixed biogenic and siliciclastic composition.

### Sediment lithology

The principal name applied to a sediment is determined by the component or group of components (e.g., total biogenic silica) making up >60% of the sediment or rock, with the exception of subequal mixtures of biogenic and siliciclastic and/or volcaniclastic material (Fig. F8D). Principal names are determined as follows.

#### *Siliciclastic sediments*

If total siliciclastic plus volcaniclastic content is >60% (Fig. F8D) and siliciclastic content is >80% of the siliciclastic plus volcaniclastic fraction (Fig. F8C), the principal name is determined by the texture of the siliciclastic grains, that is, the relative proportions of sand-, silt-, and clay-sized grains when plotted on a modified Shepard (1954) ternary classification diagram (Fig. F8A). The siliciclastic principal names are clay, silt, sand, silty clay, sandy clay, clayey silt, sandy silt, clayey sand, and silty sand.

#### *Volcaniclastic sediments*

Volcaniclastic sediments are defined as sediments derived from a primary volcanic process, including epiclastic sediment, the particles of which are derived from the weathering and erosion of preexisting volcanic rock, and primary volcanic material. Primary volcanic processes include sediment derived from the quench-granulation of lava flows as well as pyroclastic processes such as air fall and pyroclastic flow. If total siliciclastic plus volcaniclastic content is >60% (Fig. F8D) and volcaniclastic content is >80% of the siliciclastic plus volcaniclastic fraction (Fig. F8C), volcanic particles are designated as fine ash (<0.063 mm), coarse ash (0.063–2 mm), or lapilli (2–64 mm) according to Fisher and Schmincke's (1984) and Gillespie and Styles's (www.bgs.ac.uk/downloads/start.cfm?id=7) classifications. Principal names are then given according to the category of the majority of the volcaniclastic grains. If a primary volcanic nature can be ascertained, the sediment is described using the conventions employed for siliciclastic sediment.

#### *Biogenic sediments*

If total biogenic content is >60% (i.e., siliciclastic plus volcaniclastic material is <40%), the principal name applied is ooze (Fig. F8B). The major modifier consists of the name(s) of the major fossil group(s) composing at least 40% of the biogenic fraction, with the least common fossil listed first. Biogenic components are not described in textural terms. Thus, sediment containing 65% sand-sized foraminifers and 35% siliciclastic clay is called foraminifer ooze, not foraminifer sand.

#### *Mixed sediments*

Mixed sediments include sediments with <40% biogenic grains and a subequal mixture of siliciclastic and volcaniclastic grains or sediments with 40%–60% biogenic grains. The principal names of mixed sediments have two parts, as described below.

If total siliciclastic plus volcaniclastic content is >60% (Fig. F8D) and siliciclastic content is 50%–80% of the siliciclastic plus volcaniclastic fraction (Fig. F8C), the principal name is determined by the texture of the siliciclastic grains, with the major modifier determined by the size of the volcaniclastic grains (as above). For example, the principal name of a sample containing 20% diatoms, 30% fine ash, and 50% lithogenic grains that are >75% silt-sized is fine-ashy silt.

If total siliciclastic plus volcaniclastic content is >60% (Fig. F8D) and volcaniclastic content is 50%–80% of the siliciclastic plus volcaniclastic fraction (Fig. F8C), the principal name is determined by the size of the volcaniclastic fraction (as above), with the major modifier determined by the texture of the siliciclastic grains (Fig. F8A). For example, the principal name of a sample containing 20% diatoms, 30% lithogenic grains that are >75% silt-sized, and 50% fine ash is a silty fine ash.

If biogenic content is 40%–60%, (Fig. F8D), the principal name consists of two parts: (1) the principal name appropriate for the siliciclastic components (if there is a greater proportion of siliciclastic than volcaniclastic grains) or the principal name appropriate for the volcaniclastic components (if there is a greater proportion of volcaniclastic than siliciclastic grains) and (2) a major modifier appropriate for the major fossil group(s) (as above). Examples of principal names for mixed sediments are diatom fine ash and foraminifer-diatom silty clay.

## Prefixes

If a microfossil group composes 5%–40% of the sediment and this group is not included as part of the principal name, minor modifiers are used. When a microfossil group (e.g., diatom, nannofossil, or foraminifer) composes 10%–40% of the sediment, a minor modifier (see Fig. F8B) consisting of the component name hyphenated with the suffix "rich" (e.g., diatom-rich clay) is used. When a microfossil group composes 5%–10% of the sediment, a minor modifier (see Fig. F8B, F8D) consisting of the component name hyphenated with the word "bearing" (e.g., diatom-bearing clay) is used. When two minor components are present, minor modifiers are listed before the principal name in order of increasing abundance. For example, sediment with 15% foraminifers, 40% nannofossils, and 45% clay is foraminifer-rich nannofossil clay; sediment with 5% diatoms, 15% radiolarians, and 80% clay is diatom-bearing radiolarian-rich clay.

### *Indurated lithologies*

Hard indurated rocks have names that reflect the major constituent of the sediment in which they originated:

- Dolostone: a white indurated rock composed of authigenic dolomite;
- Claystone: an indurated rock composed of clay;
- Siltstone: an indurated rock composed of silt;
- Sandstone: an indurated rock composed of sand;
- Breccia: an indurated rock composed of larger than sand-sized angular clasts;
- Fine ash tuff: an indurated rock composed of fine ash–sized primary volcanic particles;
- Coarse ash tuff: an indurated rock composed of coarse ash–sized primary volcanic particles;
- Lapilli tuff: an indurated rock composed of lapilli-sized primary volcanic particles;
- Tuff-breccia: an indurated rock composed of block-sized and block-shaped particles in a matrix of ash-sized primary volcanic particles;
- Agglomerate: an indurated rock composed of bomb-sized and bomb-shaped primary volcanic particles;
- Volcaniclastic sandstone: an indurated rock composed of sand-sized volcanic particles (this name may be modified by indicating the size of the sand particles—e.g., a volcaniclastic medium-grained sandstone); and
- Volcaniclastic breccia: an indurated rock composed of gravel-sized volcanic particles.

Induration is separated into four classes:

1. Soupy: water-saturated sediment with very little strength;
2. Soft: sediment with little strength that is readily deformed under the pressure of a finger or broad-blade spatula;
3. Stiff: partly lithified sediment that is readily scratched with a fingernail or the edge of a spatula; and
4. Hard: well-lithified and cemented sediment that is resistant or impossible to scratch with a fingernail or the edge of a spatula or core that must be cut with a band saw or diamond saw.

### *Gravel-sized grains*

Several sites drilled during Expedition 323 are located along the glacially influenced continental margin of Alaska. Isolated gravel-sized clasts were recorded and, when possible, are described as follows. Note that clast occurrence is almost certainly undersampled because our observations were limited to the cut surface of the section halves. Clasts are classified as sedimentary, igneous, or metamorphic and are described according to their roundness and sphericity (Powers, 1953). Sedimentary rocks are described by color (Munsell chart) and grain size of the groundmass and are given a name consistent with the indurated lithologies described above. Metamorphic rocks are classified as either nonfoliated or foliated. Nonfoliated rocks are called "hornfels." Foliated rocks are classified as slate, phyllite, schist, or gneiss depending on the nature of the foliation. Igneous rocks are described by color (Munsell chart) and, when possible, phenocryst abundance (in percent or number/inch$^2$), phenocryst composition, phenocryst grain size, vesicle abundance, and vesicle shape (spherical, ovoid, and irregular) and are named following the scheme of Streckeisen (1974).

### *Hard rocks at Site U1342*

Hard rocks recovered from Site U1342 are described in the same way as gravel-sized grains (above). Volcaniclastic rocks drilled at Site U1342 are additionally described by the grain size of the groundmass, the

shape of the clasts or grains, the degree of rounding of the clasts or grains, and the degree of sorting (including bimodal sorting and sorting ranging from very well sorted to very poorly sorted). Igneous rocks are further described by phenocryst abundance (in percent or number/inch$^2$), phenocryst composition, phenocryst grain size, vesicle abundance, composition of vesicle infilling, and vesicle shape (spherical, ovoid, and irregular), following the scheme of Streckeisen (1974).

### Accessories

Accessories include macroscopic biogenic remains such as shells, sponge spicule aggregates, worm tubes, wood fragments, and mottling (e.g., ash, sand, and pyrite), as well as clasts, concretions, nodules, alteration halos, specks, sandy layers, and ash layers (<2 cm thick). A concretion is a small, irregularly rounded knot, mass, or lump of a mineral or mineral aggregate, normally having a warty or knobby surface and no internal structure and usually exhibiting a contrasting composition from the sediment or rock matrix in which it is embedded. A nodule is a regular, globular structure. When possible, clasts, concretions, and nodules are described by composition. An alteration halo is an area where sediment is a different color or composition in a ring surrounding a grain or accessory phase. A speck is a small spot or smear where sediment is a different color or composition than the surrounding sediment (it is not ring shaped, like an alteration halo). Pyrite is an example of a speck composition.

### Nonbiogenic structures

Lithologic, textural, or color discontinuities are identified as boundaries. Boundaries between different lithologies are classified as sharp, gradational, or wavy. If alternation of different lithologies occurs at a <30 cm scale, the lithologies are described together as a bedded or laminated unit. Bedding and lamination, respectively, are defined as follows:

Thick bedded = >30 cm.
Medium bedded = >10 cm and ≤30 cm.
Thin bedded = >3 cm and ≤10 cm.
Very thin bedded = >1 cm and ≤3 cm.
Thickly laminated = >0.3 cm and ≤1 cm.
Thinly laminated = ≤0.3 cm.

Bedding/lamination features include

- Fining-upward bedding: a layer with grains displaying a gradual uphole decrease in size;
- Coarsening-upward bedding: a layer with grains displaying a gradual uphole increase in size;
- Tilted bedding: layers of sediment that are inclined relative to the core barrel but have no clear relationship to adjacent layers;
- Cross bedding/cross lamination: layers of sediment that are inclined and truncated relative to the base and top of the set in which the inclined layers are grouped;
- Parallel laminae: alternation of parallel laminae of differing composition and/or color; and
- Wavy/undulated laminae: parallel laminae with gentle sinuosity or slightly diffuse contacts.

Other nonbiogenic structures include

- Bottom cast: preservation of seafloor irregularity caused by seafloor scouring due to a high flow regime or density contrasts between adjacent lithologies;
- Soft-sediment deformation: wavy to disorganized, twisted, or folded layers interbedded with nondeformed strata; and
- Vein: a mineral-filled fracture.

Structures associated with coring disturbances include

- Biscuits: the core is partitioned into biscuits and highly sheared zones by rotation of the core in the core barrel during extended core barrel (XCB) coring;
- Pieces: the core is broken into pieces, usually from extrusion from the core barrel due to gas expansion or extraction from the core catcher;
- Flow-in: the core is intruded by other materials such as sand due to sucking during retrieval of the APC;
- Fall-in: material falls from the hole walls onto subsequent cores and is found at the top of Section 1 and smeared along the core liner;
- Soupy: the top of the core is very loose and watery from exposure to seawater, exposure to seawater and sediment from the walls of the hole being scraped into the core barrel from shooting short cores with the APC, or from washing during XCB coring;
- Puncture: a disturbance that results from piercing a small hole through the core liner for degassing that causes a loss of sediment around the holes;
- Gas expansion: part of the core is partitioned into pieces and voids due to the expansion of interstitial gas;
- Crack: an open fracture caused by gas expansion, desiccation, or disturbance of the sediment after drilling; and

- Void: a large fracture (>2 cm) caused by gas expansion or disturbance of the sediment after drilling.

The intensity of coring disturbance is described as follows:

- Slightly disturbed: the original structure of the core is still visible;
- Moderately disturbed: the original structure of the core is fairly visible; or
- Highly/severely disturbed: the original structure of the core is lost.

### Biogenic structures

Biogenic structures are structures produced by macrofauna that lived on or in the sediment during deposition (trace fossils). The intensity of bioturbation is first described according to the following classes:

- Absent or nonvisible (0%),
- Slight (0%–30%),
- Moderate (>30%–60%), and
- Strong (>60%–100%).

These percentages were estimated relative to the surface area of the split core and were conducted on the portions of sediment affected by obvious burrowing, that is, where the color/texture of the dominant lithology is disrupted by features (tubular, mottled, etc.) having colors or textures imported from adjacent layers of different composition. Note that it may be impossible to distinguish between sediment of homogeneous composition without any bioturbation and sediment that has been effectively homogenized by bioturbation. The shape and geometry of bioturbation structures (e.g., vertical, horizontal, and mottled) are described and, when possible, attributed to one of four major ichnofacies types (*Planolites*, *Zoophycos*, *Chondrites*, and *Skolithos*).

## Biostratigraphy

Preliminary ages were assigned based on the biostratigraphic assessment of calcareous nannofossil, planktonic foraminifer, diatom, silicoflagellate, ebridian, dinoflagellate cyst, and radiolarian events. Paleoenvironmental interpretations are based on all of these groups, including benthic foraminifers and ostracodes. Biostratigraphy was correlated to the geomagnetic polarity timescale (GPTS) used for Expedition 323, which is based upon a composite of several timescales (Lourens et al., 2004). Microfossil datums were established by analyzing core catcher samples. When a more refined age determination was necessary, samples were taken from the core sections at appropriate intervals. The shipboard methods used to assess each microfossil group are detailed below.

### Calcareous nannofossils

The standard Tertiary and Quaternary calcareous nannoplankton zonation proposed by Martini (1971) was selected as the main temporal framework for Expedition 323. This scheme contains well-established additional events such as the first occurrence (FO) and last occurrence (LO) datums of *Reticulofenestra asanoi* (Sato and Takayama, 1992). However, the application of this zonation to materials from the Bering Sea is problematic because the known biogeographical distribution of marker taxa (such as discoasterids) does not cover high latitudes in the Pacific Ocean (Sato et al., 2002). Therefore, the standard calcareous nannofossil zonation and the bioevents list were adapted to the specific composition of the assemblages present in the studied samples, and additional high-latitude calcareous nannofossil events, such as abundance reversals noted by Sato and Kameo (1996) and Sato et al. (2002), were added to Table **T1.** Age estimates for the proposed datums were adopted from Lourens et al. (2004), with the exception of the reversal in dominance between *Dictyococcites* spp. (small) and *Coccolithus pelagicus*, which was dated to 2.75 Ma by Sato et al. (2002).

### Methods

Samples were prepared following a standard smear slide preparation method. A small amount of sediment was placed onto a glass slide with a few drops of deionized water. The sediment was then smeared with a wooden toothpick and allowed to dry on a hot plate at low temperature. A drop of Norland optical adhesive was added as a mounting medium to the sample, which was covered with a coverslip and set to harden under an ultraviolet lamp for 15 min. The slide was then examined with a Zeiss light microscope at 1000× magnification using cross-polarized and transmitted light.

As a general rule, the taxonomic concepts summarized in Young (1998) and Hine and Weaver (1998) were followed. However, terms were occasionally adjusted to adapt classification to the special characteristics of the assemblages present in the Bering Sea. Onboard taxonomic classification and data files were also updated for specific taxa such as *Coccolithus pelagicus* (which was divided into *C. pelagicus* and *Coccolithus braarudii*, in accordance with Sáez et al., 2003).

Calcareous nannofossil preservation was estimated using the criteria established by Raffi and Flores (1995), who proposed four categories depending on the "average" state of preservation of the specimens examined in the smear slides:

G = good; little or no evidence of dissolution and/or overgrowth, and specimens are identifiable to the species level.
M-G = moderate to good; minor to moderate dissolution and/or overgrowth, but most specimens are identifiable to the species level.
M = moderate; moderate dissolution and/or overgrowth, and identification to the species level is difficult.
P = poor; extreme dissolution and/or overgrowth.

The total abundance of calcareous nannofossils in each sample was assessed using semiquantitative abundance codes:

A = abundant; >1 specimen per field of view (FOV).
C = common; ≤1 specimen per FOV.
F = few; <1 specimen per 2–10 FOV.
R = rare; <1 specimen per 11–100 FOV.
B = barren; no nannofossils present.

The abundances of individual nannofossil taxa were assessed as follows:

D = dominant; more than half of the specimens in FOV belong to this taxon.
A = abundant; >1 specimen per FOV.
C = common; ≤1 specimen per FOV.
F = few; <1 specimen per 2–10 FOV.
R = rare; <1 specimen per 11–100 FOV.

## Foraminifers

High-latitude Bering Sea planktonic foraminiferal assemblages have low diversity, and thus biostratigraphic datums are infrequent. However, preliminary ages were assigned using Neogene planktonic biostratigraphic zonations from the North Atlantic (Weaver and Clement, 1987; Spezzaferri, 1998) for Pliocene and Pleistocene samples from Expedition 323 (Table T2). Planktonic foraminiferal taxonomy largely follows that of Kennett and Srinivasan (1983). The Neogene timescale correlated to magnetostratigraphy, as defined by Lourens et al. (2004), was applied in this study. Benthic foraminifers have limited biostratigraphic use, but they provide indispensable information about water masses, including productivity and oxygen levels (e.g., Jorissen et al., 1995; Van der Zwaan et al., 1999). Benthic foraminifers are defined as faunal assemblage zones following Salvador (1994). The assemblage zones are named after the most frequent benthic foraminifers. Benthic taxonomy largely follows the definitions by Loeblich and Tappan (1988).

### Methods

More than 40 $cm^3$ of sediment from each core catcher sample was analyzed for planktonic and benthic foraminifers. In addition, mudline samples from most holes were also analyzed. Mudline samples were collected by emptying the sediment/water material from the top core liner of each hole into a bucket. Tests using Rose Bengal staining confirmed the presence of some living foraminifers in the mudline samples. All samples were disaggregated by being soaked and washed with warm deionized water through a 63 µm mesh sieve. Weakly lithified sediments were disaggregated with detergent (borax). Strongly lithified sediments were disaggregated before wet sieving and dried and soaked for 6–12 h in kerosene. The kerosene was decanted, and boiling water was added to aid disaggregation. After wet sieving, sample fractions were dried in an oven (maximum temperature = 50°C). To minimize contamination of foraminifers between samples, the sieve was placed into a sonicator for several minutes and thoroughly inspected. Faunal analysis was carried out using a Zeiss Stemi SV11 or Zeiss DR binocular microscope. The >63 µm (benthic) and >125 µm (planktonic) size fractions were analyzed for foraminifer preservation, abundance, and faunal composition. Preservation of foraminiferal tests includes any effects of diagenesis, abrasion, encrustation, and/or dissolution.

Benthic and planktonic foraminifer preservation is categorized as follows:

VG = very good; no breakage or dissolution.
G = good; only very minor dissolution and no recrystallization; <10% of specimens are broken.
M = moderate; frequent etching and partial breakage; 30%–90% of specimens are unbroken.
P = poor; much dissolution and recrystallization; broken specimens dominate.

Planktonic foraminifer abundance in the >125 µm fraction in relation to the total residue is defined as follows:

D = dominant; >30%.
A = abundant; >10%–30%.
F = few; >5%–10%.
R = rare; 1%–5%.
P = present; <1%.
B = barren; no planktonic foraminifers present.

Benthic foraminifer abundance in the >63 µm fraction is recorded as follows:

D = dominant; >30 specimens.
A = abundant; >10–30 specimens.
F = few; >5–10 specimens.

R = rare; >1–5 specimens.
P = present; 1 specimen.
B = barren; no benthic foraminifers present.

Benthic foraminifer abundance, as plotted in site chapter figures, is calculated as the sum of total relative species abundance, with the following values assigned to each category:

B = 0.
P = 1.
R = 3.
F = 8.
A = 20.
D = 40.

## Ostracodes

Ostracodes (calcareous bivalve microcrustaceans) are the only metazoan organisms commonly preserved as microfossils in deep-sea sediments. Like benthic foraminifers, ostracodes have limited biostratigraphic use, but they can provide important environmental information and are valuable proxies in paleoceanographic studies (Dingle and Lord, 1990; Corrège 1993; Cronin et al., 2002; Ayress et al., 1997; Whatley et al., 1998; Alvarez Zarikian et al., 2009). Assemblage zones are named after the most frequent ostracode taxa. Taxonomic identification follows the taxonomy provided by Joy and Clark (1977), Whatley and Coles (1987), Didié and Bauch (2001), Stepanova (2006), Stepanova et al. (2004), Alvarez Zarikian (2009), and Yasuhara et al. (2009).

Ostracodes were picked, identified, and counted from core catcher samples following the sample methodology used for benthic foraminifers (see above). Carapace or valve preservation is classified according to three categories ranging from transparent (best) to white and chalky (poor).

## Diatoms

### Zonation

Diatom zonation used for the Neogene closely follows the zonation by Yanagisawa and Akiba (1998). Datums were modified in line with the updated geologic timescale (Lourens et al., 2004). A major alteration was made in the technique used to identify *Neodenticula* species *N. seminae* and *N. koizumii*. As discussed by Yanagisawa and Akiba (1990, 1998), the extant species *N. seminae* is closely related to the extinct species *N. koizumii* and the intermediary extinct species *Neodenticula* sp. A in the light microscope. The distinguishing feature is the copula formation. The copula of *N. seminae* is closed, smooth, and rounded, whereas the copula of *N. koizumii* and *Neodenticula* sp. A (which is classified as an intermediary form of *N. koizumii* [Yanagisawa and Akiba, 1998]) is open and pointed when well preserved. Thus, when ambiguity was found in distinguishing the species, counts of open versus closed copula were made to determine the first common occurrence (FCO) of *N. seminae* and the last common occurrence (LCO) of *N. koizumii*.

### Methods

Strewn slides were prepared following the methods of Barron and Gladenkov (1995). A small amount of material was placed in a snap-cap vial. Deionized water was added, and the vial was shaken. The upper suspension was then removed with a pipette. Strewn slides were examined in their entirety at 630× magnification for stratigraphic markers and paleoenvironmentally sensitive taxa. Identifications were also checked routinely at 1000× magnification. Whenever possible, all diatom taxa were tabulated until 100 specimens were counted (with the exception of *Chaetoceros* resting and vegetative spores). In addition, because several age indicators (e.g., *Proboscia* spp.) are relatively large and are usually rare in total diatom abundances, additional counting was performed with slides prepared for silicoflagellate studies, whereby abundant small diatoms were removed by the 20 µm grain-size fraction (see **"Silicoflagellates and ebridians"** below).

Total diatom abundance was assessed in relation to the remaining residue according to Scherer and Koç (1996):

M = mass; >60% diatoms.
A = abundant; ~20%–60% diatoms.
C = common; ~5%–20% diatoms.
F = few; 2%–5% diatoms.
R = rare; <2% diatoms.
B = barren; no diatoms present.

The relative abundance of each diatom taxon, as reported in range charts, was estimated using a qualitative scale. Values indicate counts of 100 diatom valves; a blank indicates that specimens are absent. The relative abundances of species are defined as follows:

D = dominant; >60% of assemblage.
A = abundant; >20%–60% of assemblage.
C = common; >5%–20% of assemblage.
F = few; 2%–5% of assemblage.
R = rare; <2% of assemblage.
T = trace; sporadic occurrence.

Diatom preservation categories, as reported in range charts, are described qualitatively according to Barron and Gladenkov (1995):

G = good; finely silicified forms are present with no alteration of frustules.

M = moderate; finely silicified forms are present with some alteration.
P = poor; finely silicified forms are absent or rare and fragmented, and assemblage is dominated by robust forms.

## Silicoflagellates and ebridians

During Expedition 323, the biostratigraphic framework used for silicoflagellates and ebridians was Ling (1977), which is the compiled version of Bukry (1973) and Ling (1973) from the Bering Sea and other previous studies in the North Pacific. The methods of Ling (1973, 1977), as well as Kobayashi (1988; Hole 438A) and Ling (1992; Sites 798 and 799), were applied for the age estimation of datum levels. All estimated ages were adjusted to the astronomically tuned Neogene timescale (ATNTS2004: Lourens et al., 2004).

Silicoflagellate and ebridian microslides for Sites U1340–U1345 were prepared as follows. A small amount (~0.5 $cm^3$) of core catcher sample was sieved with a 20 µm mesh and hot water. The coarser fraction (>20 µm) was mounted on a glass slide with Norland optical adhesive (number 61). Microscopic observation for silicoflagellates and ebridians was conducted using the >20 µm fraction slides. In addition, microslides prepared for diatom observation (see **"Diatoms"**) were also examined to identify the small-sized ebridian *Ammodochium rectangulare*. For Site U1339, only microslides prepared for diatom microscopic observations were used for species identification and counting of both silicoflagellates and ebridians because sediment samples from Site U1339 contain a sufficient number of skeletons for counting.

Overall abundances of silicoflagellates and ebridians were determined by counting specimens over eight traverses (perpendicular to the length of the slide) at 400× using the following conventions:

A = abundant; >50 specimens.
C = common; 16–50 specimens.
F = few; 6–15 specimens.
R = rare; 2–5 specimens.
T = trace; 1 specimen.
B = barren; no specimens present.

Preservation of silicoflagellates and ebridians is recorded as follows:

G = good; majority of specimens complete, with minor dissolution and/or breakage.
M = moderate; minor but common dissolution, with some specimen breakage.
P = poor; strong dissolution and/or breakage; many specimens unidentifiable.

## Radiolarians

Although no detailed radiolarian biostratigraphic study in the Bering Sea was conducted before Expedition 323, a biostratigraphic zonation was developed for the subarctic Pacific. Hays (1970) first proposed upper Pliocene to Quaternary radiolarian zones from piston core samples in the subarctic Pacific. Shilov (1995) proposed new Pliocene to Miocene radiolarian zonation based on Sites 881–887 of ODP Leg 145. Morley and Nigrini (1995) identified several radiolarian events during the Pleistocene to Miocene. Motoyama (1996) and Kamikuri et al. (2004, 2007) conducted detailed investigations of Neogene radiolarian biostratigraphy in the subarctic Pacific employing Deep Sea Drilling Project (DSDP) Leg 19, ODP Leg 145, and ODP Leg 186 samples. They established synthetic radiolarian zones and identified detailed radiolarian events. Essentially, the radiolarian zonation given by Kamikuri et al. (2007) was used; however, the timing of radiolarian events was recalculated according to the standard geologic timescale (Lourens et al., 2004).

Sample preparation for light-microscopic observation was performed as follows. A ~3 $cm^3$ sample of wet core catcher sediment was sieved through a 63 µm mesh sieve. A microslide was prepared by pipetting the coarse fraction onto a slide glass. After the sample on the slide was dry, a glass coverslip was mounted with Norland optical adhesive. When unclear radiolarian specimens were encountered because clay and organic matter were attached to the skeletons, Calgon or 10% $H_2O_2$ was added after sieving and another microslide was prepared.

*Eucyrtidium matuyamai*, an important radiolarian stratigraphic marker occurring between 1 and 2 Ma, is a rare species (Hays, 1970). To determine the horizon of this datum, the >106 µm fractions were used in addition to the >63 µm fractions because *E. matuyamai* is generally >200 µm.

Total radiolarian abundances were determined by light-microscopic observations at 100× magnification (10× objective and 10× eyepiece lenses) as follows:

A = abundant; >200 specimens per slide traverse.
C = common; 50–200 specimens per slide traverse.
F = few; 1–49 specimens per slide traverse.
N = none; 0 specimens per slide traverse.

Radiolarian species abundances were determined by light-microscopic observations at 100× as follows (the slide traverse employed was perpendicular to the longer distance of a microslide):

A = abundant; >30 specimens per slide traverse.
C = common; 6–30 specimens per slide traverse.

F = few; 1–5 specimens per slide traverse.
N = none; 0 specimens per slide traverse.

Preservation is recorded as follows:

G = good; most specimens, including fine structures, complete.
M = moderate; minor dissolution and/or breakage.
P = poor; common dissolution and/or breakage.

## Palynology: dinoflagellate cysts, pollen, and other palynomorphs

Several types of organic-walled microfossils (i.e., palynomorphs) were recovered in palynological samples. These include dinoflagellate cysts (dinocysts), pollen and spores, organic linings of benthic foraminifers, and sometimes organic cysts and lorica of tintinnids, phycoma of prasinophyte algae, and acritarchs. During this expedition all palynomorphs were examined, but more attention was paid to dinocysts as paleoecological and biostratigraphic indicators.

To date, no integrated, world-scale, calibrated zonal schemes have been established using dinoflagellate cysts for the Neogene interval. Nevertheless, many studies document the late Cenozoic stratigraphic distribution of dinocysts at several locations of middle to high latitude in the North Atlantic Ocean (e.g., Harland, 1979; Mudie, 1987, 1989; Powell, 1988; Head et al., 1989, 2004; de Vernal and Mudie, 1989, 1992; de Vernal et al., 1992; Head and Norris, 2003; Piasecki, 2003; Louwye et al., 2004; De Schepper et al., 2008a, 2008b). Only a few studies in the North Pacific Ocean address Cenozoic biostratigraphy. Matsuoka (1983) reported some dinoflagellate cysts and acritarchs in a Japanese Cenozoic formation. For DSDP Leg 19, Bujak (1984) established the first dinocyst biozonation in the Bering Sea for which each zone was defined by the concurrent occurrence of several taxa. This zonation was then reviewed by Bujak and Matsuoka (1986a, 1986b) according to some taxonomic reconsideration. Since then, no palynological investigations have been made in the Bering Sea except for Radi et al.'s (2001) study of surface sediments.

For biostratigraphic study of Bering Sea sediments, dinocyst events were compared to the North Pacific biostratigraphic frameworks established by Bujak (1984) and Bujak and Matsuoka (1986a, 1986b), as well as to North Atlantic schemes, notably that given by De Schepper et al. (2008a, 2008b). Bering Sea dinocysts were also compared with the broad-scale succession of events and zones established by Williams and Bujak (1985), Powell (1992), and Williams et al. (1998).

### Methods

Approximately 5 $cm^3$ of sample was processed on board according to simplified palynological treatment, avoiding hydrofluoric acid treatments. The procedure included ultrasonic treatment, sieving on a 106 µm mesh in order to discard coarse material, and sieving at 15 µm to eliminate clay and fine silt particles. The fraction between 15 and 106 µm was treated with HCl (10%) to remove carbonates. The residue was then submitted to differential settling in water. Heavy liquid separation with sodium polytungstate solution was needed for most samples because of abundant diatoms and siliciclastic debris. Residues were sieved a final time on a 15 µm mesh and mounted between a slide and coverslip with glycerin jelly. To assess palynomorph concentration in wet sediment, tablets of *Lycopodium* spores were included (as a spike) in each sample at the beginning of preparation.

Slides were examined on a Zeiss Axioskop microscope equipped with differential interference contrast with magnification ranging from 200× to 400×. Taxonomic identifications were verified at 630×–1000× magnification.

The abundances of each palynomorph group (e.g., dinocysts, pollen, spores, etc.) were calculated from relative proportions of *Lycopodium* spores after the slides were scanned. Abundances are reported as follows:

A = abundant; >2000/$cm^3$.
C = common; >200–2000/$cm^3$.
F = few; 100–200/$cm^3$.
R = rare; <100/$cm^3$.

The relative abundances of dinocyst taxa are defined as follows:

D = dominant; >30%.
A = abundant; >10%–30%.
F = few; >5%–10%.
R = rare; <5%.
P = present; counts <20.

The preservation of dinocysts, and palynomorphs in general, was determined qualitatively and is reported as follows:

G = good; no alteration of organic walls; pollen and dinocysts are spherical; the least resistant taxa occur.
M = moderate; subtle indication of alteration and flattening of palynomorphs.
P = poor; only the most resistant palynomorph is present; strong alteration features and flattening; specimens are often broken.

# Paleomagnetism

## Samples, instruments, and measurements

Paleomagnetic investigations during Expedition 323 focused mainly on measuring the natural remanent magnetization (NRM) of archive-half sections before and after alternating-field (AF) demagnetization. All NRM measurements for archive-half sections were made using a 2G Enterprises model 760R superconducting rock magnetometer (SRM) equipped with direct-current superconducting quantum interference devices (SQUIDs) and an in-line automated AF demagnetizer capable of reaching a peak field of 80 mT. The coordinate systems for the SRM and the archive and working halves are shown in Figure **F9.** A new software package was developed for the SRM during Expedition 320T and modified during Expeditions 320 and 321.

The SRM and other instruments used, tested, or available in the paleomagnetism laboratory during Expedition 323 are listed in Table **T3.** This table also includes quality assessment information (e.g., sensitivity, accuracy, and precision) of the instruments as determined by experimentation, past experience, or information provided by the instrument vendors (Richter et al., 2007). For example, tests conducted with the SRM at the beginning of Expeditions 320 and 321 indicate that the ambient noise level is $<2 \times 10^{-10}$ A/m$^2$. This finding permits the measurement of split-core samples (where the volume of material measured is ~100 cm$^3$) with intensities as low as $\sim 2 \times 10^{-5}$ A/m$^2$.

NRM measurements were usually made every 2.5 cm along the split-core sections. Additionally, measurements were made over a 15 cm interval before and after the sample entered the superconducting quantum interference device (SQUID) sensors. These measurements are referred to as the header and trailer, and they serve the dual functions of monitoring background magnetic moment and allowing future deconvolution analysis. Typically, NRM was measured after 0, 10, and 20 mT AF demagnetization. Because the laboratory's core flow (the analysis of one core after the other) dictated the amount of time available for measurements (~2–3 h per core), there was not always sufficient time to perform the optimal number of demagnetization steps. During part of Expeditions 320 and 321, a 2.5 cm measurement spacing was used when extra time was available. This practice was also used during Expedition 323. Sections that were entirely visibly disturbed were not measured. Similarly, in analyzing data, measurements were culled within 5 cm of section ends and within intervals with drilling-related core disturbance (e.g., the top few to tens of centimeters of most cores).

Low-field magnetic susceptibility was measured on all whole-core sections using the WRMSL and the Special Task Multisensor Logger (STMSL) (see **"Physical properties"** and **"Stratigraphic correlation"**). The susceptibility meters are Bartington loop meters (model MS2 with an MS2C sensor with coil diameter of 88 mm); the WRMSL has an operating frequency of 0.621 kHz; the STMSL has an operating frequency of 0.513 kHz. The meters have a nominal resolution of $2 \times 10^{-6}$ SI (Blum, 1997). The "units" option for the meters was set to SI units, and the values were stored in the database in raw meter units. To convert to true SI volume susceptibilities, the recorded values should be multiplied by $0.68 \times 10^{-5}$.

## Coring and core orientation

Cores were collected using nonmagnetic core barrels except at depths at which overpull was apparent during core recovery and the more expensive nonmagnetic barrel was endangered. In addition, the bottom-hole assembly (BHA) included a Monel (nonmagnetic) drill collar when the FlexIt core orientation tool was used.

The FlexIt orientation tool was used to orient all APC cores. This instrument uses three orthogonally mounted fluxgate magnetometers to record the orientation with respect to magnetic north of the double lines scribed on the core liner. The tool also has three orthogonally mounted accelerometers that monitor the movement of the drill assembly and help determine when the most stable, and thus most useful, core orientation data are gathered. Declination, inclination, and temperature are recorded internally at regular intervals until the tool's memory capacity is filled. When measurements are taken in intervals of 6 s, which is the interval used during Expedition 323, the tool can typically be run for ~24 h. However, we attempted to switch tools at least every 8–12 h. Three FlexIt tools (serial numbers 936, 937, and 938) were available.

The tool was set up following the standard operating procedure described in the IODP manual "Core Orientation Standard Operating Procedure" (20 January 2009, available from the IODP Cumulus database). Using this procedure, the instrument was synchronized to a personal computer running the FlexIt software (version 3.5), and the tool was inserted inside a pressure casing. The enclosed tool was then given to a core technician, who installed it on the sinker bars above the core barrel. The double lines on the core liner were aligned relative to the tool. Before firing the APC, the core barrel (along with the pipe and

BHA) was held stationary for several minutes. During this time, data were recorded to constrain core orientation. When the APC fired, the core barrel was assumed to maintain the same orientation even though this and previous cruises have provided evidence that the core barrel can rotate and the core liner can twist as it penetrates the sediments. Generally, the core barrel was pulled out after a few minutes. However, for cores collected with the third-generation advanced piston corer temperature tool (APCT-3) (see **"Downhole measurements"**), the core barrel remained in the sediments for 10 or more minutes.

Because rotation between pieces of core occurs in all XCB cores collected, XCB cores were not reoriented. However, polarity can be estimated from inclination values, which are generally high in value and diagnostic.

### Magnetostratigraphy

Magnetostratigraphies for each site were constructed by correlating obtained magnetic polarity sequences with the GPTS (Table **T4**). Biostratigraphic age constraints significantly limit the range of possible correlations with the GPTS.

The GPTS used for Expedition 323 is based on the Neogene timescale constructed by Lourens et al. (2004), who placed the Paleogene/Neogene boundary at 23.030 Ma based on the astronomically derived age for the base of Chron C6Cn.2n (Shackleton et al., 2000), which was later updated to the new astronomical solution of Laskar et al. (2004) by Pälike et al. (2006).

## Geochemistry

Geochemical methods were used to quantify volatile gases and concentrations of chemical species in interstitial water and sediment. Routine shipboard safety measurements and standard shipboard analyses were used to characterize the geochemistry of the sediment. Nonstandard sampling and analyses were carried out to satisfy the various research goals of this expedition. Subsamples of interstitial water and sediment were also taken for shore-based research.

### Hydrocarbon sampling and analyses

Concentrations of volatile hydrocarbons ($C_1$–$C_6$) from sediment headspace samples were measured once per core in Hole A (all sites) and at higher resolution in microbiology-dedicated Holes U1339B, U1342B, U1343B, U1344C, and U1345B. In the latter two holes, high-resolution headspace sampling took place on the catwalk to prevent methane ($CH_4$) loss and to produce more accurate $CH_4$ profiles, particularly near the sulfate–methane transition zone (SMTZ). Sediment plugs were taken directly from holes drilled in the core liner immediately after the core was placed on the catwalk. Two cubic centimeters of sediment was put into vials containing 4 mL of sodium hydroxide. The vials were immediately capped and stored upside down until volatile hydrocarbons were measured. The holes drilled into the core liner were taped. Headspace samples were taken at a resolution of 25 cm in the uppermost 15 mbsf, avoiding areas of the core that would be sampled for interstitial water and microbiology. In all other microbiology-dedicated holes, high-resolution headspace sampling took place in the Cold Laboratory. These headspace samples were taken in the same manner as the low-resolution catwalk samples by placing ~3–5 $cm^3$ of sediment in a 20 $cm^3$ glass serum vial and sealing it with a septum and metal crimp cap. The samples were then heated at 70°C for 30 min. A 5 $cm^3$ headspace gas aliquot was removed from the vial with a glass syringe for analysis by gas chromatography.

Headspace gas samples were analyzed using an Agilent 6890 gas chromatograph (GC) equipped with a 2.4 m × 3.2 mm stainless steel column packed with 100/120 mesh HayeSep R and a flame ionization detector. This instrument measures the concentrations of methane ($C_1$), ethane ($C_2$), ethene ($C_2$=), propane ($C_3$), and propene ($C_3$=). The glass syringe was directly connected to the GC with a 1 $cm^3$ sample loop. The carrier gas was helium. The GC oven temperature was programmed to ramp at 30°C/min from 90° to 100°C and at 15°C/min from 100° to 110°C and to remain at 110°C for 4.5 min before ramping at 50°C/min to 150°C with a final holding time of 1.8 min. Data were collected and evaluated with an Agilent Chemstation data-handling program. Chromatographic response was calibrated against preanalyzed standards.

### Interstitial water sampling and chemistry

Interstitial water was extracted from 5, 10, or 15 cm whole-round sections. For microbiology-dedicated holes (U1339B, U1342B, U1343B, U1344C, and U1345B), unique sampling strategies were used (see Fig. **F10** for an example of the strategy used in Hole U1345B). Samples were centered 25 cm apart for the uppermost 3 m in Holes U1339B and U1342B, the uppermost 9 m in Hole U1343B, the uppermost 12 m in Hole U1344C, and the uppermost 13 m in Hole U1345B. The length of this very high resolution sampling interval varied in order to create high-resolution chemical profiles through the SMTZ at each

site. Cores from the microbiology-dedicated holes were cut into whole rounds in the Cold Laboratory (~7°C). Whole rounds were stored in a nitrogen-filled glove box in the Cold Laboratory until squeezed.

In Hole A at every site, three samples were taken from the top core (1H), two were taken from the second core (2H), and one was taken from the cores below Core 2H. These whole rounds were cut on the catwalk shortly after the core was brought on deck. Squeezing occurred immediately after the whole rounds were cut.

Before squeezing, samples were removed from the core liner and the outer surfaces were carefully scraped off with a clean spatula to minimize potential contamination by the coring process. Whole rounds were placed into a titanium and steel squeezing device and squeezed at ambient temperature with a hydraulic press at pressures as great as 35,000 psi using modified versions of the standard ODP stainless steel squeezer of Manheim and Sayles (1974). Interstitial water samples were collected in plastic syringes and filtered through 0.45 µm Whatman polyethersulfone disposable filters. Aliquots of interstitial water were treated and stored for shore-based analyses.

Rhizon CSS-F 5 cm core solution samplers (Rhizosphere Research Products) were also used to collect interstitial water (Seeberg-Elverfeldt et al., 2005). Rhizon samplers were soaked in distilled water for ~1 h before use. They were then carefully inserted through holes drilled in the core liner. Acid-washed syringes were attached to each Rhizon sampler, pulled to generate vacuum, and held open with wooden spacers. The first ~1 mL was discarded, and the rest was collected and aliquoted for shore-based analyses.

Interstitial water analyses followed the procedures outlined by Gieskes et al. (1991), Murray et al. (2000), and user manuals for new shipboard instrumentation, with modifications as indicated. Interstitial water was routinely analyzed for salinity with an INDEX Instruments digital refractometer. After squeezing, alkalinity (and pH) and dissolved inorganic carbon (DIC) were measured immediately by Gran titration (Gieskes and Rogers, 1973) with a Metrohm autotitrator and a UIC 5011 $CO_2$ coulometer, respectively.

Dissolved ammonium and total hydrogen sulfide ($\Sigma H_2S = H_2S + HS^-$) were determined spectrophotometrically (Shimadzu ultraviolet [UV] mini 1240 UV-Vis spectrophotometer) based on methods by Solórzano (1969) and Cline (1969), respectively. Phosphate concentrations were determined using an OI Analytical discrete analyzer (DA3500) spectrophotometer unit. Sulfate, chloride, calcium, sodium, magnesium, and potassium concentrations were determined with a Dionex ICS-3000 ion chromatograph on 1:200 diluted aliquots in 18 MΩ water.

The International Association for the Physical Sciences of the Oceans (IAPSO) seawater standard was used for standardization of alkalinity and for all measurements made on the ion chromatograph. Sodium sulfide, ammonium chloride, potassium phosphate monobasic, and calcium carbonate were used for calibration curves and as internal standards for sulfide, ammonium, phosphate, and DIC concentration measurements, respectively. There was <1% coefficient of variation (the ratio of the standard deviation to the mean) in the DIC measurements based on calcium carbonate standards run after every fifth sample. Variation for alkalinity was 1%–2% based on IAPSO runs after every fifth sample. The coefficient of variation (based on IAPSO runs after every fifth sample) measured on the ion chromatograph was 1% for anions and 1.3% for cations. The coefficients of variation for sulfide, ammonium, and phosphate (based on internal standards run after every fifth sample) were 5%, 0.5%–2%, and 0.8%, respectively.

The minor elements manganese, iron, boron, strontium, barium, silica, and lithium were determined by inductively coupled plasma–atomic emission spectroscopy (ICP-AES) with a Teledyne Prodigy high-dispersion ICP-AES. ICP-AES techniques for minor elements were modified from those described by Murray et al. (2000) by preparing calibration standards in an acidified (2% $HNO_3$, by volume) sodium chloride matrix (35 g NaCl/L). Samples and standards were diluted 1:10 using the 2% $HNO_3$ matrix solution with 10 ppm yttrium (Y) as an internal standard. When necessary, drift correction was made using the factor from a drift monitor solution (middle value standard solution), which was analyzed after every seventh sample. The coefficient of variation based on duplicate samples was typically <5% but in some cases was as high as 10%. Quantification of the major cations sodium, magnesium, calcium, and potassium by ICP-AES was only done for Site U1339 interstitial water samples. For major cations, standards (IAPSO) and samples were diluted 1:100 with 2% $HNO_3$ containing 10 ppm Y.

## Bulk sediment geochemistry

Total inorganic carbon (TIC) concentrations were determined using a UIC 5011 $CO_2$ coulometer. Samples of ~10 mg of freeze-dried ground sediment were reacted with 1 N HCl. The liberated $CO_2$ was backtitrated to a colorimetric end point. Calcium carbon-

ate content, as weight percent, was calculated from the TIC content with the assumption that all TIC is present as calcium carbonate ($CaCO_3$):

$$\%CaCO_3 = \%TIC \times 8.33.$$

The coefficient of variation was ~1%.

Total carbon (TC), total nitrogen (TN), and total sulfur (TS) contents were determined for a subset of the samples using a Thermo Electron Flash EA 1112 elemental analyzer equipped with a Thermo Electron packed column CHNS/NCS (polytetrafluoroethylene [PTFE]; length = 2 m; diameter = 6 × 5) and thermal conductivity detector (TCD). Aliquots of 10 mg of freeze-dried ground sediment in tin cups were combusted at 900°C in a stream of oxygen. Nitrogen oxides were reduced to $N_2$, and the mixture of $N_2$, $CO_2$, $H_2O$, and $SO_2$ gases was separated by GC, with detection performed by TCD. The GC oven temperature was set at 65°C. All measurements were calibrated by comparison to the standard, pure sulfanilamide. Repeated measurements of this standard gave coefficients of variation of 1%, 2%, and 6% for TC, TN, and TS, respectively. Contents of total organic carbon (TOC), as weight percent, were calculated as the difference between TC and TIC:

$$\%\ TOC = \%TC - \%TIC.$$

# Physical properties

Shipboard measurements of physical properties provide information that assists in the characterization of lithologic units, correlation of lithostratigraphy with downhole geophysical logging data, assessment of consolidation history, and interpretation of seismic reflection profiles. The primary objectives of the Expedition 323 physical properties program were to collect downhole high-resolution data to facilitate (1) calculation of mass accumulation rates (MARs), (2) hole-to-hole and site-to-site stratigraphic correlation needed for the construction of composite stratigraphic sections, (3) detection of cyclostratigraphic sequences, and (4) identification of major seismic reflectors and construction of synthetic seismic profiles.

Physical properties were first measured on whole-round core sections. Core sections are generally 1.5 m in length, so a typical coring length (stroke) of 9.5 m yields six sections plus a shorter seventh section. Two data logging systems were run on each section: (1) the "fast track" STMSL was run on sections immediately after they were sectioned on the catwalk and (2) the "slow track" WRMSL was run on core sections that had warmed to ambient laboratory temperature (19°–20°C). The linear track of the STMSL houses a GRA bulk densitometer and a magnetic susceptibility sensor. The WRMSL employs, in this order, a GRA bulk densitometer, a magnetic susceptibility sensor, and a compressional *P*-wave velocity sensor.

After WRMSL scanning, the whole-round sections were logged for NGR. Thermal conductivity was then measured on certain whole-round sections (one section per core) by a needle probe inserted into the section through a small hole drilled through the plastic core liner.

At this phase of data gathering, the sections were split into working and archive halves. Discrete samples were collected from the working halves to measure wet bulk density, dry bulk density, water content, porosity, and grain density with moisture and density (MAD) procedures. A full discussion of all methodologies and calculations used in the R/V *JOIDES Resolution* physical properties laboratory can be found in Blum (1997).

## Special Task Multisensor Logger

The purpose of STMSL logging operations during Expedition 323 was to rapidly record medium- to high-resolution sets of GRA and magnetic susceptibility data. This information was urgently needed to identify offsets in the composite section during the drilling of multiple holes. The GRA bulk densitometer and magnetic susceptibility loop incorporated in the STMSL are effectively identical to those of the WRMSL (see **"Whole-Round Multisensor Logger"**). The spacing distance between STMSL measurements was typically 5 cm for GRA measurements and 10 cm for magnetic susceptibility measurements. Scanning time averaged 8 s. STMSL scans were also run for cores collected from dedicated microbiological holes.

## Whole-Round Multisensor Logger

High-resolution WRMSL data, especially GRA bulk density and magnetic susceptibility, were gathered to advance shipboard core-to-core correlation between drill holes and the construction of composite stratigraphic sections. WRMSL data assembly had to be completed within a reasonable time to not encumber downstream core processing and sample collection. The quality of WRMSL data is highly dependent on the structural integrity and sediment fullness of the core sections. WRMSL scans were not run for cores collected from dedicated microbiological holes.

GRA bulk density and magnetic susceptibility were measured nondestructively on all whole-round core sections. Compressional wave (*P*-wave) velocity was

measured in sections undisturbed by gas expansion voids and cracks. To optimize WRMSL performance, the same sampling spacing, typically 5 cm, was set for all sensors. Measurement time, although somewhat different for the different sensors, averaged ~8 s. With handling, data initializing, and track movement, a 1.5 m section took ~10 min to scan. A 9.5 m core thus took ~1 h to pass through the WRMSL.

### Gamma ray attenuation bulk density

Bulk density is a reflection of water-saturated porosity, grain density (dominant mineralogy), grain packing, and coring disturbance. To measure bulk density the GRA densitometer uses a 10 mCi $^{137}$Cs capsule as a gamma ray source (with the principal energy peak at 0.662 MeV) and a scintillation detector. The narrow collimated peak is attenuated as it passes through the center of the core. Incident photons are scattered by the electrons of the sediment by Compton scattering.

The attenuation of the incident intensity ($I_0$) is directly related to the electron density in the sediment core of diameter (D) that can be related to bulk density given the average attenuation coefficient (in micrometers) of the sediment (Evans, 1965; Harms and Choquette, 1965). Because the attenuation coefficient is similar for most common minerals and aluminum, bulk density is obtained through direct calibration of the densitometer using aluminum rods of different diameters mounted in a core liner filled with distilled water. The GRA densitometer has a spatial resolution of <1 cm.

GRA and magnetic susceptibility calibration issues occurred during the cruise. When these were noticed, GRA calibration standards were run. Problems with bias changes in magnetic susceptibility data will be addressed on shore (see **"Physical properties calibration issues"** in the "Appendix").

### Magnetic susceptibility

Magnetic susceptibility is a measure of the degree to which a material can be magnetized by an external magnetic field. It provides information on the magnetic composition of the sediment that commonly can be related to mineralogical composition (e.g., terrigenous versus biogenic materials) and diagenetic overprinting. Magnetite and a few other iron oxides with ferromagnetic characteristics have a specific magnetic susceptibility several orders of magnitude higher than clay, which has paramagnetic properties. Carbonate layers, opal, water, and plastic (core liner) have small negative values of magnetic susceptibility. Calcareous and siliceous (diatomaceous) deposits with low clay and iron-bearing mineral debris content thus have values approaching the detection limit of magnetic susceptibility meters.

Magnetic susceptibility was measured on the WRMSL and STMSL with the Bartington Instruments MS2C system. The frequency at which the magnetic susceptibility loop operates is 621 Hz for the WRMSL and 513 Hz for the STMSL. The output of the magnetic susceptibility sensors can be set to centimeter-gram-second (cgs) units or SI units, the IODP standard. However, to obtain dimensionless SI volume-specific magnetic susceptibility values, the instrument units stored in the IODP database must be multiplied by a correction factor to compensate for instrument scaling and the geometric ratio between core and loop dimensions.

### Compressional *P*-wave velocity

*P*-wave velocity varies with the material's lithology, porosity, and bulk density, as well as state of stress, temperature, and fabric or degree of fracturing. In sediment and rock, velocity is controlled by the degree of consolidation and lithification, fracturing, and occurrence and abundance of free gas and gas hydrate. Together with bulk density, velocity data are used to calculate acoustic impedance and reflection coefficients to construct synthetic seismic profiles and to estimate the depth of specific seismic horizons.

The *P*-wave velocity sensor measures the ultrasonic *P*-wave velocity of the whole-round sample residing in the core liner. The *P*-wave logger transmits a 500 kHz *P*-wave pulse across the core section at a specified repetition rate.

Traveltime is determined by signal processing software that automatically detects the first arrival of the *P*-wave signal to a precision of 50 ns. Ultrasonic *P*-wave velocity is calculated after correcting for system propagation delay, liner thickness, and liner material velocity.

## Natural gamma radiation

The NGRL was designed and built at the Texas A&M University IODP-USIO facility. The NGRL measures gamma rays emitted from whole-round core sections. Gamma rays detected by the logger arise primarily from the decay of mineral-hosted uranium, thorium, and potassium isotopes. In general, high counts identify fine-grained deposits containing K-rich clay minerals and their absorbed U and Th atoms. The NGRL maps fine stratigraphic details that importantly aid in core-to-core correlations.

The main NGR detector unit consists of 8 sodium iodide (NaI) scintillator detectors surrounding the

lower half of the section, 7 shielding plastic scintillator detectors, 22 photomultipliers, and a passive lead shielding. The NaI detectors are covered by at least 8 cm of lead shielding. In addition, lead separators (~7 cm of low background lead) are positioned between the NaI detectors. Half of the lead shielding closest to the NaI detectors is composed of low-background lead, whereas the outer half is composed of common (virgin) lead. In addition to this passive lead shielding, the overlying plastic scintillators detect incoming high-energy gamma and muon cosmic radiation and cancel this signal from the total counted by the NaI detectors.

A measurement run consists of counting two positions on each core section for at least 5 min each for a total of 16 measurements per 150 cm section. Typically, core-section logging required ~15 min; thus, with handling and data management, the processing of a 9.5 m core required ~1.5 h.

## Thermal conductivity

After NGR measurements were completed, thermal conductivity was measured with the TK04 (Teka Bolin) system using the needle-probe method in full-space configuration for whole-round sediment cores (Von Herzen and Maxwell, 1959). The needle probe contains a heater wire and calibrated thermistor. The probe was inserted into a 2 mm hole drilled through the liner along one of the lines that later guided the splitting of the core. Because an air conditioning vent was located directly over the thermal conductivity station, an insulating jacket of foam rubber was placed over the core section during measurement of thermal conductivity. A thermal transfer compound was used to improve the coupling between the needle and the sediment.

Because the probe is much more conductive than unconsolidated sediment, the probe is assumed to be a perfect conductor. Under this assumption, the temperature of the superconductive probe has a linear relationship with the natural logarithm of the time after the initiation of the heat:

$$T(t) = (q/4\pi k) \times \ln(t) + C,$$

where

- $T$ = temperature (K),
- $q$ = heat input per unit length per unit time (J/m/s),
- $k$ = thermal conductivity (W/[m·K]),
- $t$ = time after the initiation of the heat (s), and
- C = instrumental constant.

Two measuring cycles were automatically performed at each probe location to calculate average conductivity. A self-test, which included a drift study, was conducted at the beginning of each measurement cycle. Once the probe temperature stabilized, the heater circuit was closed and the temperature rise in the probe was recorded. Thermal conductivity was calculated from the rate of temperature rise while the heater current was flowing. Temperatures measured during the first 150 s of the heating cycle were fitted to an approximate solution of a constantly heated line source (for details, see Kristiansen, 1982; Blum, 1997). Measurement errors were 5%–10%. At sites where in situ temperatures were measured, thermal conductivity was corrected for in situ temperature and pressure as part of the calculation of heat flow. Thermal conductivity measurements were routinely taken in one section per core, typically Section 2 because Section 1 was often disturbed. Thermal conductivity measurements were not taken for holes dedicated to microbiological sampling.

## Moisture and density

After the completion of thermal conductivity measurements, whole-round cores were split into working and archive halves. The working halves were placed on the sampling table for the collection of discrete samples to determine wet and dry bulk density, grain density, water content, and porosity. In soft sediment, ~10 $cm^3$ samples were collected with a plastic syringe whose diameter fit that of the glass vial. An attempt was made to sample two or three sections per core at the 29–31 cm position. Samples were placed in numbered, preweighed 16 mL Wheaton glass vials for wet and dry sediment weighing, drying, and wet and dry volume measurements. Lithified sediments—volcaniclastic siltstone, sandstone, and coarser breccia beds—were recovered from basement rock cored at Site U1342. No shipboard MAD properties were measured on these basement cores. The weights of wet and dry sample masses were determined to a precision of 0.005 g using two Mettler Toledo electronic balances and a computer averaging system to compensate for the ship's motion.

Dry sample volume was determined using a hexapycnometer system of a six-celled, custom-configured Micromeritics AccuPyc 1330TC helium-displacement pycnometer. The precision of each cell is 1% of the full-scale volume. Volume measurement was preceded by three purges of the sample chamber with helium warmed to ~28°C. Three measurement cycles were run for each sample. Periodically, a solid metallic reference volume was placed sequentially in one of the chambers to check for instrument drift and systematic error. The volumes of the numbered Wheaton vials were calculated before the cruise by multiplying each vial's weight against the average

density of the vial glass. Dry mass and volume were measured after samples were heated in an oven at 105° ± 5°C for 24 h and allowed to cool in a desiccator. The procedures for the determination of these physical properties comply with the American Society for Testing and Materials (ASTM) designation (D) 2216 (ASTM International, 1990). The fundamental relation and assumptions for the calculations of all physical property parameters are discussed by Blum (1997) and summarized below in **"Mass and volume calculation"** and **"Calculation of bulk properties."**

### Mass and volume calculation

Wet mass ($M_{wet}$), dry mass ($M_{dry}$), and dry volume ($V_{dry}$) were measured in the laboratory. The ratio of mass (rm) is a computational constant of 0.965 (i.e., 0.965 g of freshwater per 1 g of seawater). Salt precipitated in sediment pores during the drying process is included in the $M_{dry}$ and $V_{dry}$ values. The mass of the evaporated water ($M_{water}$) and salt ($M_{salt}$) in the sample are given by $M_{water} = M_{wet} - M_{dry}$ and $M_{salt} = M_{water}\,[s/(1 - s)]$, respectively, where $s$ = the assumed saltwater salinity (0.035%) corresponding to a pore water density ($\rho_{pw}$) of 1.024 g/cm$^3$ and a salt density ($\rho_{salt}$) of 2.22 g/cm$^3$. The corrected mass of pore water ($M_{pw}$), volume of pore water ($V_{pw}$), mass of solids excluding salt ($M_{solid}$), volume of salt ($V_{salt}$), volume of solids excluding salt ($V_{solid}$), and wet volume ($V_{wet}$) are, respectively,

$$M_{pw} = (M_{wet} - M_{dry})/\mathrm{rm},$$

$$V_{pw} = M_{pw}/\rho_{pw},$$

$$M_{solid} = M_{wet} - M_{pw},$$

$$M_{salt} = M_{pw} - (M_{wet} - M_{dry}),$$

$$V_{salt} = M_{salt}/\rho_{salt},$$

$$V_{wet} = V_{dry} - V_{salt} + V_{pw},$$

and

$$V_{solid} = V_{wet} - V_{pw}.$$

### Calculation of bulk properties

For all sediment samples, water content (w) is expressed as the ratio of mass of pore water to wet sediment (total) mass,

$$w = M_{pw}/M_{wet}.$$

Wet bulk density ($\rho_{wet}$), dry bulk density ($\rho_{dry}$), sediment grain density ($\rho_{solid}$), porosity ($\phi$) and void ratio (VR) are calculated as follows:

$$\rho_{wet} = M_{wet}/V_{wet},$$

$$\rho_{dry} = M_{solid}/V_{wet},$$

$$\rho_{solid} = M_{solid}/V_{solid},$$

$$(\phi) = V_{pw}/V_{wet},$$

and

$$VR = V_{pw}/V_{solid}.$$

Moisture and density properties reported and plotted in the "Physical properties" sections of all site reports were calculated with shipboard-prepared Excel spreadsheets.

### Formation factor

Formation factor ($F$) was determined from electrical conductivity measurements taken every 10 or 20 cm on the split-core sediments from the top three to five cores from Holes U1339A, U1342A, U1343E, U1344A, and U1345A. Two in-line electrodes (1.5 cm in length and spaced 1 cm apart) mounted on a block of nonconducting grade PTFE and attached to a Metrohm 712 conductometer were inserted into the split-core sediments. This method is based on McDuff and Ellis (1979).

At each sampling location, measurements of sediment conductivity (the inverse of resistivity [$R_{core}$]) were made. Measurements of conductivity for room-temperature seawater ($R_{sw}$) were made regularly so that formation factor, $F = R_{core}/R_{sw}$, could be calculated. Both sediment and seawater were equilibrated to ambient laboratory temperature. Temperature measurements on both were made with each conductivity measurement.

This simple method for determining formation factor does not take into account surface conductivity effects of the sediment matrix. However, this is not of concern in high-porosity sediments where the conductive pathways depend dominantly on intergranular porosity and pore connectivity, even where the sediment matrix contains significant clays.

## Stratigraphic correlation

It was necessary to recover complete stratigraphic sections to meet the scientific objectives of Expedition 323. Continuous sedimentary sections cannot be recovered from a single IODP borehole because core-recovery gaps occur between successive APC and XCB cores despite 100% or more nominal recovery (Ruddiman et al., 1987; Hagelberg et al., 1995). The construction of a complete section, referred to as

a splice, requires the combination of stratigraphic intervals from two or more holes cored at the same site. To maximize the probability of bridging gaps between successive cores in individual holes, the starting depths below seafloor from which cores are recovered are offset between holes. This practice ensures that most missing sedimentary sections from inter-core gaps within a given hole are recovered in one or more adjacent holes. Usually at least two complete holes and a third partial hole must be cored to recover a complete section in the APC portion at a site. Additional complete holes are cored to allow for the construction of alternate splices, where possible.

The composite section and splice construction methodology employed during Expedition 323 follows the basic strategy originally developed during ODP Leg 138 (e.g., Hagelberg et al., 1992) and later refined during other legs. This strategy is now common practice on all high-resolution paleoceanographic expeditions. Our approach was modeled after that of ODP Leg 202, in which initial STMSL analyses of magnetic susceptibility and (new to Expedition 323) GRA bulk density were used to develop preliminary composite depths to inform drilling decisions; a more refined scale was developed as more detailed information became available (Mix, Tiedemann, Blum, et al., 2003).

The goals for stratigraphic correlation, in order of priority, were to

1. Guide drilling to ensure recovery of a complete stratigraphic section;
2. Establish a composite depth scale;
3. Define a stratigraphically complete and representative sampling splice and, if possible, one or more alternate splices;
4. Link core depths to logging depths at sites where logging was done; and
5. Evaluate and, if possible, refine shipboard stratigraphic age models by synthesizing all available age information, including the potential for tuning lithologic variations to reference records.

As a result of this stratigraphic correlation process, several depth models were created. Table **T5** summarizes these depth models and their ODP equivalents. Detailed discussion of the definitions of these depth scales and the process by which they are created follows.

## Core depth below seafloor (CSF-A)

Initial depths for the top and bottom of each core are assigned during drilling based on the length of the drill string below the ship's drilling rig floor and the length of the recovered sediment. In IODP this depth scale is referred to as CSF-A, which is equivalent to the ODP scale mbsf. As a convention, recovered core is reported in mbsf throughout this volume.

The zero depth point on the CSF-A scale is defined by the mudline in the first core of each hole. It is often difficult to tell whether this empirical mudline recovers the true sediment/water interface. Some holes are purposely (or inadvertently) started below the sediment/water interface. In this case, the zero depth point in CSF-A units may be substantially offset from the zero depth point in adjacent holes that successfully recover the sediment/water interface.

Within each core, CSF-A depths are calculated based on the drilling depth to the top of the core and by adding the depth offset of each data point within a section to the sum of the overlying sections' "created lengths," which are the lengths of the core liner sections measured with a ruler on the core-receiving platform (i.e., the "catwalk"). A different length of section, referred to as "last observed length," is recorded as the section length in the LIMS, but the created lengths are used for calculating CSF-A depths. Another length measurement called "curated length" is available in the LIMS but was not used during Expedition 323.

Stratigraphic correlation relies on comparisons between holes and numerical adjustment of the depths of various data collected on several nonintrusive sensing tracks (detailed below). Depths assigned to individual data points on the various tracks are based on offsets from the top of each section end cap, as sensed by a laser indexer unique to each track, as well as relative movements of the core sections or sensors in each track system. Early in the cruise, some discrepancies in the offsets within sections for the various tracks were observed. The software for each track was adjusted to attempt to correct these discrepancies. When discrepancies occurred, the depth registration of WRMSL magnetic susceptibility was used as the reference depth when possible. This depth was chosen as the reference because WRMSL magnetic susceptibility was generally the data set with the highest signal-to-noise ratio and the measurements were relatively insensitive to issues of calibration drift. Errors in depth assignment of track data within sections are small—in most cases <1 cm. Errors between sections caused by the use of created lengths to determine core depth may be as large as several centimeters, especially deep in each core, where the sum of several section-created lengths is used in the depth calculation. In spite of these potential errors, the use of created lengths provides consistency in the database (i.e., the depths are precise, even if not completely accurate).

The CSF-A scale is also inaccurate because of ship heave (which is not compensated for in APC coring), tidal variations in sea level, and other sources of error. Tidal influence on shot depth was first predicted during Leg 138 (Hagelberg et al., 1995) and was proven by correlation of affine offset changes and tide height during Leg 202 (Mix, Tiedemann, Blum, et al., 2003). In an attempt to remove tidal influence from the drilling depths, deep-ocean tidal predictions for all Expedition 323 drill sites were obtained from Dr. Gary Egbert at Oregon State University (pers. comm., 2009). Dr. Egbert provided output on sea-surface height from two different tidal prediction models to optimize drilling strategy. These site-specific tidal corrections were used throughout Expedition 323 to adjust drilling depths relative to the ship.

## Core composite depth below seafloor (CCSF-A)

Before a splice can be constructed, cores from various holes must be stratigraphically correlated with each other. Such correlation transfers the initial estimates of drilling depth (CSF-A) into a composite depth scale referred to as core composite depth below seafloor, appended (CCSF-A). This depth scale is approximately equivalent to the ODP depth scale meters composite depth (mcd).

The CCSF-A scale is initiated by choosing the uppermost sediment in the first core (commonly referred to as the "mudline") in a single hole that best represents the sediment/water interface. At each site, this selected core becomes the "anchor" in the composite depth scale for all holes and is usually the only core for which depths are the same on both the CSF-A and CCSF-A scales. From this anchor, core logging data are correlated among holes downsection. For each core, depth offsets, or affine values, are chosen to best align observed lithologic variations among the equivalent cores in adjacent holes. An affine value specific to each core is added to the CSF-A depth in sequence downhole.

It is not possible to perfectly align all features between holes, so affine values are chosen where possible to maximize correlations at the same precision that splice tie points are defined between holes (see **"Splice (CCSF-D),"** below).

### Data sources for depth scale construction

An initial composite depth scale was created during Expedition 323 using data from loop magnetic susceptibility and GRA bulk density from the ship's STMSL, based on recommendations from Leg 202 (Mix, Tiedemann, Blum, et al., 2003). This initial scale was developed during drilling for the primary purpose of guiding drilling in subsequent holes in an attempt to recover the full stratigraphic section.

The final CCSF-A scale and the splice for each site are based primarily on correlation of data from the *JOIDES Resolution*'s WRMSL, which measures GRA bulk density (a function of grain density and porosity) and loop magnetic susceptibility. These WRMSL GRA bulk density and magnetic susceptibility data generally replaced the STMSL data; however, cores from holes dedicated to microbiology experiments were only analyzed on the STMSL, and these data were recorded and archived so that these special-purpose cores could be incorporated into the composite depth framework. Comparison of STMSL and WRMSL core logging data also led us to detect calibration drift in the sensor, which was corrected during the expedition whenever possible. The WRMSL also measures *P*-wave velocity and noncontact resistivity, but these data were not useful for correlation purposes, and to save time these sensors were used only intermittently during Expedition 323.

Correlations based primarily on GRA bulk density and magnetic susceptibility data were augmented by data from the NGRL and digital color reflectance parameters L*, a*, and b* measured on the SHMSL, which also records high-resolution reflectance spectra. This track also normally measures high-resolution point-source magnetic susceptibility (MSLP), but the MSLP system was not functioning during Expedition 323. High-resolution color digital images were analyzed on the SHIL, which provides color digital images that were incorporated, for the first time, in the correlation procedures during Expedition 323. These measurements are described in greater detail in **"Physical properties."** Core logging data were collected at 2.5, 5, or 10 cm intervals depending on time and core flow.

### Composite depth scale construction

Raw stratigraphic data were imported into the beta-test versions of the specialized shipboard software program "Correlator" (versions 1.65, 1.652, 1.655, 1.656, and 1.657) and linked to digital core images with the program "Corelyzer" (versions 1.2.9.1, 1.3.2, and 1.3.3). Input data for these programs were downloaded from the ship's LIMS database using several versions of "Correlator Download." Upload of the resulting depth models to the LIMS was attempted with "AffineSpliceUploader," and management of various depth scales was attempted with "Depth Manager." These programs were sequentially modified to resolve problems that arose during Expedition 323, and they will be further modified before they become fully operational programs for IODP expeditions.

Correlator enables the graphical construction of a composite depth scale for each hole at a given site by depth-shifting individual cores to maximize the correlation of core logging data among multiple holes. For hole-to-hole correlations and plotting results, data were masked to avoid incorporating anomalous data influenced by edge effects at section boundaries or at core tops or in voids where no sediment was present; however, all original data were retained in the LIMS database.

Depth intervals within cores are not squeezed or stretched by Correlator; thus, it is not possible to align all correlative features within each core. Stretching or squeezing between cores from different holes may reflect small-scale differences in sedimentation and/or distortion caused by the coring and archiving processes. For example, the tops of APC cores are often stretched and the bottoms compressed, although this depends on lithology and the extent of lithification. In addition, sediment of unknown age occasionally falls from higher levels in the borehole onto the tops of cores as they are recovered, and as a result the top depths of some cores are unreliable. Gas expansion caused voids within some core sections. When this happened, holes were drilled into the liners and the sediment was manually pushed into the core liners to minimize the occurrence of these voids, which compromise track data. Where holes were drilled, pressurized sediment often extruded in wormlike streams. Although drilling holes in the core liner improves the continuity of data used for correlation in gassy sediments, it may also cause artificial distortion of depths within cores. Gas expansion also frequently extruded sediment out of the top of cores before the cores could be archived. The extruded material was recovered from the drilling rig floor and reassembled as Section 1 in many cores. Although great care was taken to assemble these sections in stratigraphic order, these assemblies are severely disturbed and may be missing some intervals. Where possible, the splice excludes these disturbed sections.

Correlation among cores from adjacent holes was evaluated visually and statistically (by cross-correlation). The depth offsets for each core that are needed to convert CSF-A to CCSF-A scales are recorded in an affine table for each site. The CCSF-A depth for any point within a core equals the CSF-A depth plus the affine offset. Correlation at finer resolution is not possible with Correlator because depth adjustments are applied linearly to individual cores; at this stage of depth-scale development, no adjustments in the length of each core, such as numerical squeezing and stretching, are made within cores. Such finer scale adjustment of individual cores relative to the splice (e.g., Hagelberg et al., 1995; Pälike et al., 2005) or logging data (e.g., Harris et al., 1995) can be done after the development of the composite section.

Ideally, the base of the continuous CCSF-A scale is the bottom of the deepest core recovered from the deepest hole. In practice, however, the base often occurs where core recovery gaps align across all holes, and the construction of a splice is impossible. Cores below this interval cannot be directly tied into the overlying "continuous" CCSF-A scale. However, below the base of the continuous section in CCSF-A units, cores from two or more holes can sometimes be correlated with each other, allowing the generation of a "floating" CCSF-A scale for intervals deeper than the continuous CCSF-A scale. In these cases, cores in the interval with no overlap were "appended" using the affine value of the overlying cores, and a floating splice was added below the appended interval. Because Correlator could not handle situations with multiple appended cores, these values were calculated manually. In one case (Site U1339), the observation that gaps between cores (the differential affine offset plus the drill pipe advance less core recovery) within the correlated section were relatively constant (i.e., the growth rate in the affine values as a function of drilling depth was linear) was used to assign cores below the splice an extrapolated affine value that yields an extrapolated CCSF-A scale with gaps. At other sites, long appended intervals use a constant affine value assigned to drilling depths.

The length of the CCSF-A scale at a given site is typically ~10%–20% greater than the length of the cored section in any one hole as indicated by the CSF-A scale. Although the exact reasons for this apparent expansion of the sediment column are unknown, expansion is commonly attributed to rebound that follows the release of overburden in the deeper sections, stretching during the coring process, gas expansion during the core recovery process, and other factors (Moran, 1997).

## Corrected core composite depth below seafloor (CCSF-B)

Scaled CCSF (CCSF-B) is a depth scale intended to correct the CCSF-A, CCSF-C, or CCSF-D scales for empirically observed expansion. CCSF-B can be produced by dividing various CCSF depth values by the average affine growth value of the CCSF-A scale relative to the CSF-A scale over a sufficiently long interval for which random variations in drill pipe advance caused by ship heave, tides, and other factors are negligible. This produces a complete stratigraphic sequence that is the same length as the total depth

cored. The CCSF-B scale is assumed to be a close approximation of the actual drilled interval in the sediment column, although this is difficult to verify in intervals not covered by wireline logging. During Expedition 323, CCSF-B scales were not created, but affine growth factors were provided so that users could create them as needed.

## Splice (CCSF-D)

The splice is a composite core section representing the best available representation of a complete stratigraphic column at a site. It is composed of core sections from adjacent holes such that coring gaps in one hole are filled with core from an adjacent hole. The splice does not generally contain coring gaps, and an effort was made to minimize inclusion of disturbed sections by examining core photographs. The shipboard splice is ideally suited to guide core sampling for detailed paleoceanographic studies. A splice table and a figure that summarize the tie points between intervals from each hole used to construct the splice are presented in each site chapter. The portion of the CCSF-A depth scale applied to the splice is referred to as CCSF-D. Within the splice sections, CCSF-D is identical to CCSF-A.

The choice of splice tie points is somewhat subjective. The method used in the construction of a splice employed three rules. First, when possible, the top and bottom 50 cm of core, where disturbance from drilling artifacts (even if not apparent in core logging data) was most likely, were not used. Reassembled first sections of cores that were severely disturbed were also not used unless they were the only representations of a sedimentary interval. Second, attempts were made to incorporate the realizations of the stratigraphic section that were judged most representative of the holes recovered. Third, a minimum number of tie points was used (i.e., the longest possible sections within individual cores were used) to simplify sampling.

When possible, additional shipboard splices were constructed so that more than one copy of a complete stratigraphic section was available for high-resolution sampling. When this was done, multiple splices were given depth scales designated as CCSF-D. Note, however, that because of stretching and squeezing within cores, some features may not correlate precisely between the different splices. Therefore, the final composite depth scale, CCSF-D, is only formally defined in the primary shipboard splice. Composite depth scales for any alternate splices are also CCSF-D scales, but these scales are slightly different than CCSF-D in the primary splice. To avoid confusion, alternate splices can be designated numerically (e.g., CCSF-D2, CCSF-D3, etc.) depending on the number of additional splices. A solution to the problem of comparing different splices is to create an additional depth scale that numerically stretches and squeezes features into a splice-correlated scale (CCSF-C). Such scales are applied to individual holes and thus may be discontinuous. In the ODP program such a scale was referred to as revised meters composite depth (rmcd). Splice-correlated scales were not created during Expedition 323 because of software limitations.

## Core-log integration (CCSF-L)

For sites that were logged, high-quality logging data allow for core-log integration in which cored intervals are squeezed or stretched and the zero depth point of the wireline log is linearly shifted up or down to maximize correlation between core logs and wireline logs. Core-log integration produces yet another depth scale. In ODP such depths were referred to as equivalent logging depths (eld). In IODP such a depth scale might be referred to as CCSF-C because it is a variant of the CCSF scale modified by correlation. However, this presents the potential for confusion between a CCSF-C scale developed to link all CCSF depths to the primary splice and a CCSF-C scale developed to correlate cores and logs. A new definition should be created specifically for depths modified to correlate with logging depths. This construct is tentatively referred to as CCSF-L.

The CCSF-L scale typically begins at ~100 mbsf, where the drill pipe is positioned during logging operations. When available, and when logging data are of sufficient quality, CCSF-L is the best estimate of in situ depth and so is ideal for calculating MARs and other products that require knowledge of absolute depths. Errors in wireline log depths can occur when ship heave is significant relative to heave compensation of the wireline.

A specialized module in Correlator is used to determine CCSF-L. Raw data are culled and smoothed as necessary to ensure that bad data are not included in the integration and that log and core data are compatible. Because core logging data are typically higher resolution than downhole logging data, it is necessary to smooth core logs before comparing them with downhole logs. Correlator allows correlation of individual cores within different holes with the data series recovered from logging. Core-log integration was attempted for all Expedition 323 holes in which downhole logging occurred. Unfortunately, although Correlator is capable of correlating cores and logs, it could not output the data correctly. Given time limitations, efforts at core-log integration were abandoned during the expedition pending corrections to the software. Determination of the

CCSF-L depth scale will be accomplished during postcruise study when the problems with Correlator are resolved.

### Depths in splice tables versus LIMS depths

Discrepancies in CSF-A and CCSF-A (CCSF-D) depths of as much as ±50 cm were found between the LIMS and Correlator. These discrepancies resulted from incorrect calculation on the Correlator-referred onboard splice table provided by the stratigraphic correlators, even though the onboard affine tables for each hole at the particular sites provided correct CCSF-A depths. After the new version of Correlator (version 1.66) was developed during postcruise study, output depths in the splice tables for all sites from Correlator were consistent with CSF-A depths in the LIMS. The shipboard splice tables include small differences (±5 cm) between calculated depth and measured depth that were derived from a calculation of interpolation of the tie points by using shipboard nondestructive measurements.

## Downhole measurements

Downhole logs are used to determine physical, chemical, and structural properties of the formation penetrated by a borehole. The data are rapidly collected, continuous with depth, and measured in situ; they can be interpreted in terms of the stratigraphy, lithology, mineralogy, and geochemical composition of the penetrated formation. When core recovery is incomplete or disturbed, logging data may be the only means to characterize the borehole section. When core recovery is good, log and core data complement one another and may be interpreted jointly.

Downhole logs measure formation properties on a scale intermediate between the scales obtained from laboratory measurements of core samples and geophysical surveys. They are useful in calibrating the interpretation of geophysical survey data (e.g., through the use of synthetic seismograms) and provide a necessary link for the integrated understanding of physical properties on all scales.

### Wireline logging

During wireline logging, downhole logs were made with a variety of Schlumberger logging tools that were combined into tool strings and run down the hole after coring operations were complete. Two tool strings were used during Expedition 323: a triple combination or "triple combo" tool string, which measured gamma radiation, porosity, density, and resistivity, and the Formation MicroScanner (FMS)-sonic tool string, which gathered resistivity images of the borehole wall and sonic velocities (Fig. **F11;** Table **T6**). Each tool string also contained a telemetry cartridge for communicating through the wireline to the Schlumberger data acquisition system (the MAXIS unit) on the drillship.

In preparation for logging, the boreholes were flushed of debris by circulating a "pill" of viscous drilling fluid (sepiolite mud mixed with seawater; approximate density = 8.8 lb/gal [1.055 g/cm$^3$]) through the drill pipe to the bottom of the hole. The BHA was pulled up to 60–80 mbsf. The tool strings were then lowered downhole by a seven-conductor wireline cable in sequential runs. A new wireline heave compensator (WHC) was employed to minimize the effect of the ship's heave on the tool position in the borehole (see below). During each logging run, incoming data were recorded and monitored in real time on the Schlumberger Minimum Configuration Maxis (MCM) logging computer. The tool strings were then pulled up at constant speed, typically 250–300 m/h, to provide continuous measurements of several properties simultaneously.

### Logged sediment properties and tool measurement principles

The logged properties and the methods by which they were measured are briefly described below. The main logs are listed in Table **T7.** More detailed information on individual tools and their geological applications may be found in Ellis and Singer (2007), Goldberg (1997), Lovell et al. (1998), Rider (1996), Schlumberger (1989, 1994), and Serra (1984, 1986, 1989). A complete online list of acronyms for Schlumberger tools and measurement curves is provided at **www.slb.com/modules/mnemonics/index.aspx.**

### Natural radioactivity

The Hostile Environment Gamma Ray Sonde (HNGS) was included in both tool strings to measure and classify natural radioactivity in the formation. The HNGS uses two bismuth germanate scintillation detectors and five-window spectroscopy to determine concentrations of potassium, thorium, and uranium (K, Th, and U). The radioactive isotopes of these elements dominate the natural radiation spectrum. The HNGS filters out gamma ray energies below 500 keV, eliminating sensitivity to bentonite or KCl in the drilling mud and improving measurement accuracy. Its inclusion in both tool strings allows the use of gamma ray data for depth correlation between logging strings and passes.

## Density

Formation density was determined with the Hostile Environment Litho-Density Sonde (HLDS). The sonde contains a radioactive cesium ($^{137}$Cs) gamma ray source (622 keV) and far and near gamma ray detectors mounted on a shielded skid, which is pressed against the borehole wall by a hydraulically activated eccentralizing arm. Gamma rays emitted by the source undergo Compton scattering, where gamma rays are scattered by electrons in the formation. The number of scattered gamma rays that reach the detectors is proportional to the density of electrons in the formation, which is in turn related to bulk density. Porosity also may be derived from bulk density if the matrix (grain) density is known. Good contact between the tool and the borehole wall is essential for good HLDS logs; poor contact results in underestimation of density values.

The HLDS also measures photoelectric absorption as the photoelectric effect (PEF). Gamma rays are photoelectrically absorbed when their energy is reduced below 150 keV by being repeatedly scattered by electrons in the formation. Because PEF depends on the atomic number of the elements in the formation, it also varies according to the chemical composition of the minerals present and can be used to identify some minerals. For example, the PEF of calcite = 5.08 barns per electron (b/e$^-$), illite = 3.03 b/e$^-$, quartz = 1.81 b/e$^-$, and kaolinite = 1.49 b/e$^-$.

## Porosity

Formation porosity was measured with the Accelerator Porosity Sonde (APS). The APS incorporates a minitron neutron generator that produces fast (14.4 MeV) neutrons and five neutron detectors (four epithermal and one thermal) positioned at different spacings from the minitron. The tool's detectors count neutrons that arrive at the detectors after being scattered and slowed by collisions with atomic nuclei in the formation.

The highest energy loss occurs when neutrons collide with hydrogen nuclei, which have practically the same mass as the neutron (the neutrons simply bounce off of heavier elements without losing much energy). If hydrogen (i.e., water) concentration is low, as in low-porosity formations, neutrons can travel farther before being captured, and the count rates increase at the detector. The opposite effect occurs in high-porosity formations where water content is high. However, because hydrogen that is bound in minerals such as clays or in hydrocarbons also contributes to the measurement, the raw porosity value is often an overestimate.

Upon reaching thermal energies (0.025 eV), neutrons are captured by the nuclei of Cl, Si, B, and other elements, resulting in a gamma ray emission. This neutron-capture cross section ($\Sigma_f$) is also measured by the APS.

## Electrical resistivity

The phasor dual induction–spherically focused resistivity tool (DITE-SFL) was used to measure electrical resistivity. The DITE-SFL provides three measures of electrical resistivity, each with a different depth of investigation into the formation. The two induction devices (deep and medium depths of penetration) transmit high-frequency alternating currents through transmitter coils, creating magnetic fields that induce secondary currents in the formation. These currents produce a new inductive signal, proportional to the conductivity of the formation, that is measured by the receiving coils. The measured conductivities are then converted to resistivity (in units of ohm-meters). Spherically focused resistivity is measured by an electrode device that sends a current into the formation. The amount of current needed to maintain a constant drop in voltage gives a direct measure of resistivity. This device uses several electrodes to focus current flow into the formation so that equipotential surfaces are spherical, and it has a higher vertical resolution than induction measurements. Calcite, silica, and hydrocarbons are electrical insulators, whereas ionic solutions like pore water are conductors. Electrical resistivity, therefore, can be used to evaluate porosity (via Archie's law) for a given salinity and resistivity of the pore water.

## Acoustic velocity

The Dipole Sonic Imager (DSI) measures the transit times between sonic transmitters and an array of eight receivers. It combines replicate measurements, thus providing a measurement of compressional velocity through sediments that are relatively free from the effects of formation damage and an enlarged borehole (Schlumberger, 1989). Along with the monopole transmitters found on most sonic tools, the DSI also contains two cross-dipole transmitters that allow for the additional measurement of shear wave velocity. Dipole measurements are necessary to measure shear velocity in slow formations whose shear velocities are less than the velocity of sound in the borehole fluid. Such slow formations are typically encountered in deep-ocean drilling.

### Formation MicroScanner

The FMS provides high-resolution electrical resistivity images of borehole walls. The tool has four orthogonal arms and pads, each containing 16 button electrodes that are pressed against the borehole wall during recording. The electrodes are arranged in two diagonally offset rows of eight electrodes each. A focused current is emitted from the button electrodes into the formation, with a return electrode near the top of the tool. Formation resistivity at the button electrodes is derived from the intensity of the current passing through the button electrodes. Processing transforms these measurements into oriented high-resolution images that reveal the geologic structures of the borehole wall. Features such as bedding, fracturing, slump folding, and bioturbation can be resolved; the images are oriented to magnetic north so that fabric analysis can be carried out and the dip and direction (azimuth) of planar features in the formation can be measured.

The maximum extension of the FMS caliper arms is 15 inches. In holes having >15 inch diameters, pad contact is inconsistent and the FMS images may appear out of focus and too conductive. Irregular (rough) borehole walls also adversely affect the images if contact with the wall is poor.

### Accelerometry and magnetic field measurement

Three-component acceleration and magnetic field measurements were made with the General Purpose Inclinometry Tool (GPIT). The primary purpose of this tool, which incorporates a three-component accelerometer and a three-component magnetometer, is to determine the acceleration and orientation of the FMS-sonic tool string during logging. Thus, the FMS images can be corrected for irregular tool motion, and the dip and direction (azimuth) of features in the FMS image can be determined. During Expedition 323, the GPIT was also used to record downhole tool motion and evaluate in real time the performance of the new heave compensator.

## Logging data quality

The principal influence on logging data quality is the condition of the borehole wall. If borehole diameter varies over short intervals because of washouts during drilling or ledges made of layers of harder material, the logs from tools that require good contact with the borehole wall (i.e., FMS and density tools) may be degraded. Deep investigation measurements such as resistivity and sonic velocity, which do not require contact with the borehole wall, are generally less sensitive to borehole conditions. Very narrow ("bridged") sections also cause irregular log results. The quality of the borehole is improved by minimizing the circulation of drilling fluid while drilling, flushing the borehole to remove debris, and logging as soon as possible after drilling and conditioning are completed.

The quality of the logging depth determination depends on several factors. The depth of the wireline-logged measurement is determined from the length of the logging cable played out at the winch on the ship. The seafloor is identified on the NGR log by the abrupt reduction in gamma radiation at the water/sediment boundary (mudline). Discrepancies between drillers depth and wireline log depth occur because of core expansion, incomplete core recovery, incomplete heave compensation, and, for drillers depth only, drill pipe stretch. Discrepancies in log depth between successive runs occur because of incomplete heave compensation, incomplete correction for cable stretch, and cable slip. Tidal changes in sea level also affect depth determination. Wireline tool motion caused by ship heave is minimized by a new hydraulic WHC that adjusts for rig motion during wireline logging operations.

## Wireline heave compensator

Expedition 323 continued evaluation of the new WHC system aboard the *JOIDES Resolution*. The WHC system is designed to compensate for the vertical motion of the ship and maintain the steady motion of the logging tools. It uses vertical acceleration measurements made by a motion reference unit (MRU; located under the rig floor near the ship's center of gravity) to calculate the vertical motion of the ship, and it adjusts the length of the wireline by varying the distance between two sets of pulleys through which the cable passes. Real-time measurements of uphole (surface) and downhole acceleration are made simultaneously by the MRU and by the GPIT tool, respectively. A software package developed by Lamont-Doherty Earth Observatory (LDEO) allows these data to be analyzed and compared in real time, displaying the actual motion of the logging tool string and enabling evaluation of the compensator's efficiency. In addition to its improved design and smaller footprint compared to the previous system, the WHC's placement near the winch unit on the starboard side of the derrick contributes to a significant reduction in the time needed to prepare for logging operations.

## Logging data flow and log depth scales

Data for each wireline logging run were monitored in real time and recorded using the Schlumberger MAXIS 500 system. Initial logging data were refer-

enced to the rig floor (wireline log depth below rig floor [WRF]). After logging was completed, the data were shifted to a seafloor reference (wireline log depth below seafloor [WSF]) based on the step in gamma radiation at the sediment/water interface.

Downhole logging data were also transferred on shore to LDEO for standardized data processing. This processing consisted primarily of depth matching to remove depth offsets between different logging runs, which resulted in a new depth scale, wireline log matched depth below seafloor (WMSF). In addition, during data processing, corrections were made to certain tools and logs, and documentation for the logs (with an assessment of log quality) was prepared. Schlumberger GeoQuest's GeoFrame software package was used for most of the processing. The data were transferred back to the ship within a few days of logging and were made available through the shipboard IODP logging database.

Measurements of properties such as NGR and density were taken both downhole and on cores. These measurements can be correlated with Correlator, which allows the shifting of core depths onto the wireline depth scale (see **"Stratigraphic correlation"**).

### Core-log-seismic integration

Depth–traveltime relationships must be determined at each site to correlate core and logging data acquired at depth with seismic reflection measurements that are a function of sonic traveltime. Although the most direct way to define such a relationship is to acquire a check shot survey or vertical seismic profile, it can also be estimated by constructing synthetic seismograms that are computed from reflection coefficients obtained from contrasts in *P*-wave velocity and density. Synthetic seismograms were calculated from density and $V_P$ logs using the IESX seismic interpretation package (part of the Schlumberger GeoFrame software suite), which allows interactive adjustment of the depth–traveltime relationship until a good match is achieved between features in the synthetic seismogram and the measured seismic data. A calibrated depth–traveltime relationship allows correlation of hole stratigraphy with seismic reflection features (e.g., the assignment of ages to prominent seismic reflectors that can be correlated away from the drill site).

### In situ temperature measurements

In situ temperature measurements were made at each site using the APCT-3 temperature tool. The APCT-3 tool fits directly into the coring shoe of the APC and consists of a battery pack, data logger, and platinum resistance-temperature device calibrated over a temperature range of 0°–30°C. Before it enters the borehole, the tool is stopped at the seafloor for 5 min to thermally equilibrate with bottom water. However, the lowest temperature recorded during the run down is preferred to the average temperature at the seafloor as an estimate of bottom water temperature because this measurement is more repeatable and the bottom water is expected to have the lowest temperature in the profile. After the APC penetrated the sediment, it was held in place for 5–10 min while the APCT-3 instrument recorded the temperature of the cutting shoe every second. When the APC was plunged into the formation there was an instantaneous temperature rise from frictional heating. This heat gradually dissipated into the surrounding sediments as the temperature at the APCT-3 equilibrated toward the temperature of the sediments.

The equilibrium temperature of the sediments was estimated by applying a mathematical heat-conduction model to the temperature decay record (Horai and Von Herzen, 1985). The synthetic thermal decay curve for the APCT-3 tool is a function of the geometry and thermal properties of the probe and the sediments (Bullard, 1954; Horai and Von Herzen, 1985). The equilibrium temperature must be estimated by applying a fitting procedure in the TP-Fit software by Heesemann. However, when the APCT-3 does not achieve a full stroke or ship heave pulls up the APC from full penetration, the temperature equilibration curve is disturbed and temperature determination is more difficult. The nominal accuracy of the APCT-3 temperature measurement is ±0.1°C.

APCT-3 temperature data were combined with measurements of thermal conductivity (see **"Physical properties"**) obtained from core samples to obtain heat flow values. Heat flow was calculated according to the Bullard method to be consistent with ODP Leg 199 analyses and the synthesis of ODP heat flow data by Pribnow et al. (2000).

## Microbiology

The microbiology objectives of Expedition 323 are (1) to constrain global models of subseafloor biomass by quantifying subseafloor cell abundance in an extremely high productivity region of the ocean and (2) to determine how subseafloor community composition is influenced by extremely high productivity in the overlying ocean. To meet these objectives, our analyses included quantification of total cell abundance and assessment of the diversity and structure of the microbial community by the use of nucleic acid–based techniques and fluorescent in situ hybridization (FISH).

## Core handling and sampling

Cores were sectioned on the catwalk, and the sections were immediately run through the SHMSL. To minimize temperature effects on microbial community composition, all further handling took place in the Cold Laboratory (7°C). All materials, including core cutters, were kept cold so that the samples did not warm. In addition, because core liners are not sterile and the outer surfaces of cores are contaminated during drilling (Smith et al., 2000a, 2000b), subsampling excluded the sediment next to the core liner. In the Cold Laboratory, core sections were cut into multiple whole rounds for interstitial water analyses. Immediately after cutting a whole round, the edge of the remainder section was cleaned with a sterile blade. Samples for prokaryotic cell counts, contamination tests, and nucleic acid analyses were then taken with sterile 5–60 $cm^3$ cut-off syringes.

The above procedures were followed only for cores retrieved from microbiology-dedicated holes. In addition, a limited number of samples were collected from nondedicated holes. These samples were taken directly on the catwalk adjacent to whole rounds collected for interstitial water analyses.

## Prokaryotic cell counts and contamination tests

Cell counts (cells per cubic centimeter) serve as the basis for subseafloor biomass estimates (e.g., Whitman et al., 1998; Parkes et al., 2000; Kallmeyer et al., 2008). Samples for prokaryotic cell counts were taken with sterile 3 $cm^3$ cut-off syringes, placed in 15 mL vials containing 8 mL of 2% formalin, and stored at 4°C for postcruise analyses (Kallmeyer et al., 2008).

Contamination during drilling and handling was evaluated by tests using micrometer-sized fluorescent beads and perfluorocarbon tracer (PFT). These tests have previously shown that core samples can be obtained without introducing prokaryotic cell contamination, which is essential for all microbiological analyses that follow core retrieval (Smith et al., 2000a, 2000b).

A suspension of submicrometer-sized fluorescent microspheres was introduced into the drill fluid in all microbiology-dedicated holes. A plastic bag positioned within the core catcher released a suspension of beads inside the core barrel as it hit the sediment, allowing for the maximum effectiveness of the beads as tracers of potential bacterial contamination. Particle contamination in the samples will be evaluated during postcruise analyses of subsamples taken for total cell counts.

PFT was continuously fed into the seawater drill fluid at a tracer concentration of 1 mg/L seawater drill fluid. The concentration of PFT was measured in all sections used for microbiological studies. For this purpose, 5 $cm^3$ subsamples were routinely taken, as described by Smith et al. (2000b), and placed in headspace vials. PFT was analyzed on a GC equipped with an electron capture detector and an HP-AL/S 15 m × 0.25 mm ID, 5.00 µm film thickness (Agilent P/N 19091P-531) column. Additionally, air samples were occasionally taken to monitor the ambient concentration of PFT in the Cold Laboratory air. The concentration of PFT at the outer periphery of the drill cores was measured to verify delivery of the PFT.

## Diversity and structure of the microbial community

### Microbial molecular analyses

Samples for microbial molecular analyses were collected in 5 and 60 $cm^3$ sterile cut-off syringes, which were frozen at –80°C in Mylar or whirlpack bags.

Molecular analysis of the 16S ribosomal ribonucleic acid (rRNA) will be performed during postcruise investigations. 16S ribosomal deoxyribonucleic acid (rDNA) sequence libraries for prokaryote diversity will be established and compared downhole and between sites. Functional genes will be analyzed through application of specific polymerase chain reaction (PCR) primers. This will enable the characterization of the diversity of specific functional guilds such as sulfate-reducing bacteria.

### Fluorescence in situ hybridization

Samples for FISH analysis were collected in 2 $cm^3$ sterile syringes and transferred to Eppendorf tubes. Sediment was fixed following the protocol by Pernthaler et al. (2001) in buffered paraformaldehyde solution (gram-negative bacteria) or ethanol (Archaea and gram-positive bacteria). Fixed samples were washed several times, and ethanol was added. Samples were then stored at –20°C until processing in onshore laboratories.

# References

Alvarez Zarikian, C.A., 2009. Data report: late Quaternary ostracodes at IODP Site U1314 (North Atlantic Ocean). *In* Channell, J.E.T., Kanamatsu, T., Sato, T., Stein, R., Alvarez Zarikian, C.A., Malone, M.J., and the Expedition 303/306 Scientists, *Proc. IODP,* 303/306: College Station, TX (Integrated Ocean Drilling Program Management International, Inc.). **doi:10.2204/iodp.proc.303306.213.2009**

Alvarez Zarikian, C.A., Stepanova, A.Y., and Grützner, J., 2009. Glacial–interglacial variability in deep sea ostracod assemblage composition at IODP Site U1314 in the subpolar North Atlantic. *Mar. Geol.,* 258(1–4):69–87. **doi:10.1016/j.margeo.2008.11.009**

ASTM International, 1990. Standard method for laboratory determination of water (moisture) content of soil and rock (Standard D2216–90). In *Annual Book of ASTM Standards for Soil and Rock* (Vol. 04.08): Philadelphia (Am. Soc. Testing and Mater.). [revision of D2216-63, D2216-80]

Ayress, M., Neil, H., Passlow, V., and Swanson, K., 1997. Benthonic ostracods and deep watermasses: a qualitative comparison of southwest Pacific, Southern and Atlantic Oceans. *Palaeogeogr., Palaeoclimatol., Palaeoecol.,* 131(3–4):287–302. **doi:10.1016/S0031-0182(97)00007-2**

Barron, J.A., and Gladenkov, A.Y., 1995. Early Miocene to Pleistocene diatom stratigraphy of Leg 145. *In* Rea, D.K., Basov, I.A., Scholl, D.W., and Allan, J.F. (Eds.), *Proc. ODP, Sci. Results,* 145: College Station, TX (Ocean Drilling Program), 3–19. **doi:10.2973/odp.proc.sr.145.101.1995**

Blum, P., 1997. Physical properties handbook: a guide to the shipboard measurement of physical properties of deep-sea cores. *ODP Tech. Note,* 26. **doi:10.2973/odp.tn.26.1997**

Bujak, J.P., 1984. Cenozoic dinoflagellate cysts and acritarchs from the Bering Sea and northern North Pacific, DSDP Leg 19. *Micropaleontology,* 30(2):180–212. **doi:10.2307/1485717**

Bujak, J.P., and Matsuoka, K., 1986a. Late Cenozoic dinoflagellate cyst zonation in the western and northern Pacific. *In* Wrenn, J.H., Duffield, S.L., and Stein, J.A. (Eds.), *Am. Assoc. Stratigr. Palynol. Contrib. Ser.,* 17:7–25.

Bujak, J.P., and Matsuoka, K., 1986b. Taxonomic reallocation of Cenozoic dinoflagellate cysts from Japan and the Bering Sea. *Palynology,* 10:235–241.

Bukry, D., 1973. Coccoliths and silicoflagellates from Deep Sea Drilling Project Leg 19, North Pacific Ocean and Bering Sea. *In* Creager, J.S., Scholl, D.W., et al., *Init. Repts. DSDP,* 19: Washington, DC (U.S. Govt. Printing Office), 857–867. **doi:10.2973/dsdp.proc.19.131.1973**

Bullard, E.C., 1954. The flow of heat through the floor of the Atlantic Ocean. *Proc. R. Soc. London, Ser. A,* 222:408–429.

Cline, J.D., 1969. Spectrophotometric determination of hydrogen sulfide in natural waters. *Limnol. Oceanogr.,* 14:454–458.

Commission Internationale d'Eclairage (CIE), 1986. *CIE Recommendations on Colorimetry,* 2nd ed. (CIE 15.2-1986): Vienna (CIE Central Bureau).

Corrège, T., 1993. The relationship between water masses and benthic ostracod assemblages in the western Coral Sea, Southwest Pacific. *Palaeogeogr., Palaeoclimatol., Palaeoecol.,* 105(3–4):245–266. **doi:10.1016/0031-0182(93)90086-X**

Cronin, T.M., Boomer, I., Dwyer, G.S., and Rodriguez-Lázaro, J., 2002. Ostracoda and paleoceanography. *In* Holmes, J.A., and Chivas, A.R. (Eds.), *The Ostracoda: Applications in Quaternary Research:* Washington, DC (Am. Geophys. Union), 99–119.

De Schepper, S., and Head, M.J., 2008a. Age calibration of dinoflagellate cyst and acritarch events in the Plio-Pleistocene of the eastern North Atlantic (DSDP Hole 610A). *Stratigraphy,* 5(2):137–161.

De Schepper, S., and Head, M.J., 2008b. New dinoflagellate cyst and acritarch taxa from the Pliocene and Pleistocene of the eastern North Atlantic (DSDP Site 610). *J. Syst. Palaeontol.,* 6(1):101–117. **doi:10.1017/S1477201907002167**

de Vernal, A., Londeix, L., Mudie, P.J., Harland, R., Morzadec-Kerfourn, M.T., Turon, J.-L., and Wrenn, J.H., 1992. Quaternary organic-walled dinoflagellate cysts of the North Atlantic Ocean and adjacent seas: ecostratigraphy and biostratigraphy. *In* Head, M.J., and Wrenn, J.H. (Eds.), *Neogene and Quaternary Dinoflagellate Cysts and Arcritarchs:* Salt Lake City (Publisher's Press), 289–328.

de Vernal, A., and Mudie, P.J., 1989. Pliocene and Pleistocene palynostratigraphy at ODP Sites 646 and 647, eastern and southern Labrador Sea. *In* Srivastava, S.P., Arthur, M.A., Clement, B., et al., *Proc. ODP, Sci. Results,* 105: College Station, TX (Ocean Drilling Program), 401–422. **doi:10.2973/odp.proc.sr.105.134.1989**

de Vernal, A., and Mudie, P.J., 1992. Pliocene and Quaternary dinoflagellate cyst stratigraphy in Labrador Sea: paleoecological implications. *In* Head, M.J., and Wrenn, J.H. (Eds.), *Neogene and Quaternary Dinoflagellate Cysts and Acritarchs:* Salt Lake City (Publisher's Press), 329–346.

Didié, C., and Bauch, H.A., 2001. Erratum to "Species composition and glacial–interglacial variations in the ostracode fauna of the northeast Atlantic during the past 200,000 years" [Marine Micropaleontology, 40 (2000) 105–129]. *Mar. Micropaleontol.,* 40(1–2):103–108. **doi:10.1016/S0377-8398(00)00051-7**

Dingle, R.V., and Lord, A.R., 1990. Benthic ostracods and deep water-masses in the Atlantic Ocean. *Palaeogeogr., Palaeoclimatol., Palaeoecol.,* 80(3–4):213–235. **doi:10.1016/0031-0182(90)90133-R**

Ellis, D.V., and Singer, J.M., 2007. *Well Logging for Earth Scientists, Second Edition:* Dordrecht, The Netherlands (Springer).

Evans, H.B., 1965. GRAPE—a device for continuous determination of material density and porosity. *Trans. SPWLA Annu. Logging Symp.:* 6(2):B1–B25.

Fisher, R.V., and Schmincke, H.-U., 1984. *Pyroclastic Rocks:* New York (Springer-Verlag).

Gieskes, J.M., Gamo, T., and Brumsack, H., 1991. Chemical methods for interstitial water analysis aboard *JOIDES Resolution. ODP Tech. Note,* 15. **doi:10.2973/odp.tn.15.1991**

Gieskes, J.M., and Rogers, W.C., 1973. Alkalinity determination in interstitial waters of marine sediments. *J. Sediment. Petrol.,* 43:272–277.

Goldberg, D., 1997. The role of downhole measurements in marine geology and geophysics. *Rev. Geophys.,* 35(3):315–342. **doi:10.1029/97RG00221**

Hagelberg, T.K., Pisias, N.G., Shackleton, N.J., Mix, A.C., and Harris, S., 1995. Refinement of a high-resolution,

continuous sedimentary section for studying equatorial Pacific Ocean paleoceanography, Leg 138. *In* Pisias, N.G., Mayer, L.A., Janecek, T.R., Palmer-Julson, A., and van Andel, T.H. (Eds.), *Proc. ODP, Sci Results,* 138: College Station, TX (Ocean Drilling Program), 31–46. **doi:10.2973/odp.proc.sr.138.103.1995**

Hagelberg, T., Shackleton, N., Pisias, N., and Shipboard Scientific Party, 1992. Development of composite depth sections for Sites 844 through 854. *In* Mayer, L., Pisias, N., Janecek, T., et al., *Proc. ODP, Init. Repts.,* 138: College Station, TX (Ocean Drilling Program), 79–85. **doi:10.2973/odp.proc.ir.138.105.1992**

Harland, R., 1979. Dinoflagellate biostratigraphy of Neogene and Quaternary sediments at Holes 400/400A in the Bay of Biscay (Deep Sea Drilling Project Leg 48). *In* Montadert, L., Roberts, D.G., et al., *Init. Repts. DSDP,* 48: Washington, DC (U.S. Govt. Printing Office), 531–545. **doi:10.2973/dsdp.proc.48.122.1979**

Harms, J.C., and Choquette, P.W., 1965. Geologic evaluation of a gamma-ray porosity device. *Trans. SPWLA Annu. Logging Symp.:* 6:C1–C37.

Harris, S., Hagelberg, T., Mix, A., Pisias, N.G., and Shackleton, N.J., 1995. Sediment depths determined by comparisons of GRAPE and logging density data during Leg 138. *In* Pisias, N.G., Mayer, L.A., Janecek, T.R., Palmer-Julson, A., and van Andel, T.H. (Eds.), *Proc. ODP, Sci. Results,* 138: College Station, TX (Ocean Drilling Program), 47–57. **doi:10.2973/odp.proc.sr.138.104.1995**

Hays, J.D., 1970. Stratigraphy and evolutionary trends of radiolaria in North Pacific deep sea sediments. *In* Hays, J.D. (Ed.), *Geological Investigations of the North Pacific.* Mem.—Geol. Soc. Am., 126:185–218.

Head, M.J., and Norris, G., 2003. New species of dinoflagellate cysts and other palynomorphs from the latest Miocene and Pliocene of DSDP Hole 603C, western North Atlantic. *J. Paleontol.,* 77(1):1–15. **doi:10.1666/0022-3360(2003)077<0001:NSODCA>2.0.CO;2**

Head, M.J., Norris, G., and Mudie, P.J., 1989. Palynology and dinocyst stratigraphy of the upper Miocene and lowermost Pliocene, ODP Leg 105, Site 646, Labrador Sea. *In* Srivastava, S.P., Arthur, M.A., Clement, B., et al., *Proc. ODP, Sci. Results,* 105: College Station, TX (Ocean Drilling Program), 423–451. **doi:10.2973/odp.proc.sr.105.135.1989**

Head, M.J., Riding, J.B., Eidvin, T., and Chadwick, R.A., 2004. Palynology and foraminiferal biostratigraphy of (upper Pliocene) Nordland Group mudstones at Sleipner, northern North Sea. *Mar. Petrol. Geol.,* 21(3):277–297. **doi:10.1016/j.marpetgeo.2003.12.002**

Hine, N., and Weaver, P.P.E., 1998. Quaternary. *In* Bown P.R. (Ed), *Calcareous Nannofossil Biostratigraphy:* Dordrecht (Kluwer Academic Publishers), 266–283.

Horai, K., and Von Herzen, R.P., 1985. Measurement of heat flow on Leg 86 of the Deep Sea Drilling Project. *In* Heath, G.R., Burckle, L.H., et al., *Init. Repts. DSDP,* 86: Washington, DC (U.S. Govt. Printing Office), 759–777. **doi:10.2973/dsdp.proc.86.135.1985**

Jorissen, F.J., de Stigter, H.C., and Widmark, J.G.V., 1995. A conceptual model explaining benthic foraminiferal microhabitats. *Mar. Micropaleontol.,* 26(1–4):3–15. **doi:10.1016/0377-8398(95)00047-X**

Joy, J.A., and Clark, D.L., 1977. The distribution, ecology and systematics of the benthic Ostracoda of the central Arctic Ocean. *Micropaleontology,* 23(2):129–154. **doi:10.2307/1485329**

Kallmeyer, J., Smith, D.C., Spivack, A.J., and D'Hondt, S., 2008. New cell extraction procedure applied to deep subsurface sediments. *Limnol. Oceanogr.: Methods,* 6:236–245.

Kamikuri, S., Nishi, H., and Motoyama, I., 2007. Effects of late Neogene climatic cooling on North Pacific radiolarian assemblages and oceanographic conditions. *Palaeogeogr., Palaeoclimatol., Palaeoecol.,* 249(3–4):370–392. **doi:10.1016/j.palaeo.2007.02.008**

Kamikuri, S., Nishi, H., Motoyama, I., and Saito, S., 2004. Middle Miocene to Pleistocene radiolarian biostratigraphy in the Northwest Pacific Ocean, ODP Leg 186. *Isl. Arc,* 13(1):191–226. **doi:10.1111/j.1440-1738.2003.00421.x**

Kennett, J.P., and Srinivasan, M.S., 1983. *Neogene Planktonic Foraminifera: A Phylogenetic Atlas:* Stroudsburg, PA (Hutchinson Ross).

Kobayashi, H., 1988. Neogene silicoflagellate biostratigraphy of the Japan Sea Coastal region, with reference to DSDP Hole 438A. *Sci Rep. Tohoku Univ., Ser. 2,* 59:1–98.

Kristiansen, J.I., 1982. The transient cylindrical probe method for determination of thermal parameters of earth materials [Ph.D. dissert.]. Åarhus Univ., Åarhus, Denmark.

Laskar, J., Robutel, P., Joutel, F., Gastineau, M., Correia, A.C.M., and Levrard, B., 2004. A long-term numerical solution for the insolation quantities of the Earth. *Astron. Astrophys.,* 428(1):261–285. **doi:10.1051/0004-6361:20041335**

Ling, H.Y., 1973. Silicoflagellates and ebridians from Leg 19. *In* Creager, J.S., Scholl, D.W., et al., *Init. Repts.* DSDP, 19: Washington (U.S. Govt. Printing Office), 751–775. **doi:10.2973/dsdp.proc.19.127.1973**

Ling, H.Y., 1977. Late Cenozoic silicoflagellates and ebridians from the eastern North Pacific region. *Proc. Int. Congr. Pac. Neogene Stratigr.,* 1:205–233.

Ling, H.Y., 1992. Late Neogene silicoflagellates and ebridians from Leg 128, Sea of Japan. *In* Pisciotto, K.A., Ingle, J.C., Jr., von Breymann, M.T., and Barron, J., et al. (Eds.), *Proc. ODP, Sci. Results,* 127/128, Pt. 1: College Station, TX (Ocean Drilling Program), 237–248. **doi:10.2973/odp.proc.sr.127128-1.126.1992**

Lisiecki, L.E., and Raymo, M.E., 2005. A Pliocene–Pleistocene stack of 57 globally distributed benthic $\delta^{18}O$ records. *Paleoceanography,* 20(1):PA1003. **doi:10.1029/2004PA001071**

Loeblich, A.R., and Tappan, H., 1988. *Foraminiferal Genera and Their Classification* (Vol. 2): New York (Van Nostrand Reinhold Co.).

Lourens, L.J., Hilgen, F.J., Shackleton, N.J., Laskar, J., and Wilson, D., 2004. The Neogene period. *In* Gradstein, F.M., Ogg, J.G., and Smith, A.G. (Eds.), *A Geological Time Scale 2004*. Cambridge (Cambridge Univ. Press), 409–440.

Louwye, S., Head, M.J., and De Schepper, S., 2004. Dinoflagellate cyst stratigraphy and palaeoecology of the Pliocene in northern Belgium, southern North Sea Basin. *Geol. Mag.,* 141(3):353–378. **doi:10.1017/S0016756804009136**

Lovell, M.A., Harvey, P.K., Brewer, T.S., Williams, C., Jackson, P.D., and Williamson, G., 1998. Application of FMS images in the Ocean Drilling Program: an overview. *In* Cramp, A., MacLeod, C.J., Lee, S.V., and Jones, E.J.W. (Eds.), *Geological Evolution of Ocean Basins: Results from the Ocean Drilling Program.* Geol. Soc. Spec. Publ., 131(1):287–303. **doi:10.1144/GSL.SP.1998.131.01.18**

Manheim, F.T., and Sayles, F.L., 1974. Composition and origin of interstitial waters of marine sediments, based on deep sea drill cores. *In* Goldberg, E.D. (Ed.), *The Sea* (Vol. 5): *Marine Chemistry: The Sedimentary Cycle:* New York (Wiley), 527–568.

Martini, E., 1971. Standard Tertiary and Quaternary calcareous nannoplankton zonation. *In* Farinacci, A. (Ed.), *Proc. 2nd Int. Conf. Planktonic Microfossils Roma:* Rome (Ed. Tecnosci.), 2:739–785.

Matsuoka, K., 1983. Late Cenozoic dinoflagellates and acritarchs in the Niigata District, Central Japan. *Palaeontographica, Abt. B,* 187:89–154.

McDuff, R.E., and Ellis, R.A., 1979. Determining diffusion coefficients in marine sediments: a laboratory study of the validity of resistivity techniques. *Am. J. Sci.,* 279:666–675.

Mix, A.C., Tiedemann, R., Blum, P., et al., 2003. *Proc. ODP, Init. Repts.,* 202: College Station, TX (Ocean Drilling Program). **doi:10.2973/odp.proc.ir.202.2003**

Moran, K., 1997. Elastic property corrections applied to Leg 154 sediment, Ceara Rise. *In* Shackleton, N.J., Curry, W.B., Richter, C., and Bralower, T.J. (Eds.), *Proc. ODP, Sci. Results,* 154: College Station, TX (Ocean Drilling Program), 151–155. **doi:10.2973/odp.proc.sr.154.132.1997**

Morley, J.J., and Nigrini, C., 1995. Miocene to Pleistocene radiolarian biostratigraphy of North Pacific Sites 881, 884, 885, 886, and 887. *In* Rea, D.K., Basov, I.A., Scholl, D.W., and Allan, J.F. (Eds.), *Proc. ODP, Sci. Results,* 145: College Station, TX (Ocean Drilling Program), 55–91. **doi:10.2973/odp.proc.sr.145.107.1995**

Motoyama, I., 1996. Late Neogene radiolarian biostratigraphy in the subarctic Northwest Pacific. *Micropaleontology,* 42(3):221–262. **doi:10.2307/1485874**

Mudie, P.J., 1987. Palynology and dinoflagellate biostratigraphy of Deep Sea Drilling Project Leg 94, Sites 607 and 611, North Atlantic Ocean. *In* Ruddiman, W.F., Kidd, R.B., Thomas, E., et al., *Init. Repts. DSDP,* 94: Washington, DC (U.S. Govt. Printing Office), 785–812. **doi:10.2973/dsdp.proc.94.118.1987**

Mudie, P.J., 1989. Palynology and dinocyst biostratigraphy of the late Miocene to Pleistocene, Norwegian Sea: ODP Leg 104, Sites 642 to 644. *In* Eldholm, O., Thiede, J., Taylor, E., et al., *Proc. ODP, Sci. Results,* 104: College Station, TX (Ocean Drilling Program), 587–610. **doi:10.2973/odp.proc.sr.104.174.1989**

Munsell Color Company, Inc., 1994. *Munsell Soil Color Chart* (Revised ed.): Newburgh, MD (Munsell Color).

Murray, R.W., Miller, D.J., and Kryc, K.A., 2000. Analysis of major and trace elements in rocks, sediments, and interstitial waters by inductively coupled plasma–atomic emission spectrometry (ICP-AES). *ODP Tech. Note,* 29. **doi:10.2973/odp.tn.29.2000**

Pälike, H., Frazier, J., and Zachos, J.C., 2006. Extended orbitally forced palaeoclimatic records from the equatorial Atlantic Ceara Rise. *Quat. Sci. Rev.,* 25(23–24):3138–3149. **doi:10.1016/j.quascirev.2006.02.011**

Pälike, H., Moore, T., Backman, J., Raffi, I., Lanci, L., Parés, J.M., and Janecek, T., 2005. Integrated stratigraphic correlation and improved composite depth scales for ODP Sites 1218 and 1219. *In* Wilson, P.A., Lyle, M., and Firth, J.V. (Eds.), *Proc. ODP, Sci. Results,* 199: College Station, TX (Ocean Drilling Program), 1–41. **doi:10.2973/odp.proc.sr.199.213.2005**

Parkes, R.J., Cragg, B.A., and Wellsbury, P., 2000. Recent studies on bacterial populations and processes in subseafloor sediments: a review. *Hydrogeol. J.,* 8(1):11–28. **doi:10.1007/PL00010971**

Pernthaler, J., Glöckner, F.O., Schönhuber, W., and Amann, R., 2001. Fluorescence in situ hybridization with rRNA-targeted oligonucleotide probes. *Meth. Enzymol.,* 30:207–226.

Piasecki, S., 2003. Neogene dinoflagellate cysts from Davis Strait, offshore West Greenland. *Mar. Petrol. Geol.,* 20(9):1075–1088. **doi:10.1016/S0264-8172(02)00089-2**

Powell, A.J., 1988. A preliminary investigation in the Neogene dinoflagellate cyst biostratigraphy of the British Southwestern approaches. *Bull. Cent. Rech. Explor.-Prod. Elf-Aquitaine,* 12:277–311.

Powell, A.J. (Ed.), 1992. *A Stratigraphic Index of Dinoflagellate Cysts:* London (Chapman and Hall).

Powers, M.C., 1953. A new roundness scale for sedimentary particles. *J. Sediment. Petrol.,* 23:117–119.

Pribnow, D.F.C., Kinoshita, M., and Stein, C.A., 2000. *Thermal Data Collection and Heat Flow Recalculations for ODP Legs 101–180:* Hanover, Germany (Inst. Joint Geosci. Res., Inst. Geowiss. Gemeinschaftsauf. [GGA]). **http://www-odp.tamu.edu/publications/heatflow/ODPReprt.pdf**

Radi, T., de Vernal, A., and Peyron, O., 2001. Relationships between dinoflagellate cyst assemblages in surface sediment and hydrographic conditions in the Bering and Chukchi seas. *J. Quat. Sci.,* 16(7):667–680. **doi:10.1002/jqs.652**

Raffi, I., and Flores, J.-A., 1995. Pleistocene through Miocene calcareous nannofossils from eastern equatorial Pacific Ocean (Leg 138). *In* Pisias, N.G., Mayer, L.A., Janecek, T.R., Palmer-Julson, A., and van Andel, T.H. (Eds.), *Proc. ODP, Sci. Results,* 138: College Station, TX (Ocean Drilling Program), 233–286. **doi:10.2973/odp.proc.sr.138.112.1995**

Richter, C., Acton, G., Endris, C., and Radsted, M., 2007. Handbook for shipboard paleomagnetists. *ODP Tech. Note,* 34. **doi:10.2973/odp.tn.34.2007**

Rider, M.H., 1996. *The Geological Interpretation of Well Logs* (2nd ed.): Caithness (Whittles Publ.).

Rothwell, R.G., 1989. *Minerals and Mineraloids in Marine Sediments: An Optical Identification Guide:* London (Elsevier).

Ruddiman, W.F., Cameron, D., and Clement, B.M., 1987. Sediment disturbance and correlation of offset holes drilled with the hydraulic piston corer: Leg 94. *In* Ruddiman, W.F., Kidd, R.B., Thomas, E., et al., *Init. Repts. DSDP,* 94: Washington, DC (U.S. Govt. Printing Office), 615–634. **doi:10.2973/dsdp.proc.94.111.1987**

Sáez, A.G., Probert, I., Geisen, M., Quinn, P., Young, J.R., and Medlin, L.K., 2003. Pseudo-cryptic speciation in coccolithophores. *Proc. Natl. Acad. Sci.,* 100(12):7163–7168. **doi:10.1073/pnas.1132069100**

Salvador, A. (Ed.), 1994. *International Stratigraphic Guide,* 2nd edition: Boulder (IUGS, Geol. Soc. Am.).

Sato, T., and Kameo, K., 1996. Pliocene to Quaternary calcareous nannofossil biostratigraphy of the Arctic Ocean, with reference to late Pliocene glaciation. *In* Thiede, J., Myhre, A.M., Firth, J.V., Johnson, G.L., and Ruddiman, W.F. (Eds.), *Proc. ODP, Sci. Results,* 151: College Station, TX (Ocean Drilling Program), 39–59. **doi:10.2973/odp.proc.sr.151.112.1996**

Sato, T., Saito, T., Yuguchi, S., Nakagawa, H., Kameo, K., and Takayama, T., 2002. Late Pliocene calcareous nannofossil paleobiogeography of the Pacific Ocean: evidence for glaciation at 2.75 Ma. *Rev. Mex. Cienc. Geol.,* 19(3):175–189.

Sato, T., and Takayama, T., 1992. A stratigraphically significant new species, *Reticulofenestra asanoi* (calcareous nannofossil). *In* Ishizaki, K., and Saito, T. (Eds.), *Centenary of Japanese Micropaleontology:* Tokyo (Terra Sci. Publ.), 457–460. **http://www.terrapub.co.jp/e-library/cjm/pdf/0457.pdf**

Scherer, R.P., and Koç, N., 1996. Late Paleogene diatom biostratigraphy and paleoenvironments of the northern Norwegian-Greenland Sea. *In* Thiede, J., Myhre, A.M., Firth, J.V., Johnson, G.L., and Ruddiman, W.F. (Eds.), *Proc. ODP, Sci. Results,* 151: College Station, TX (Ocean Drilling Program), 75–99. **doi:10.2973/odp.proc.sr.151.155.1996**

Schlumberger, 1989. *Log Interpretation Principles/Applications:* Houston (Schlumberger Educ. Services), SMP–7017.

Schlumberger, 1994. *IPL Integrated Porosity Lithology:* Houston (Schlumberger Wireline and Testing), SMP-9270.

Seeberg-Elverfeldt, J., Schlüter, M., Feseker, T., and Kölling, M., 2005. Rhizone sampling of porewaters near the sediment-water interface of aquatic systems. *Limnol. Oceanogr.: Methods,* 3:361–371.

Serra, O., 1984. *Fundamentals of Well-Log Interpretation* (Vol. 1): *The Acquisition of Logging Data:* Dev. Pet. Sci., 15A: Amsterdam (Elsevier).

Serra, O., 1986. *Fundamentals of Well-Log Interpretation* (Vol. 2): *The Interpretation of Logging Data.* Dev. Pet. Sci., 15B: Amsterdam (Elsevier).

Serra, O., 1989. *Formation MicroScanner Image Interpretation:* Houston (Schlumberger Educ. Services), SMP-7028.

Shackleton, N.J., Hall, M.A., Raffi, I., Tauxe, L., and Zachos, J., 2000. Astronomical calibration age for the Oligocene–Miocene boundary. *Geology,* 28(5):447–450. **doi:10.1130/0091-7613(2000)28<447:ACAFTO>2.0.CO;2**

Shepard, F.P., 1954. Nomenclature based on sand-silt-clay ratios. *J. Sediment. Petrol.,* 24(3):151–158.

Shilov, V.V., 1995. Miocene–Pliocene radiolarians from Leg 145, North Pacific. *In* Rea, D.K., Basov, I.A., Scholl, D.W., and Allan, J.F. (Eds.), *Proc. ODP, Sci. Results,* 145: College Station, TX (Ocean Drilling Program), 93–116. **doi:10.2973/odp.proc.sr.145.111.1995**

Smith, D.C., Spivack, A.J., Fisk, M.R., Haveman, S.A., and Staudigel, H., 2000a. Tracer-based estimates of drilling-induced microbial contamination of deep sea crust. *Geomicrobiol. J.,* 17(3):207–219. **doi:10.1080/01490450050121170**

Smith, D.C., Spivack, A.J., Fisk, M.R., Haveman, S.A., Staudigel, H., and the Leg 185 Shipboard Scientific Party, 2000b. Methods for quantifying potential microbial contamination during deep ocean coring. *ODP Tech. Note,* 28. **doi:10.2973/odp.tn.28.2000**

Solórzano, L., 1969. Determination of ammonia in natural waters by phenolhypochlorite method. *Limnol. Oceanogr.,* 14:799–801.

Spezzaferri, S., 1998. Planktonic foraminifer biostratigraphy and paleoenvironmental implications of Leg 152 sites (East Greenland margin). *In* Saunders, A.D., Larsen, H.C., and Wise, S.W., Jr. (Eds.), *Proc. ODP, Sci. Results,* 152: College Station, TX (Ocean Drilling Program), 161–189. **doi:10.2973/odp.proc.sr.152.220.1998**

Stepanova, A.Y., 2006. Late Pleistocene–Holocene and recent Ostracoda of the Laptev Sea and their importance for paleoenvironmental reconstructions. *Paleontol. J.,* 40(S2):91–204. **doi:10.1134/S0031030106080016**

Stepanova, A., Taldenkova, E., and Bauch, H.A., 2004. Ostracod species of the genus *Cytheropteron* from the Pleistocene, Holocene and recent sediments of the Laptev Sea (Arctic Siberia). *Rev. Esp. Micropaleontol.,* 36(1):83–108.

Streckeisen, A., 1974. Classification and nomenclature of plutonic rocks recommendations of the IUGS subcommission on the systematics of igneous rocks. *Geol. Rundsch.,* 63(2):773–786. **doi:10.1007/BF01820841**

Van der Zwaan, G.J., Duijnstee, I.A.P., den Dulk, M., Ernst, S.R., Jannink, N.T., and Kouwenhoven, T.J., 1999. Benthic foraminifers: proxies or problems?: a review of paleoecological problems. *Earth-Sci. Rev.,* 46(1–4):213–236. **doi:10.1016/S0012-8252(99)00011-2**

Von Herzen, R.P., and Maxwell, A.E., 1959. The measurement of thermal conductivity of deep-sea sediments by a needle-probe method. *J. Geophys. Res.,* 64(10):1557–1563. **doi:10.1029/JZ064i010p01557**

Weaver, P.P.E., and Clement, B.M., 1987. Magnetobiostratigraphy of planktonic foraminiferal datums: Deep Sea Drilling Project Leg 94, North Atlantic. *In* Ruddiman, W.F., Kidd, R.B., Thomas, E., et al., *Init. Repts. DSDP,* 94: Washington (U.S. Govt. Printing Office), 815–829. **doi:10.2973/dsdp.proc.94.120.1987**

Whatley, R., and Coles, G., 1987. The late Miocene to Quaternary Ostracoda of Leg 94, Deep Sea Drilling Project. *Rev. Esp. Micropaleontol.,* 19:33–97.

Whatley, R., Eynon, M., and Moguilevsky, A., 1998. The depth distribution of Ostracoda from the Greenland Sea. *J. Micropalaeontol.,* 17:15–32.

Whitman, W.B., Coleman, D.C., and Wiebe, W.J., 1998. Prokaryotes: the unseen majority. *Proc. Natl. Acad. Sci. U. S. A.,* 95(12):6578–6583. **doi:10.1073/pnas.95.12.6578**

Williams, G.L., and Bujak, J.P., 1985. Mesozoic and Cenozoic dinoflagellates. *In* Bolli, H.M., Saunders, J.B., and Perch-Nielsen, K. (Eds.), *Plankton Stratigraphy:* Cambridge (Cambridge Univ. Press), 847–964.

Williams, G.L., Lentin, J.K., and Fensome, R.A., 1998. *The Lentin and Williams Index of Fossil Dinoflagellate Cysts* (1998 ed.). Am. Assoc. Stratigr. Palynol., Contrib. Ser., Vol. 34.

Yasuhara, M., Okahashi, H., and Cronin, T.M., 2009. Taxonomy of Quaternary deep-sea ostracods from the western North Atlantic Ocean. *Palaeontology,* 52(4):879–931. **doi:10.1111/j.1475-4983.2009.00888.x**

Yanagisawa, Y., and Akiba, F., 1990. Taxonomy and phylogeny of the three marine diatom genera, *Crucidenticula, Denticulopsis* and *Neodenticula*. *Bull. Geol. Surv. Jpn.,* 41:197–301.

Yanagisawa, Y., and Akiba, F., 1998. Refined Neogene diatom biostratigraphy for the northwest Pacific around Japan, with an introduction of code numbers for selected diatom biohorizons. *J. Geol. Soc. Jpn.,* 104:395–414.

Young, J.R., 1998. Neogene. *In* Bown, P.R. (Ed.), *Calcareous Nannofossil Biostratigraphy:* Dordrecht, The Netherlands (Kluwer Academic Publ.), 225–265.

**Publication:** 15 March 2011
**MS 323-102**

**Figure F1**. Sediment smear slide worksheet.

**IODP Expedition 323**
**SEDIMENT SMEAR SLIDE WORKSHEET**

| Leg | Site | Hole | Core | Type | Sec | Interval (cm) Top | Interval (cm) Bottom |
|---|---|---|---|---|---|---|---|
| | | | | | | | |

| Sediment/Rock Name | | Observer | |
|---|---|---|---|

Comments:

| Siliciclastic percent texture | | |
|---|---|---|
| Sand | Silt | Clay |
| | | |

| Percent | Component |
|---|---|
| **SILICICLASTIC GRAINS/MINERALS** | |
| | Framework minerals |
| | Quartz |
| | Feldspar |
| | K-feldspar (Orthoclase, Microcline...) |
| | Plagioclase |
| | Rock fragments |
| | |
| | Accessory/trace minerals |
| | Micas |
| | Biotite |
| | Muscovite |
| | Clay minerals |
| | Chlorite |
| | Glauconite |
| | Chert |
| | Zircon |
| | Ferromagnesium minerals |
| | |
| | |
| | Authigenic minerals |
| | Barite |
| | Phosphorite/Apatite |
| | Zeolite |
| | |
| | Opaque minerals |
| | Pyrite |
| | Magnetite |
| | Fe-oxide |
| | |
| | Carbonates |
| | Calcite |
| | Dolomite |
| | |
| **VOLCANICLASTIC GRAINS** | |
| | Crystal grain |
| | |
| | |
| | Vitric grain |
| | Lithic grain |

| Percent | Component |
|---|---|
| **BIOGENIC GRAINS** | |
| | Calcareous |
| | Foraminifers |
| | Planktonic foraminifers |
| | Benthic foraminifers |
| | Nannofossils |
| | Coccoliths |
| | Discoasters |
| | Pteropods |
| | |
| | |
| | Siliceous |
| | Radiolarians |
| | Spumellaria |
| | Nassellaria |
| | Diatoms |
| | Centric |
| | Pennate |
| | *Chaetoceros* resting spores |
| | Silicoflagellates |
| | Sponge spicules |
| | Dinoflagellates |
| | |
| | |
| | Others |
| | Pollen |
| | Organic debris |
| | Plant debris |
| | Ebridians |
| | Echinoderm |
| | Fish remains (teeth, bones, scales) |
| | Bryozoans |
| | Bivalves |
| | Others |
| | |
| | |
| | |
| | |
| | |
| | |

**Figure F2.** Thin section worksheet.

**IODP Expedition 323**
**THIN SECTION WORKSHEET**

| Leg | Site | Hole | Core | Type | Sec | Interval (cm) Top | Interval (cm) Bottom |
|---|---|---|---|---|---|---|---|
| | | | | | | | |

| Sediment/Rock Name | | Observer | |
|---|---|---|---|

| Thin section | Coarse fraction | Grain mount | Dominant lithology | Minor lithology | Siliciclastic percent texture Sand | Silt | Clay |
|---|---|---|---|---|---|---|---|
| | | | | | | | |

Comments:

| Percent | Component |
|---|---|
| | **SILICICLASTIC GRAINS/MINERALS** |
| | Framework minerals |
| | Quartz |
| | Feldspar |
| | K-feldspar (Orthoclase, Microcline...) |
| | Plagioclase |
| | Rock fragments |
| | Sedimentary |
| | Igneous Intrusive |
| | Igneous Volcanic |
| | Metamorphic |
| | |
| | |
| | Accessory/trace minerals |
| | Micas |
| | Biotite |
| | Muscovite |
| | Clay minerals |
| | Chlorite |
| | Glauconite |
| | Chert |
| | Zircon |
| | Ferromagnesium minerals |
| | |
| | |
| | Authigenic minerals |
| | Barite |
| | Phosphorite/Apatite |
| | Zeolite |
| | |
| | |
| | Opaque minerals |
| | Pyrite |
| | Magnetite |
| | Fe-oxide |
| | |
| | |
| | Carbonates |
| | Calcite |
| | Dolomite |

| Percent | Component |
|---|---|
| | **VOLCANICLASTIC GRAINS** |
| | Crystal grain |
| | |
| | Vitric grain (glass, pumice) |
| | Lithic grain |
| | |
| | **BIOGENIC GRAINS** |
| | Calcareous |
| | Foraminifers |
| | Planktonic foraminifers |
| | Benthic foraminifers |
| | Nannofossils |
| | Coccoliths |
| | Discoasters |
| | Pteropods |
| | |
| | Siliceous |
| | Radiolarians |
| | Spumellaria |
| | Nassellaria |
| | Diatoms |
| | Centric |
| | Pennate |
| | *Chaetoceros* resting spores |
| | Silicoflagellates |
| | Sponge spicules |
| | Dinoflagellates |
| | |
| | Others |
| | Pollen |
| | Organic debris |
| | Plant debris |
| | Ebridians |
| | Echinoderm |
| | Fish remains (teeth, bones, scales) |
| | Bryozoans |
| | Bivalves |
| | Others |
| | |
| | |

**Figure F3.** Visual core description worksheet for sediments.

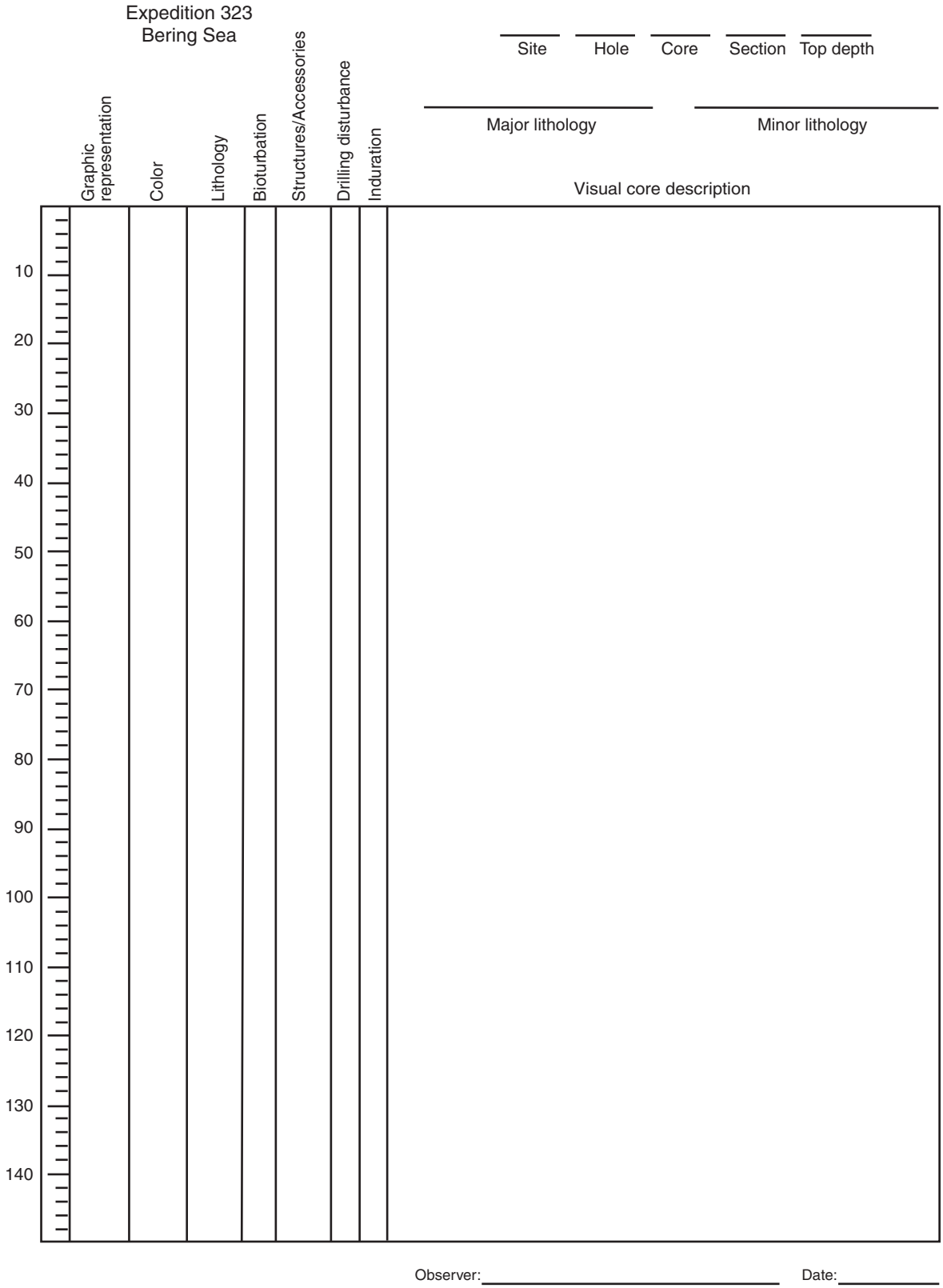

**Figure F4.** Visual core description (VCD) worksheet for hard rocks.

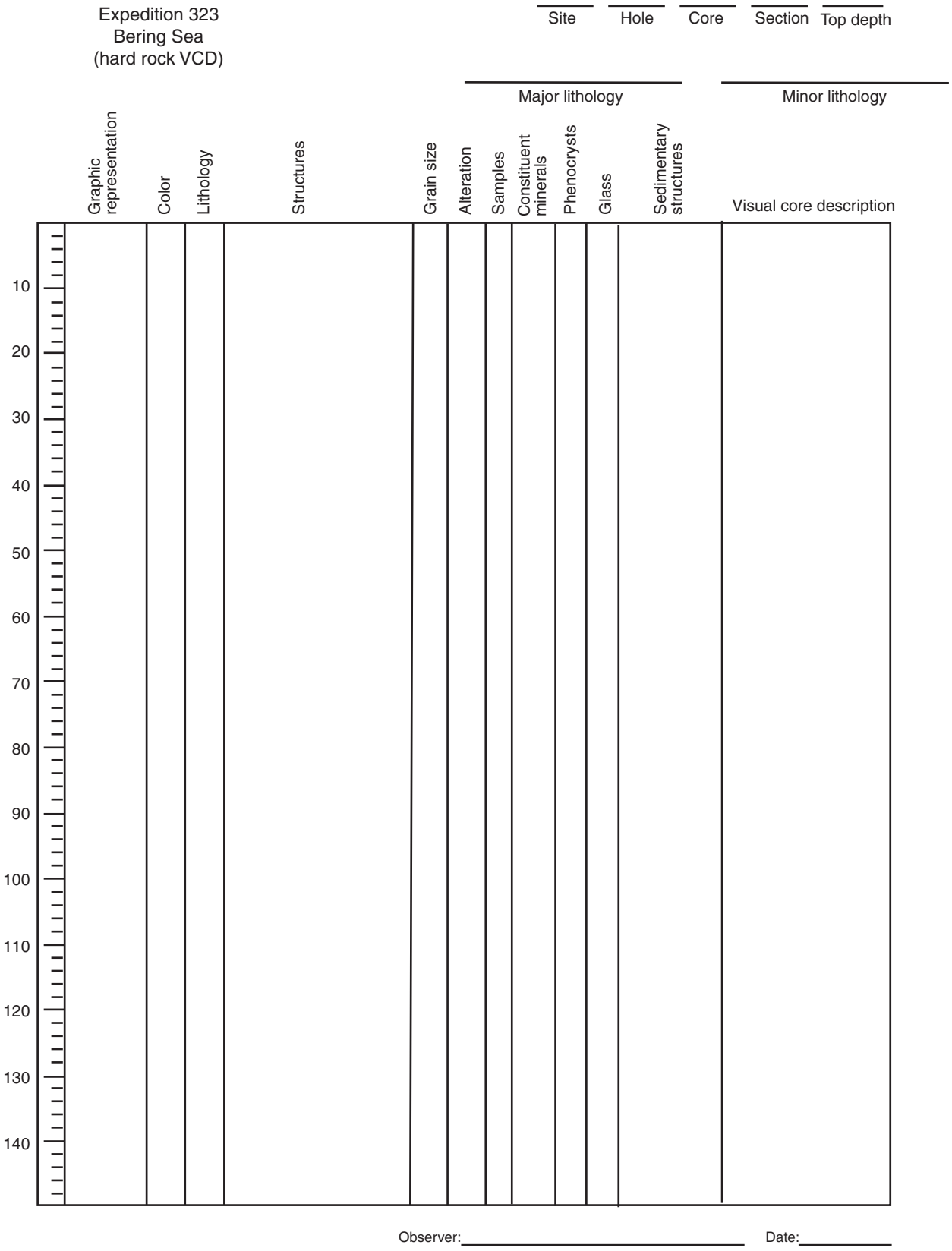

**Figure F5.** Example standard graphical report. GRA = gamma ray attenuation. See Figure F6 for legend.

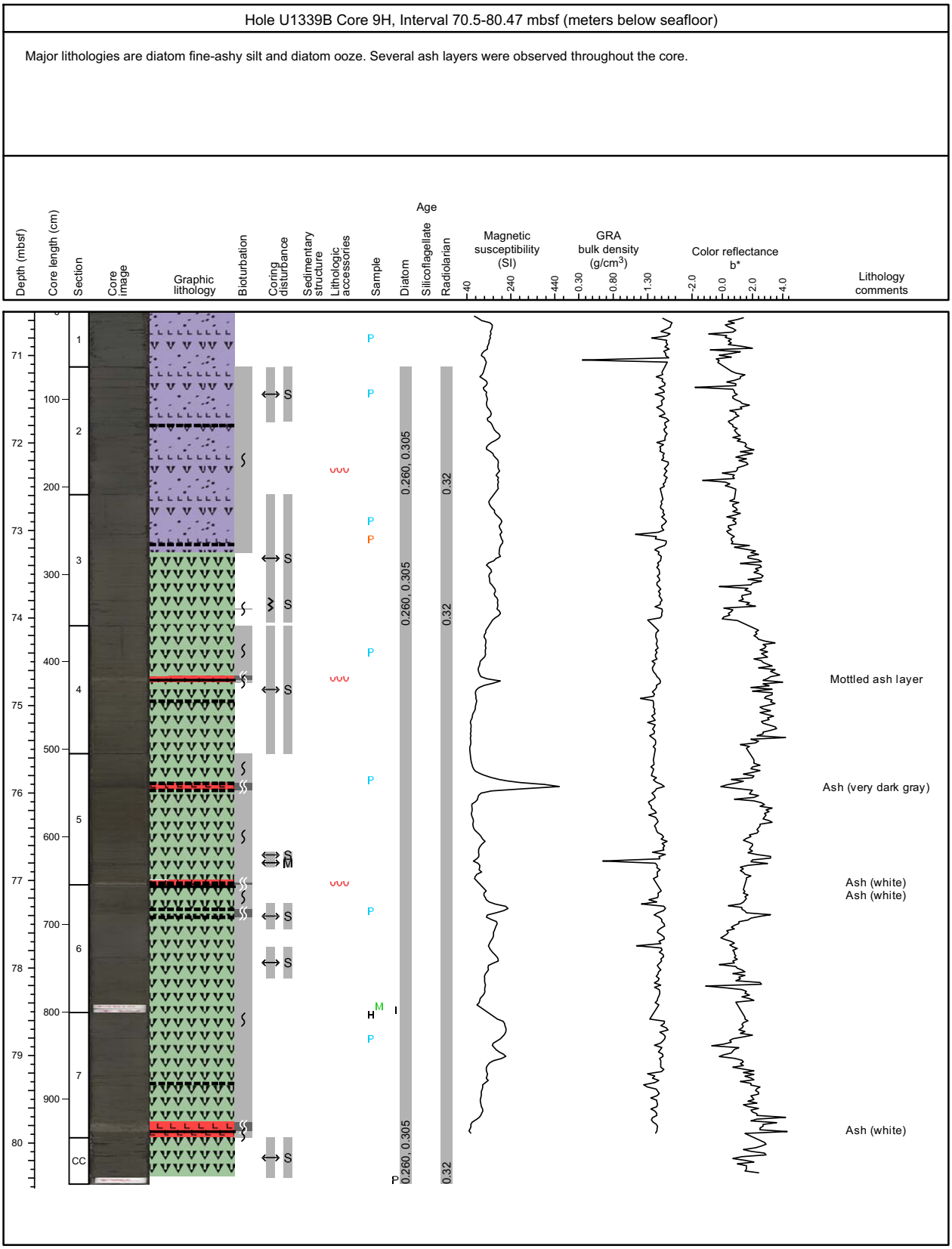

**Figure F6.** Standard graphical report legend.

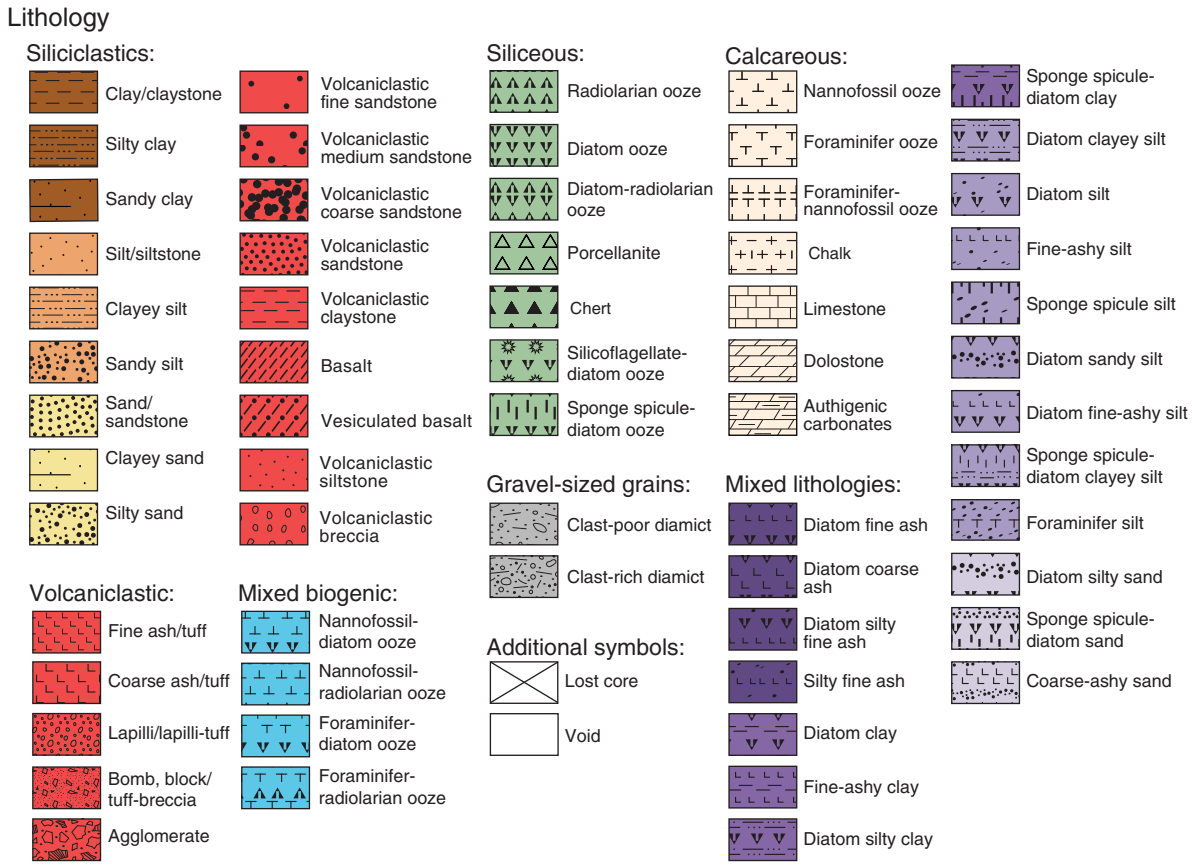

**Figure F7.** Example lithologic summary (top) and legend (bottom). In the lithology column, a black or gray bar that is half the width of the column indicates laminated or bedded sediment, respectively. Soft-sed = soft-sediment, auth = authigenic, calc = calcareous, NGR = natural gamma radiation, GRA = gamma ray attenuation, sed rate = sedimentation rate. Datums and sedimentation rates are from biostratigraphy (black; see "Biostratigraphy") and paleomagnetism (red; see "Paleomagnetism"). The Lisiecki and Raymo (2005) stacked benthic $\delta^{18}O$ curve is plotted at the far right. The locations of Expedition 323 datums are plotted along this curve for reference.

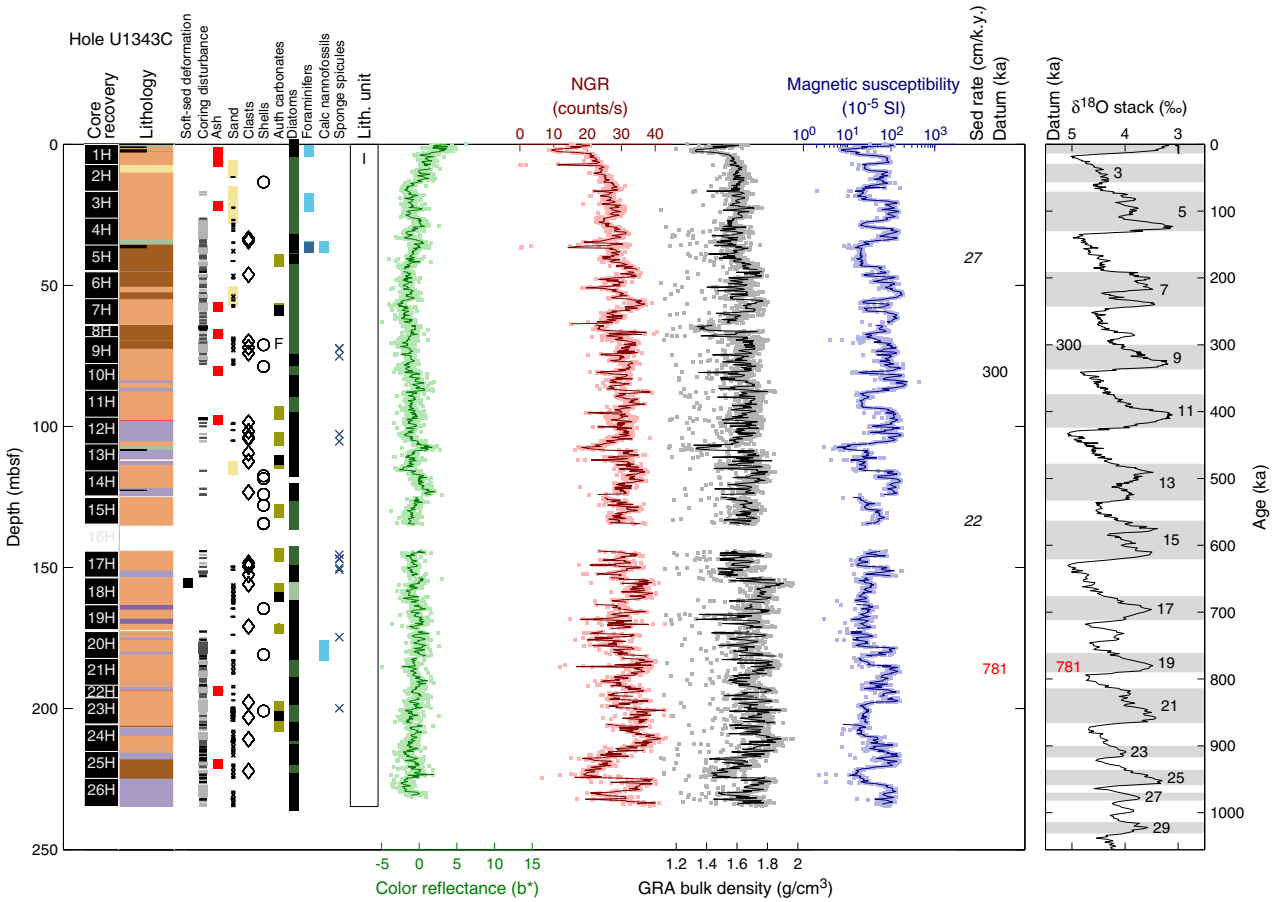


Lithology
- Clay, silty clay, sandy clay
- Silt, clayey silt, sandy silt
- Sand, clayey sand, silty sand
- Ash, basalt, volcaniclastic rocks
- Dolostone
- Diatom ooze
- Mixed calcareous–silicious ooze
- Nannofossil ooze, foraminifer ooze
- Diatom fine ash, silty fine ash
- Diatom clay
- Diatom silt
- Diatom silty sand
- Laminated (<1 cm)
- Thinly bedded (1-10 cm)

Coring disturbance
- Slight
- Moderate
- Severe

Sand
- >25% sand
- Sandy layer/mottle/patch
- Interval with sandy layers

Clast

Shell

Authigenic carbonates
- Disseminated auth carbonates
- Dolostone
- F Yellowish foraminifers

Microfossils
- Diatom bearing (5%-10%)
- Diatom rich (10%-40%)
- >40% diatoms
- Foraminifer bearing (5%-10%)
- Foraminifer rich (10%-40%)
- >40% foraminifers
- Calc nannofossil bearing (5%-10%)
- Calc nannofossil rich (10%-40%)
- >40% calc nannofossils
- Sponge spicule aggregate
- Sponge spicule bearing (5%-10%)
- Sponge spicule rich (10%-40%)
- >40% sponge spicules

Datums
- 300 Biostratigraphic
- 780 Paleomagnetic

**Figure F8.** Lithologic classification. **A.** Shepard ternary classification diagram. **B.** Biogenic classification. **C.** Siliciclastic and volcaniclastic classification. **D.** Summary of sediment classification.

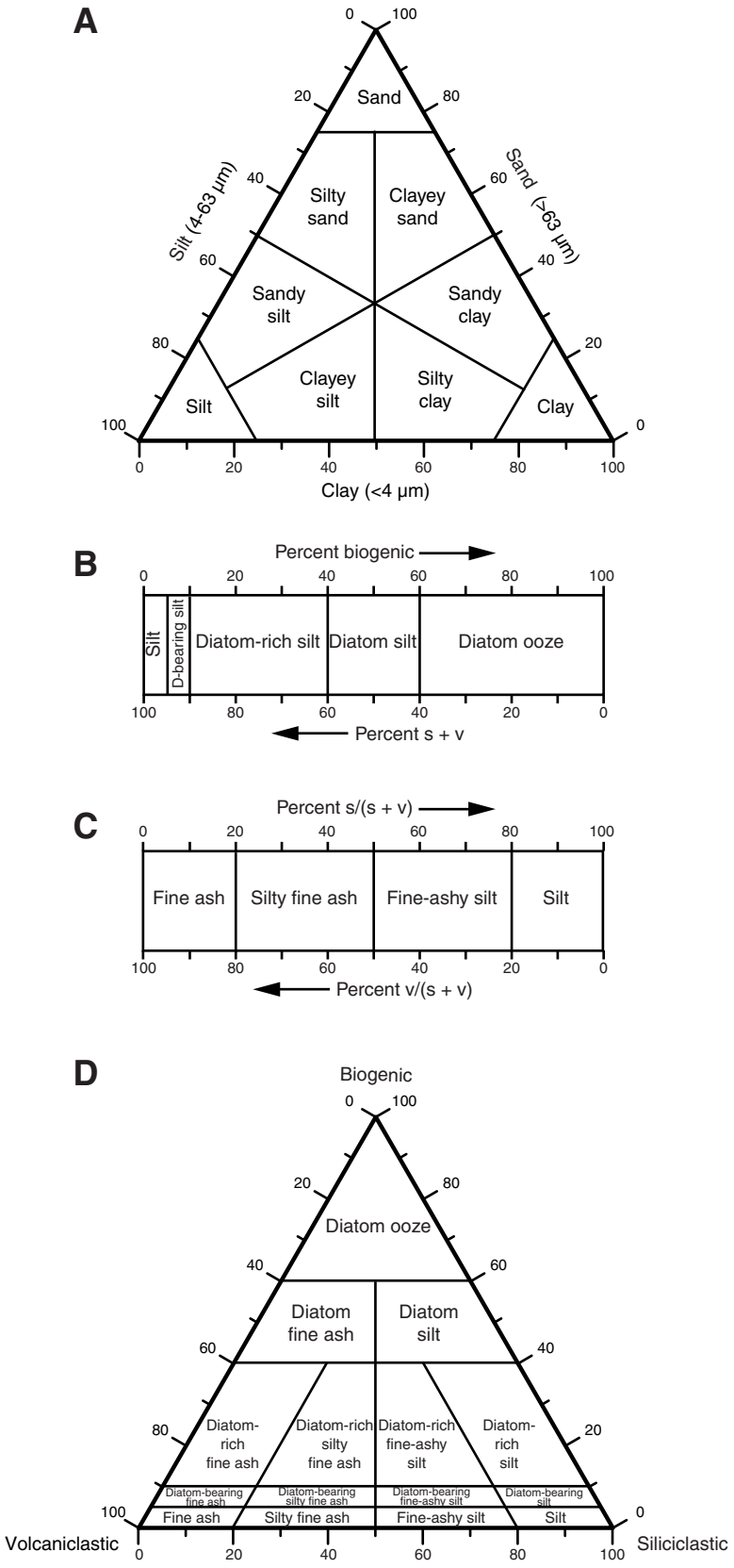

**Figure F9.** Coordinate systems used for archive- and working-half sections and for the superconducting rock magnetometer. SQUID = superconducting quantum interference device.

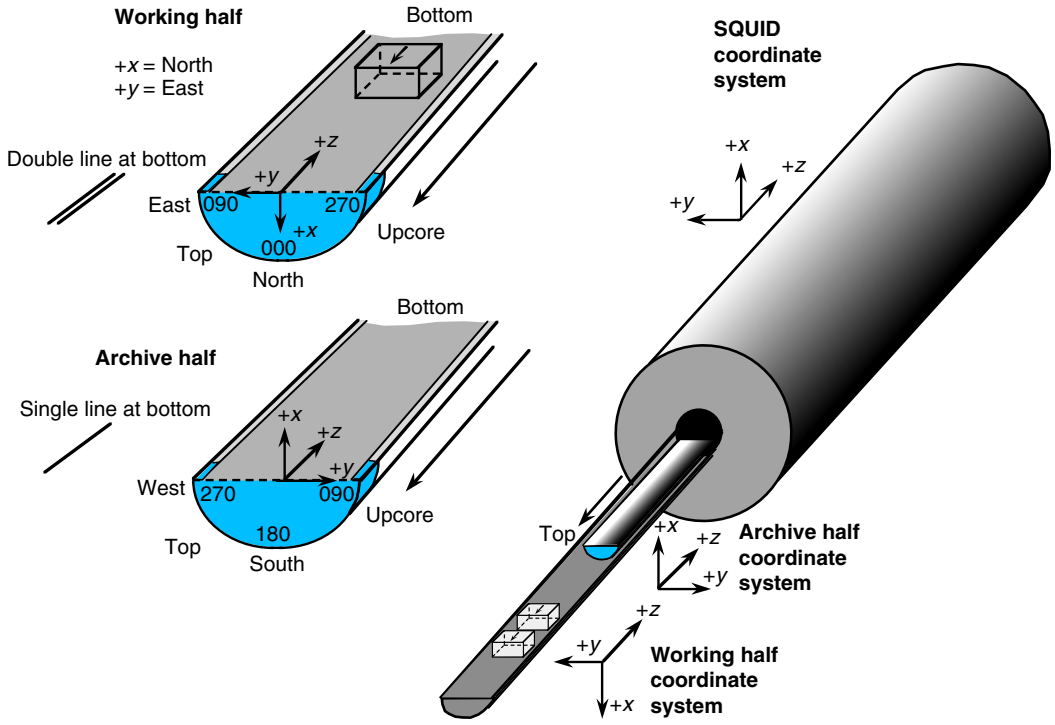

**Figure F10.** Sampling scheme used in microbiology-dedicated Hole U1345B. Sampling resolution varied in each of the four cores sampled. Holes were drilled on the catwalk for sampling volatile hydrocarbons at high resolution. All other sampling took place in the Cold Laboratory (~7°C), where unsqueezed interstitial water whole rounds were stored in a nitrogen-filled glove box. Upon cutting of the microbiology whole round, samples were immediately taken and treated for shore-based analyses.

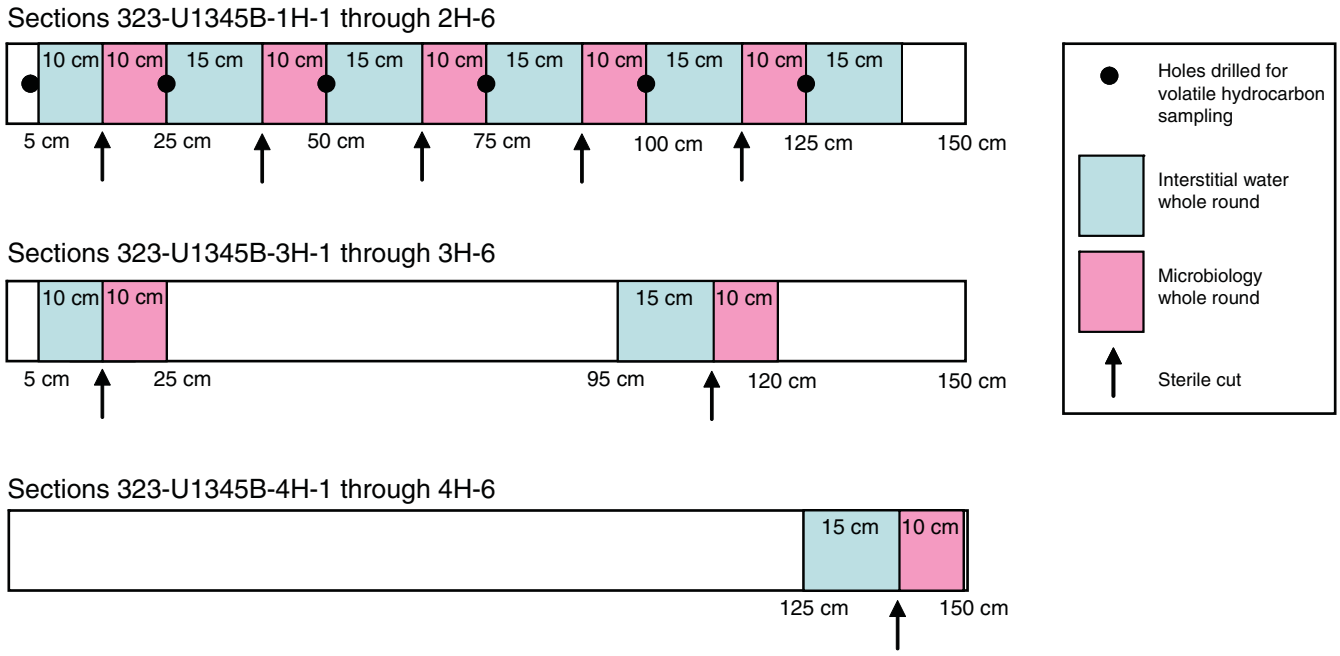

**Figure F11.** Wireline tool strings used during Expedition 323. See specific site chapters for tool strings deployed at each site. Triple combo = triple combination, HNGS = Hostile Natural Gamma Ray Sonde, HLDS = Hostile Environment Litho-Density Sonde, APS = Accelerator Porosity Sonde, GPIT = General Purpose Inclinometry Tool, DIT = Dual Induction Tool, FMS = Formation MicroScanner, DSI = Dipole Sonic Imager.

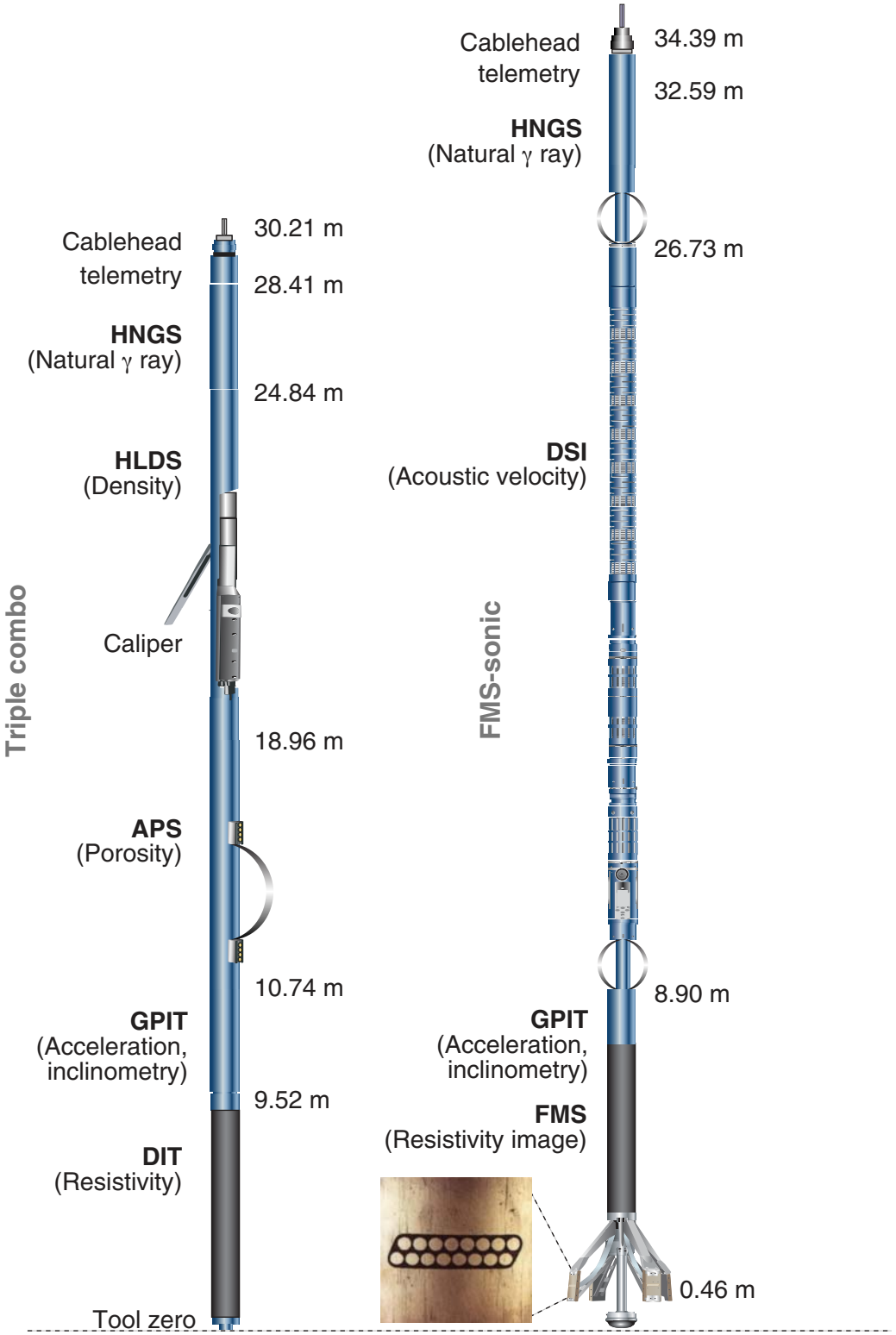

**Table T1.** Calcareous nannofossil datum events. (See table notes.)

| Datum event | Zone (base)* | Age (Ma) | Reference |
|---|---|---|---|
| FO *Emiliania huxleyi* | NN21 | 0.29 | Lourens et al. (2004) |
| LO *Pseudoemiliania lacunosa* | NN20 | 0.44 | Lourens et al. (2004) |
| LCO *Reticulofenestra asanoi* | | 0.91 | Lourens et al. (2004) |
| LO *Gephyrocapsa* spp. (large) | | 1.26 | Lourens et al. (2004) |
| FO *Gephyrocapsa* spp. (large) | | 1.56 | Lourens et al. (2004) |
| FO *Gephyrocapsa* spp. (medium) | | 1.69 | Lourens et al. (2004) |
| Pliocene/Pleistocene boundary | | 1.806 | Lourens et al. (2004) |
| LCO† *Dictyococcites* spp. (small) | | 2.75 | Sato et al. (2002) |
| LO *Reticulofenestra pseudoumbilicus* | NN16 | 3.7 | Lourens et al. (2004) |

Notes: * = based on Martini (1971), † = reversal in dominance between *Dictyococcites* spp. (small) and *Coccolithus pelagicus.* FO = first occurrence, LO = last occurrence, LCO = last common occurrence.

**Table T2.** Planktonic foraminifer datum events. (See table note.)

| Datum event | Age (Ma) | Polarity interval | Reference | Region |
|---|---|---|---|---|
| FO *Neogloboquadrina pachyderma* (sinistral) | 1.8 | C2n | Weaver and Clement (1987); Spezzaferri (1998) | N. Atlantic |
| LO *Neogloboquadrina atlantica* (sinistral) | 2.4–2.5 | C2r.2r | Weaver and Clement (1987); Spezzaferri (1998) | N. Atlantic |
| FO *Globorotalia puncticulata* | 4.6 | C3n.2n | Weaver and Clement (1987) | N. Atlantic |
| FO *Neogloboquadrina pachyderma* (dextral) | 5.3–5.7 | C3r | Weaver and Clement (1987) | N. Atlantic |

Note: FO = first occurrence, LO = last occurrence.

**Table T3.** Shipboard paleomagnetism laboratory equipment. (See table note.)

| Equipment | Status | Quality assessment |
|---|---|---|
| 2G Enterprises 760R Superconducting Rock Magnetometer | Used and functional | Magnetic moments for a 150 cm blank (air) after tray and background corrections is <1E–10 $Am^2$. Magnetic field in sensor region is <8 nT*. |
| AGICO KappaBridge KLY-4*S* susceptibility meter | Used and functional | Used to measure bulk susceptibilities |
| DTECH D-2000 alternating field (AF) demagnetizer | Not used | Undetermined |
| Schonstedt TSD-1 thermal demagnetizer | Used and functional | Thermal demagnetization experiments were conducted on 13 discrete samples |
| ASC IM-10 impulse magnetizer (Serial 01971) | Tested and functional | Undetermined |
| Applied Physics portable fluxgate magnetometer (Model 520) | Tested and functional | Resolution <1 nT* |
| Molspin minispin magnetometers (two) | Not used | Undetermined |

Note: * = from survey of the magnetic field inside the instrument and around the lab, completed during Expedition 320T.

**Table T4.** Normal polarity intervals of the Expedition 323 geomagnetic polarity timescale.

| Age (Ma) | | | |
|---|---|---|---|
| Top | Bottom | Polarity chron | Reference |
| 0.000 | 0.781 | C1n Brunhes | Lourens et al. (2004) |
| 0.988 | 1.072 | C1r.1n Jaramillo | Lourens et al. (2004) |
| 1.173 | 1.185 | C1r.2n Cobb Mountain | Lourens et al. (2004) |
| 1.778 | 1.945 | C2n Olduvai | Lourens et al. (2004) |
| 2.128 | 2.148 | C2r.1n Reunion | Lourens et al. (2004) |
| 2.581 | 3.032 | C2An.1n Gauss | Lourens et al. (2004) |
| 3.116 | 3.207 | C2An.2n | Lourens et al. (2004) |
| 3.330 | 3.596 | C2An.3n | Lourens et al. (2004) |
| 4.187 | 4.300 | C3n.1n Cochiti | Lourens et al. (2004) |
| 4.493 | 4.631 | C3n.2n Nunivak | Lourens et al. (2004) |
| 4.799 | 4.896 | C3n.3n Sidufjall | Lourens et al. (2004) |
| 4.997 | 5.235 | C3n.4n Thvera | Lourens et al. (2004) |
| 6.033 | 6.252 | C3An.1n | Lourens et al. (2004) |
| 6.436 | 6.733 | C3An.2n | Lourens et al. (2004) |
| 7.140 | 7.212 | C3Bn | Lourens et al. (2004) |
| 7.251 | 7.285 | C3Br.1n | Lourens et al. (2004) |
| 7.454 | 7.489 | C3Br.2n | Lourens et al. (2004) |
| 7.528 | 7.642 | C4n.1n | Lourens et al. (2004) |
| 7.695 | 8.108 | C4n.2n | Lourens et al. (2004) |
| 8.254 | 8.300 | C4r.1n | Lourens et al. (2004) |
| 8.769 | 9.098 | C4An | Lourens et al. (2004) |
| 9.312 | 9.409 | C4Ar.1n | Lourens et al. (2004) |
| 9.656 | 9.717 | C4Ar.2n | Lourens et al. (2004) |
| 9.779 | 9.934 | C5n.1n | Lourens et al. (2004) |
| 9.987 | 11.040 | C5n.2n | Lourens et al. (2004) |
| 11.118 | 11.154 | C5r.1n | Lourens et al. (2004) |
| 11.554 | 11.614 | C5r.2n | Lourens et al. (2004) |
| 12.014 | 12.116 | C5An.1n | Lourens et al. (2004) |
| 12.207 | 12.415 | C5An.2n | Lourens et al. (2004) |
| 12.730 | 12.765 | C5Ar.1n | Lourens et al. (2004) |
| 12.820 | 12.878 | C5Ar.2n | Lourens et al. (2004) |
| 13.015 | 13.183 | C5AAn | Lourens et al. (2004) |
| 13.369 | 13.605 | C5ABn | Lourens et al. (2004) |
| 13.734 | 14.095 | C5ACn | Lourens et al. (2004) |
| 14.194 | 14.581 | C5ADn | Lourens et al. (2004) |
| 14.784 | 14.877 | C5Bn.1n | Lourens et al. (2004) |
| 15.032 | 15.160 | C5Bn.2n | Lourens et al. (2004) |
| 15.974 | 16.268 | C5Cn.1n | Lourens et al. (2004) |
| 16.303 | 16.472 | C5Cn.2n | Lourens et al. (2004) |
| 16.543 | 16.721 | C5Cn.3n | Lourens et al. (2004) |
| 17.235 | 17.533 | C5Dn | Lourens et al. (2004) |
| 18.056 | 18.524 | C5En | Lourens et al. (2004) |
| 18.748 | 19.722 | C6n | Lourens et al. (2004) |
| 20.040 | 20.213 | C6An.1n | Lourens et al. (2004) |
| 20.439 | 20.709 | C6An.2n | Lourens et al. (2004) |
| 21.083 | 21.159 | C6AAn | Lourens et al. (2004) |
| 21.403 | 21.483 | C6AAr.1n | Lourens et al. (2004) |
| 21.659 | 21.688 | C6AAr.2n | Lourens et al. (2004) |
| 21.767 | 21.936 | C6Bn.1n | Lourens et al. (2004) |
| 21.992 | 22.268 | C6Bn.2n | Lourens et al. (2004) |
| 22.564 | 22.754 | C6Cn.1n | Lourens et al. (2004) |
| 22.902 | 23.030 | C6Cn.2n | Lourens et al. (2004) |
| 23.278 | 23.340 | C6Cn.3n | Pälike et al. (2006) |

**Table T5.** Depth scale definitions, Expedition 323. (See table note.)

| Depth scale | | Description |
|---|---|---|
| IODP | ODP | |
| CSF-A | mbsf | Core depth below seafloor, assigned by drillers |
| CCSF-A | mcd | Core composite depths appended from affine table |
| CCSF-B | cmcd | Core composite depths scaled to remove growth factor |
| CCSF-C | rmcd | Core composite depths for off-splice sections correlated into the primary splice |
| CCSF-D | mcd | Core composite depths within the primary splice (identical to CCSF-A within the splice sections) |
| CCSF-E | Undefined | Core composite depths for "floating" composite intervals outside the primary splice |
| CCSF-L (informal) | eld | Core composite depths correlated to WSF |
| WSF | Log-mbsf | Wireline log depth below seafloor (m) |
| Offset | DIS | Depth in section, depth offset from top of parent sample |

Note: IODP = Integrated Ocean Drilling Program, ODP = Ocean Drilling Program.

**Table T6.** Measurements made by wireline tool strings. (See table notes.)

| Tool string | Tool | Measurement | Sampling interval (cm) | Approximate vertical resolution (cm) |
|---|---|---|---|---|
| Triple combination | HNGS | Spectral gamma ray | 15 | 20–30 |
| | GPIT | Tool orientation | 3.8 | NA |
| | HLDS | Bulk density | 2.5 and 15 | 38 |
| | DIT | Resistivity | 15 | 240/180/92 |
| | APS | Porosity | 5 and 15 | 36 |
| Formation MicroScanner (FMS)-sonic combination | HNGS | Spectral gamma ray | 15 | 20–30 |
| | GPIT | Tool orientation | 3.8 | NA |
| | FMS | Microresistivity | 0.25 | 0.5 |
| | DSI | Acoustic velocity | 15 | 107 |

Notes: NA = not applicable. All tool and tool string names are trademarks of Schlumberger. For definitions of tool acronyms, see Table T7.

**Table T7.** Measurement acronyms and units of wireline logging tools deployed during Expedition 323. (See table note.)

| Tool | Output | Description | Unit |
|---|---|---|---|
| APS | | Accelerator Porosity Sonde | |
| | APLC | Near array porosity | % |
| | STOF | Tool standoff | inch |
| | SIGF | Formation capture cross-section | Capture units |
| DIT | | Dual Induction Tool | |
| | IDPH | Deep induction phasor-processed resistivity | Ωm |
| | IMPH | Medium induction phasor-processed resistivity | Ωm |
| | SFLU | Spherically focused resistivity | Ωm |
| DSI | | Dipole Sonic Imager | |
| | DTCO | Compressional wave delay time (Δt) | µs/ft |
| | DTSM | Shear wave delay time (Δt) | µs/ft |
| FMS | | Formation MicroScanner | |
| | C1, C2 | Orthogonal hole diameters | inch |
| | P1AZ | Pad 1 azimuth | ° |
| | | Spatially oriented resistivity images of borehole wall | |
| GPIT | | General Purpose Inclinometry Tool | |
| | DEVI | Hole deviation | ° |
| | HAZI | Hole azimuth | ° |
| | F*x*, F*y*, F*z* | Earth's magnetic field (three orthogonal components) | oersted |
| | A*x*, A*y*, A*z* | Acceleration (three orthogonal components) | $m/s^2$ |
| HLDS | | Hostile Environment Litho-Density Sonde | |
| | RHOM | Bulk density | $g/cm^3$ |
| | PEFL | Photoelectric effect | barn/$e^-$ |
| | LCAL | Caliper (measure of borehole diameter) | inch |
| | DRH | Bulk density correction | $g/cm^3$ |
| HNGS | | Hostile Natural Gamma Ray Sonde | |
| | HSGR | Standard (total) gamma ray | gAPI |
| | HCGR | Computed gamma ray (HSGR minus uranium contribution) | gAPI |
| | HFK | Potassium | wt% |
| | HTHO | Thorium | ppm |
| | HURA | Uranium | ppm |

Note: For the complete list of acronyms used in IODP and for additional information about tool physics and use, consult IODP-USIO Science Services, LDEO, at iodp.ldeo.columbia.edu/TOOLS_LABS/tools.html.

# Appendix

## Physical properties calibration issues

### Magnetic susceptibility

During drilling, problems were noticed with bias changes in magnetic susceptibility data. These problems were to be addressed on shore. Magnetic susceptibility loop sensor instability sometimes resulted in very low readings by both the STMSL and the WRMSL. When low readings were observed on board, cores were reanalyzed on the track loggers. Because the magnetic susceptibility loop sensors were not calibrated on board, the only way to correct the data sets may be to check magnetic susceptibility blank measurements before and after track measurements. Postcruise efforts to correct magnetic susceptibility data should be attempted.

### Gamma ray attenuation

Calibration issues with GRA bulk density measurements occurred during the cruise. At Site U1341, both STMSL and WRMSL GRA bulk density data were found to be out of calibration; recalibration of the GRA sensor occurred in the middle of collecting data from Cores 323-U1341A-9H (WRMSL) and 13H (STMSL). Earlier calibration data were not available for either track. Both cores were reanalyzed after calibration. This comparison, along with comparison of the data overlap intervals in Holes U1341A, U1341B, and U1341C (in the CCSF-A depth scale, interpolated to 10 cm intervals and smoothed with a Gaussian window of 9 cm half-width to minimize offsets caused by small miscorrelations), suggests approximate correction factors of 0.016 (+0.002) subtracted from WRMSL GRA values measured prior to and including timestamp 2009-07-28 13:17:45.468 Universal Time Coordinated (UTC) and 0.351 (+0.006) subtracted from STMSL GRA values measured prior to and including timestamp 2009-07-28 02:30:07.312 UTC (Fig. **AF1**). As a result of this discovery, the GRA sensors on the WRMSL and the STMSL were recalibrated with an aluminum standard before measurements began in each hole.

Although calibration runs were performed after this discovery, out-of-calibration issues often recurred. Because of gas-expansion disruption of core sediment on the catwalk, holes were commonly drilled in the core liner about 10 cm apart. Sediment composed mainly of silty and clayey mud commonly extruded through the punctured holes in the core section during STMSL and WRMSL measurements. Because of the vertical placement of the GRA source (above the core tube) and detector (beneath the core tube), extruded mud tended to accumulate on the detector, which attenuated the GRA signal relative to its calibration (causing estimates of GRA density to be too high). When this was noticed, the extruded mud smeared on the scintillation detector was cleaned up and a GRA calibration standard was run before measurements began. It was not always possible to run calibrated measurements, so postcruise efforts to refine the calibration and correct the GRA bulk density data sets are probably necessary.

### Natural gamma radiation

NGR data are very useful in detecting sedimentary cycles recorded by variations in clay content, which are invaluable in establishing stratigraphic correlations. However, systematic variation in NGR readings for core sections was observed during the cruise (Fig. **AF2**). Figure **AF2** shows an example of the NGRL measurements recorded on board. In this figure, the NGR data from Hole U1343A are superimposed on the intervals in each section for all sections. There are two measurement issues: (1) a trend of decreasing intensity at both ends of the 1.5 m core section and (2) recordings of high-intensity peaks for each core section. The low counts for the section ends may be caused by the instrument's architecture. The second feature (two high-intensity lobes) may be related to calibration among the seven scintillation counters. The last calibration of the NGRL was carried out on 1 July 2009 near Victoria, British Columbia, Canada. No calibration of the instrument was possible during Expedition 323. The first calibration issue concerns background levels of NGR intensity. NGR flux in the Bering Sea is higher than in the equatorial Pacific Ocean; therefore, it might be necessary to correct for the higher background intensity of onboard measurements. The second calibration issue concerns an electrical shutdown and restart of the NGRL that occurred in the middle of the expedition.

Postcruise correction of NGR data would significantly enhance the usefulness of the NGR data sets. Table **AT1** provides example corrections to NGR count data.

### Color reflectance

Before each core was measured, the spectrophotometer was calibrated with a Labsphere-certified white reflectance standard and a black light trap with the light source shuttered. These standards were covered with the same plastic wrap used to cover the core section. For Sites U1339–U1341, the instrument was calibrated every 12 h with the same piece of plastic wrap covering the standards. Shipboard scientists observed the following calibration issues for color reflectance using the SHMSL: (1) reflectance data were affected by light leakage from the room

lights into the sensor (depending on how flat the section half surface was) or light channeling along the plastic wrap (confirmed by the detection of Hg-emission lines from the laboratory's fluorescent lights); (2) reflectance data were not stable over 12 h timescales (for unknown reasons), requiring more frequent calibration; and (3) some of the plastic wrap was discovered to be yellowish, and different batches of plastic wrap were used on the white calibration and sediment core. Several unexplained excursions in b* data could possibly be explained by the use of yellowed plastic wrap. Unfortunately, the source of plastic was not documented for each core section, so it is not straightforward to check for these artifacts.

**Figure AF1.** Comparison of STMSL gamma ray attenuation (GRA) bulk density before and after calibration for Core 323-U1341A-13H.

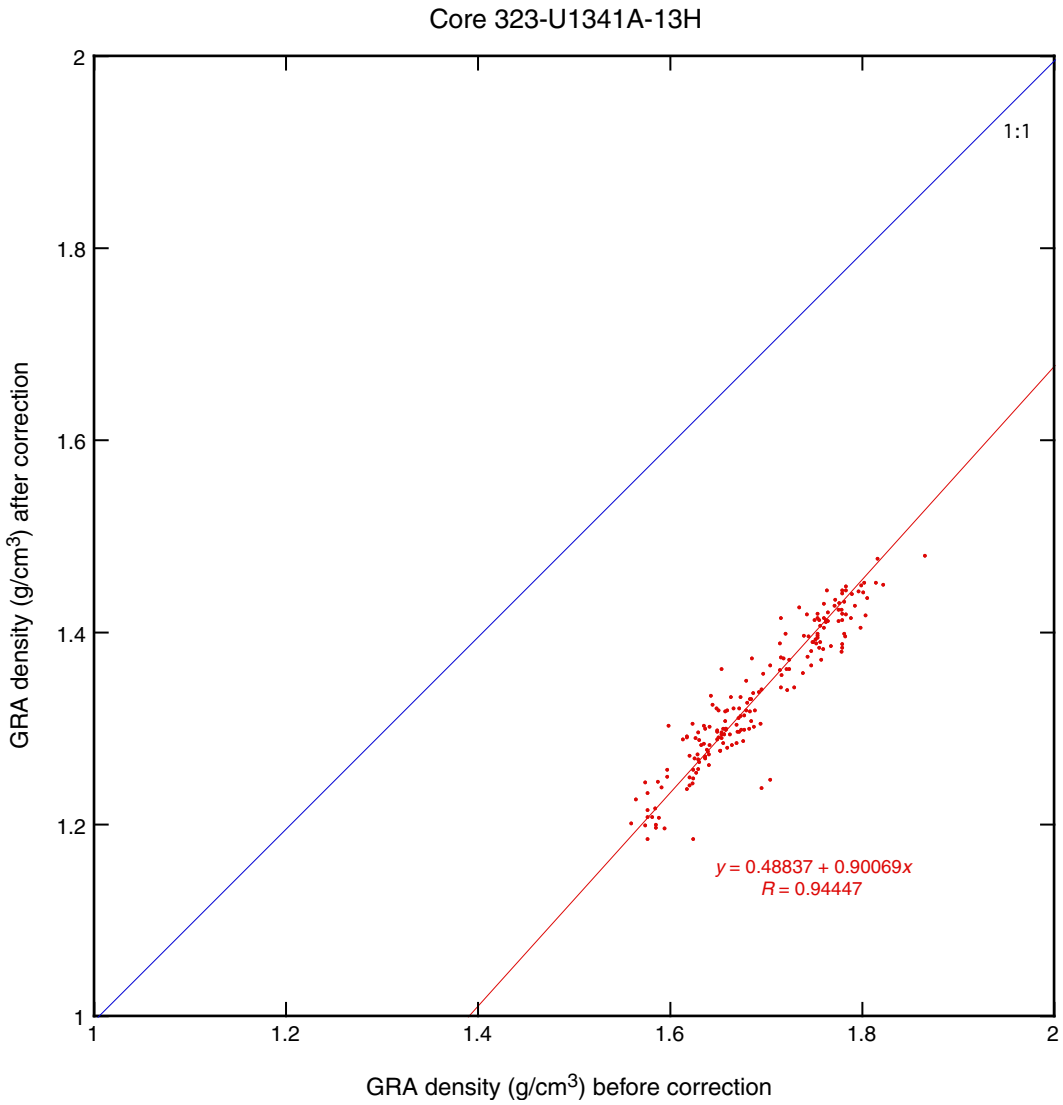

**Figure AF2.** NGRL measurements for all core sections from Hole U1343A. Natural gamma radiation (NGR) data are degraded by superimposed system measuring errors.

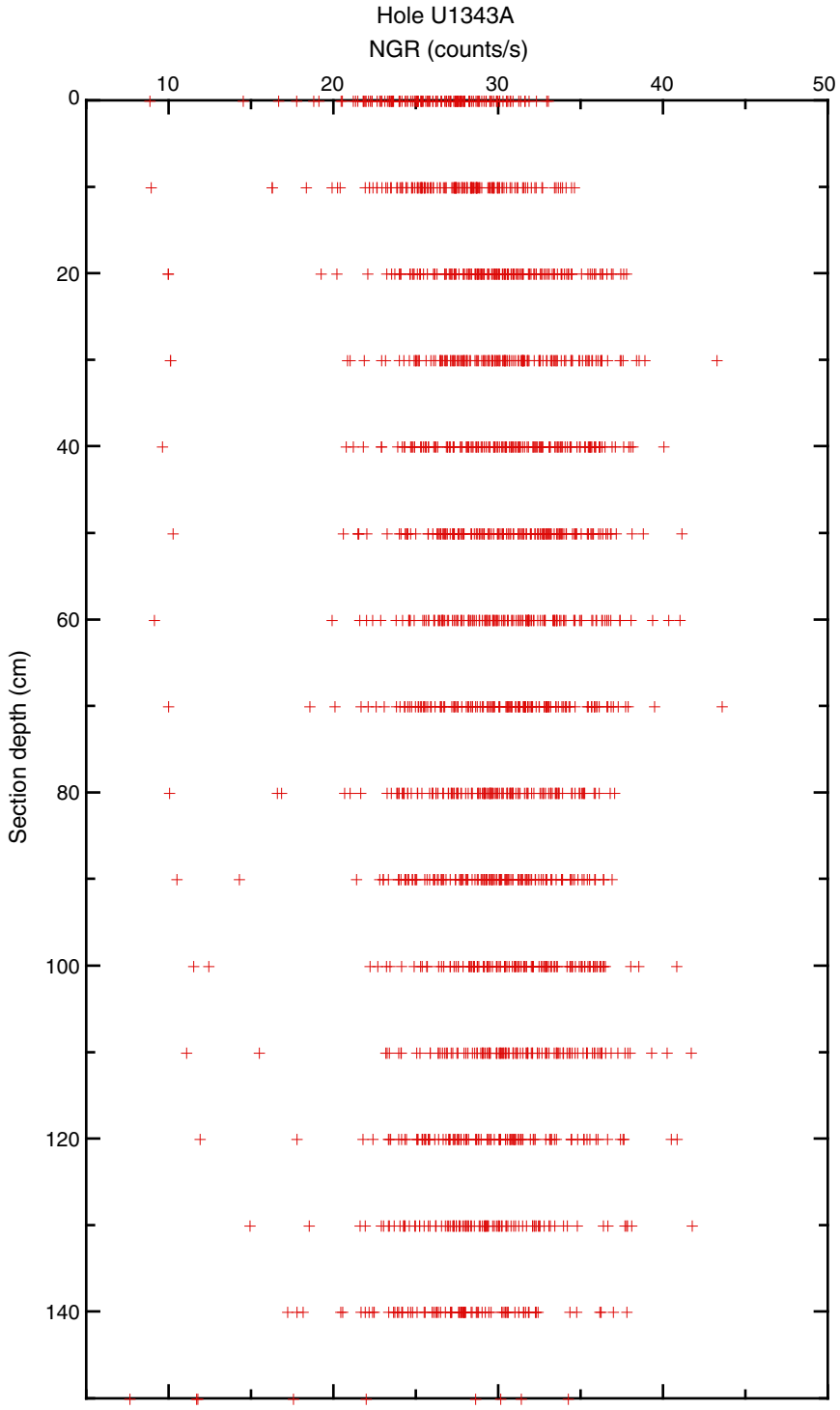

**Table AT1.** Example of corrections to natural gamma radiation (NGR) count data. (See table note.)

| Depth in section (cm) | NGR (counts/s) | | |
|---|---|---|---|
| | Median | Standard error | Correction |
| 0 | 26.6 | 0.3 | –3.2 |
| 10 | 27.8 | 0.3 | –2.1 |
| 20 | 30.0 | 0.4 | 0.1 |
| 30 | 30.3 | 0.4 | 0.4 |
| 40 | 30.7 | 0.4 | 0.8 |
| 50 | 30.6 | 0.4 | 0.8 |
| 60 | 30.4 | 0.4 | 0.5 |
| 70 | 30.9 | 0.4 | 1.0 |
| 80 | 29.6 | 0.4 | –0.3 |
| 90 | 29.7 | 0.4 | –0.2 |
| 100 | 31.2 | 0.4 | 1.3 |
| 110 | 31.0 | 0.4 | 1.1 |
| 120 | 29.4 | 0.4 | –0.4 |
| 130 | 28.9 | 0.4 | –0.9 |
| 140 | 27.9 | 0.5 | –2.0 |
| 150* | 22.1 | 3.3 | –7.8 |

Note: * = the large apparent correction and the large standard error at 150 cm may be artifacts of core section length, with the sensor sometimes recording no sediment.